12-2016

A Study on Wide-area Measurement-based Approaches for Power System Voltage Stability

Haoyu Yuan
University of Tennessee, Knoxville, hyuan2@vols.utk.edu

To the Graduate Council:

I am submitting herewith a dissertation written by Haoyu Yuan entitled "A Study on Wide-area Measurement-based Approaches for Power System Voltage Stability." I have examined the final electronic copy of this dissertation for form and content and recommend that it be accepted in partial fulfillment of the requirements for the degree of Doctor of Philosophy, with a major in Electrical Engineering.

Fangxing Li, Major Professor

We have read this dissertation and recommend its acceptance:

Yilu Liu, Kai Sun, MIngzhou Jin

Accepted for the Council:

Carolyn R. Hodges

Vice Provost and Dean of the Graduate School

(Original signatures are on file with official student records.)

A Study on Wide-area Measurement-based Approaches for Power System Voltage Stability

A Dissertation Presented for the

Doctor of Philosophy

Degree

The University of Tennessee, Knoxville

Haoyu Yuan

December 2016

ACKNOWLEDGEMENTS

First and foremost, I would like to express my deepest gratitude to my advisor, Dr. Fangxing Li for his continuous guidance and persistent help for this dissertation and all other research during my Ph.D. study at the University of Tennessee at Knoxville (UTK).

I am very thankful to my dissertation committee members, Dr. Yilu Liu, Dr. Kai Sun, and Dr. Mingzhou Jin, for their time and valuable comments.

Moreover, I would like to express my special thanks to Dr. Tao Jiang and Dr. Yanli Wei for being my mentors in the area of power system stability and power system economics, respectively. Also, I would like to thank all the members at my research group for always being supportive and to thank the friends and professors in the Center for Ultra-Wide-Area Resilient Electric Energy Transmission (CURENT) for creating a loving and friendly atmosphere for conducting research.

Last but not the least I am greatly indebted to my parents and my wife for their unconditional love and support, without whom it is impossible for me to finish this work.

ABSTRACT

With the development of wide-area monitoring system (WAMS) enabled by the synchrophasor technology, measurement-based approaches for power system voltage stability and control have been widely discussed in recent years. Based on high-frequency synchronized measurement signals collected from phasor measurement units (PMUs), these approaches have great potentials to significantly improve the situational awareness and to effectively guide the controls of interconnected modern power systems.

If compared with conventional model-based voltage stability assessment (VSA) and control methods, the measurement-based methods are relatively new. Although their simplicity and independence of system models make them suitable for online deployment, the applications of these measurement-based methods are not as well explored as their model-based counterparts, which have been improved and matured over several decades. Therefore, the motivation of this dissertation is to explore new applications of measurement-based voltage stability assessment and control.

In this dissertation, first, a comparative study on existing measurement-based approaches is provided; second, a hybrid VSA approach for N-1 contingency is proposed; third, measurement-based wide-area loading margin sensitivity suitable for voltage stability control is presented with a sample control study; fourth, mitigation approaches for overestimation of voltage stability margin when using coupled single-port circuit are proposed; and fifth, voltage dependent load model is integrated into measurement-based voltage stability analysis to provide a practical and accurate assessment of voltage stability margin.

Keywords: Measurement-based approach, voltage stability, voltage stability control, wide-area measurement systems (WAMS), phasor measurement unit (PMU), Thevenin equivalent, coupled single-port circuit, voltage dependent load, and ZIP load.

TABLE OF CONTENTS

LIST OF TABLES

LIST OF FIGURES

CHAPTER 1

INTRODUCTION AND GENERAL INFORMATION

Voltage stability is a major concern for today's power system operation and control [1]. Failure to detect voltage instability or to take prompt control has caused several system-wide blackouts. In the past decade, the penetration of renewable and intermittent generations [2]–[8] as well as the total loads in power systems keeps increasing, while the transmission capability and the traditional generation capacity have not increased in a comparable pace. Consequently, the power systems of today are being operated closer to their limits than before [9]. Therefore, to maintain the reliability of an electric power system, it is crucial that the voltage stability margin is assessed accurately and timely.

On the other hand, the world-wide deployment of synchronized phasor measurement units (PMUs) and the development of wide-area monitoring systems (WAMS) in recent years [10]–[12] have enabled measurement-based tools for power system stability assessment [13]–[18]. The study in this dissertation will focus on measurement-based voltage stability assessment and control.

1.1 Measurement-Based Voltage Stability Assessment

Voltage stability, also known as load stability, is often assessed using model-based static methods such as continuation power flow (CPF) [19], [20] or optimization methods [21]–[23]. Such methods need detailed and accurate models of generators, transformers, transmission lines, and loads to assess the system stability margin on a certain load increasing pattern. Based on the model and load increasing pattern,

techniques such as CPF will also require a significant amount of computational efforts to solve the load margin. Moreover, recent developments of renewable energy [24]–[26], energy storage [7], [27], and demand response [28]–[30] bring more complexity to the modeling of modern power systems. Therefore, for a practical system, such model-based static studies may not be highly suitable for online assessment, but are conducted off-line to assess the voltage stability.

With the availability of phasor measurement units (PMUs), measurement-based voltage stability assessment (VSA) approaches have been proposed [13], [31]–[37]. Such measurement-based methods require no or little information of the complex system models, therefore, they are highly efficient in terms of computation [38], [39]. However, measurement-based approaches are still in their early stage of development, and the applications of the measurement-based VSA are still mostly limited to voltage stability assessment.

1.1.1 Thevenin Identification Methods

For all the measurement-based VSA methods, the calculation of the Thevenin equivalence (TE) from measurement data is the most fundamental and time consuming step. Therefore, the performance of the TE identification method is crucial for these measurement-based methods to be implemented online.

Although these TE identification methods all achieve good accuracy in their respective test cases, they have not been compared explicitly with each other on the same test case. Further, some of the methods [31], [34] are tested on pseudo-measurements

from power flow results. It is stated that time domain simulations including slow dynamics of the system may better demonstrate the problem of voltage stability [1].

Tests of different TE identification methods on the same time domain simulated test case provide another perspective for evaluating these methods. In our study in Chapter 3, the test results of four existing methods from [31]–[34] on the practical Northeast Power Coordinating Council (NPCC) 140-bus system discover some new characteristics of these methods that have never been mentioned in previous works.

1.1.2 Hybrid VSA for N-1 Contingency

To maintain the reliability of an electric power system during operation, it is of significant importance that the voltage stability margins for both normal and N-1 contingency status should be assessed accurately and timely [40].

For a practical power system, the number of the contingencies needed to be monitored usually can be in the same order of the system size. That is, the computation burden of assessing the VSA of N-1 contingency is N times of the computation burden of assessing the VSA of normal operating condition. Certainly, many heuristic rules such as identifying the root contingency cases are usually applied in practice to reduce the computational burden. However, the number of N-1 contingency cases is still a large number demanding significant computation efforts.

Unfortunately, in existing measurement-based approaches, there is no report in the literatures that aimed to directly assessing the voltage stability margin under N-1 contingencies. Thus, this is a much under-developed area if compared with VSA for normal condition.

In this dissertation, a hybrid VSA method is proposed in Chapter 4 to perform N-1 contingency analysis at high accuracy and efficiency, which can be suitable for online applications. For contingency analysis, the hybrid approach integrates the model-based sensitivity which gives fast estimation of the post-contingency system status. A variety of studies discussed such sensitivity analysis in the literature [41], [42] using different techniques. In [41], the outage line was kept in the system, while it was transformed to two hypothetical, dummy buses in [42]. Both approaches achieve decent results. Essentially, these sensitivity factors, a.k.a., distribution factors, are based on the Newton-Raphson Jacobian matrix to represent the contingencies as changes of nodal power injection. However, this work attempts to further advance the sensitivity analysis such that the topological transformation will be mathematically proven and a succinct model will be proposed (e.g., to eliminate the extra buses in the previous work that must be added into the network). In addition, estimated voltage angles, which are crucial for VSA but not studied/compared in the previous works, will be explored in this work. This is another important goal of this work.

1.2 Measurement-Based Voltage Stability Control

The development of measurement-based voltage stability assessment approaches has great potential in improving the situational awareness in the control rooms. With the proposed hybrid VSA approach for N-1 analysis, insecure contingencies can be efficiently identified. In the next step, effective control actions should be taken to improve the voltage stability margin as soon as the insecure alert is issued to the system operators. However, measurement-based voltage stability control has rarely been

explored. In this dissertation, measurement-based loading margin sensitivity (LMS) is proposed in Chapter 5. A comprehensive control schemes based on the LMS is also developed.

To ensure voltage stability, it is required that the systems are operated with a sufficient voltage stability margin. Among various indices, loading margin (LM) is a fundamental measure of voltage stability margin and is closely monitored by many utilities. It is defined as the amount of additional load in a specific pattern of load increase that would cause a voltage collapse [43].

Despite its straightforward definition, the computation of LM is complicated and time-consuming. For applications that need to update the LM frequently, loading margin sensitivity (LMS) is often utilized. LMS refers to the sensitivity of the LM w.r.t. the variation of system parameters or controls.

Though the efficiency of the computation of LM or similar voltage stability margins has been improved, the calculation of these model-based sensitivities requires detailed system model, Jacobian matrix, and calculation of eigenvalues. Therefore, such model-based sensitivities may not be good candidates for online applications.

With the motivation to develop a simple measurement-based sensitivity, a wide-area loading margin sensitivity (WALMS) model is proposed in this work based on the coupled single-port concept [34]. The WALMS has been derived, with respect to real power injection, reactive power injection, and generator terminal voltage in this research work. Inheriting the simplicity of measurement-based approach, the proposed WALMS requires no additional information and minimum calculation on top of the coupled single-

port circuit method. In addition, in contrast to the model-based counterparts, the WALMS model does not require that the Jacobian matrix is singular to calculate the dominant eigenvalue. Based on WALMS, a multi-step voltage stability control strategy is proposed for demonstrating the applicability of WALMS.

1.3 Load Model in Voltage Stability Analysis and Control

In most voltage stability and analysis applications, load model is considered as constant P and constant Q model, which is voltage independent. The constant PQ load model works fine under the assumption that the voltage of the load bus is close to nominal (1 p.u.). However, when system is operating close to its limit, such assumption does not hold well. If the voltage is below the nominal level, the consumption of the real and reactive power should accordingly reduce. Constant PQ load is not able to model such voltage dependence characteristics and will eventually lead to a more conservative operating margin [13], [44], [45].

A widely-used load model that incorporates the voltage dependence is the ZIP load model. Under this load model, 100% of the real power is partitioned into constant impedance (Z) load, constant current (I) load, and constant power (P) load. The reactive power is also divided into Z, I, and P load model and the distribution may be different than the real power consumption. The power consumption of constant impedance (Z) load is quadratically dependent on voltage magnitude; the power consumption of constant current (I) load is linear dependent on the voltage magnitude; the power consumption of the constant power (P) load is independent of the voltage magnitude.

In this dissertation, the impact of ZIP load model to voltage stability margin is studied. A novel measurement-based voltage stability indicator is developed to incorporate the impact of ZIP load model. This work is described in details in Chapter 7.

1.4 The Structure of Measurement-Based VSA and Control

In order to better illustrate the wide-area measurement-based voltage stability assessment and control, a structure or framework is proposed as shown in Figure 1. The process starts from the data input from PMU measurement as well as EMS. The data is passed to a data center where various applications can extract useful information.

Then, online voltage stability assessment should be first conducted to ensure that the system is operated in a stable condition with sufficient margin. In this step, the Thevenin equivalent (TE) identification which is discussed in Chapter 3 will be used.

The work in Chapter 6 and Chapter 7 also fall into the category of online VSA. Chapter 6 discusses the overestimation of coupled single-port circuit which is also introduced in Chapter 3. Chapter 7 then introduces ZIP load model into the assessment.

If the system is stable, then the N-1 contingency analysis should also be conducted. If not, corrective control should be applied.

For online voltage security assessment, the proposed hybrid VSA for N-1 contingency in Chapter 4 can be applied. If the system is also secure, no control action is needed. Otherwise, preventive control shall be applied.

The wide-area loading margin sensitivity introduced in Chapter 5 can be used for both corrective and preventive control to guide the system operators' decisions.

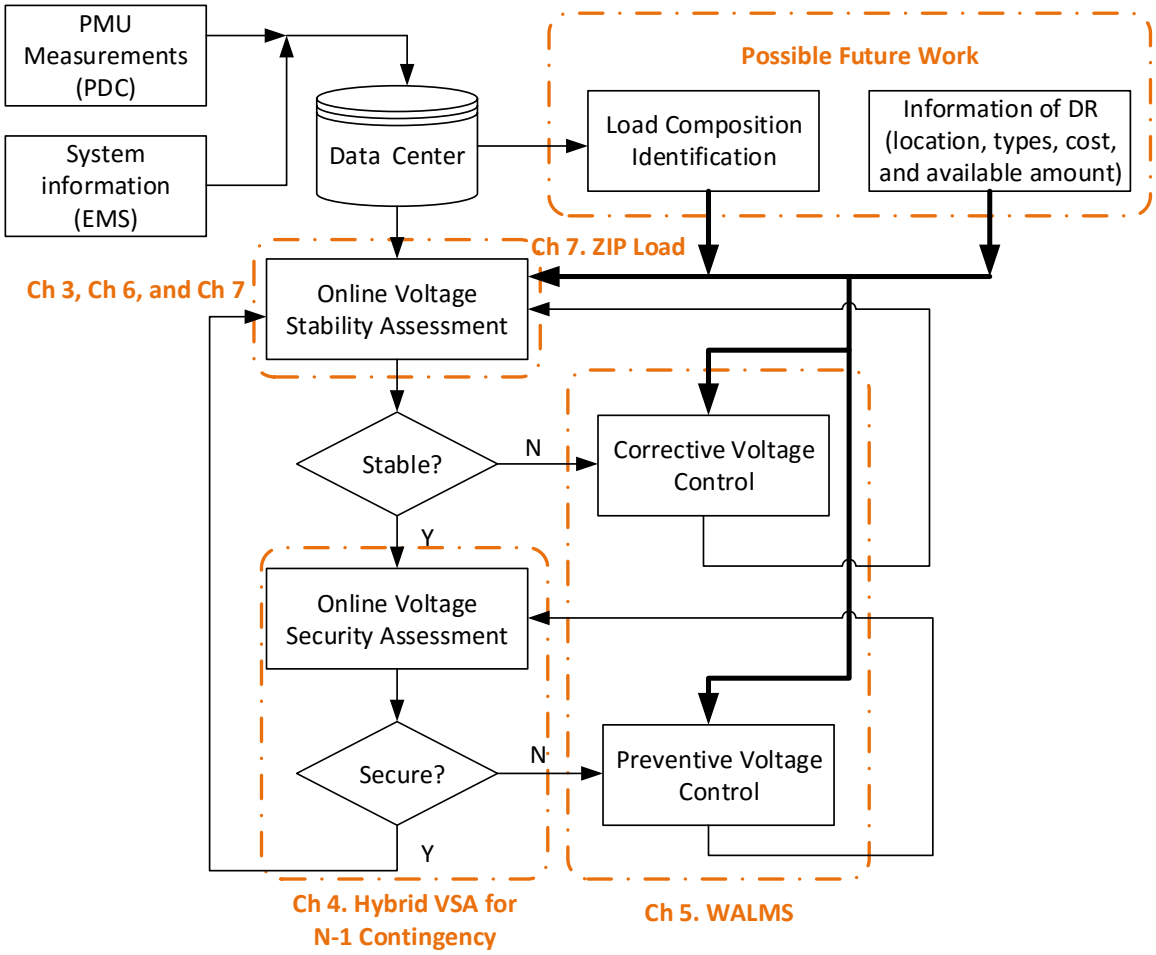

Figure 1. Framework of wide-area measurement-based VSA.

The future work will be associated with composite load modeling and demand response from measurements which will be beneficial for voltage stability assessment and controls. Indeed, the load composition identification will be input to voltage stability assessment as indicated in Figure 1. The proposed VSI in Chapter 7 will need such information for VSA.

1.5 Contributions of This Work

This work studies measurement-based voltage stability assessment and control. The contributions can be summarized into three aspects.

- This work presents an analytical comparative study of four different measurement-based Thevenin Equivalents (TE) identification methods. The detailed algorithm analysis and performance comparison on the measurements generated from time-domain simulation can serve as a general guidance on choosing the TE identification methods.

- The proposed hybrid voltage stability assessment for N-1 contingency broadens the practical application of measurement-based VSA to contingency analysis, which greatly improves the situational awareness in the control room.

- The proposed measurement-based wide-area loading margin sensitivity provides an efficient and effective sensitivity which aids the decisions of operators for improving the voltage stability. The proposed comprehensive control scheme provides a measurement-based online control algorithm for enhancing the system voltage stability.

- The two mitigation approaches introduced in Chapter 6 successfully mitigate the overestimation of voltage stability margin introduced in Coupled Single-Port Circuit method.
- A novel measurement-based voltage stability indicator is proposed which can incorporate the ZIP load model into measurement-based VSA study. With the proposed indicator, the voltage stability margin can be assessed closer to actual system behavior.

1.6 Organizations of the Dissertation

In Chapter 2, existing works on measurement-based voltage stability assessment and control are comprehensively reviewed. In Chapter 3, a comparative study on various measurement-based Thevenin Equivalent identification methods is presented. Chapter 4 introduces the proposed hybrid voltage stability assessment for N-1 contingency. Chapter 5 introduces the wide-area measurement-based loading margin sensitivity and the voltage stability control scheme based on the proposed LMS. Chapter 6 introduces the overestimation of voltage stability margin using coupled single-port circuit under a special condition and proposes two mitigation methods. In Chapter 7, the impact of ZIP load model to voltage stability analysis is studied and a novel measurement-based voltage stability indicator is proposed to incorporate the ZIP load model. Chapter 8 concludes the entire dissertation and discusses the potential future works.

CHAPTER 2

LITERATURE REVIEW

This chapter presents the review of past and on-going research findings relevant to the measurement-based approaches voltage stability assessment and control.

2.1 Measurement-Based Voltage Stability Assessment

Enabled by synchronized phasor measurement units (PMUs), measurement-based voltage stability assessment (VSA) approaches have been widely discussed in the recent decade. In an early work [31], Vu et al. proposed to use local phasor measurements to estimate the voltage stability margin. In [32], a local voltage-stability index using Tellegen's theorem is proposed. Corsi and Taranto proposed a real-time identification algorithm based on an adaptive method [33]. In [34], the concept of a coupled single-port circuit is proposed for considering voltage stability of a load area. The idea proposed in [31]–[33] uses local measurements to identify the system Thevenin Equivalent “seen” from the bus of interest. The critical point for voltage instability is reached when the absolute value of the load impedance is equal to the Thevenin equivalent impedance [46]. Besides the impedance matching criterion, several voltage instability indicators based on local measurements have been proposed [47], [48]. In some follow-up works [13], [34], [49], the Thevenin equivalent model is employed for measurement-based VSA. In [13], the ZIP load model is considered and a wide-area PMU network, rather than local measurements, is required for the proposed control scheme. In [49], a wide-area detection scheme combining load flow is proposed. In [34], the concept of coupled single-port circuit is proposed for considering voltage stability of a load area. In [36], a mitigation

factor is introduced on top of the coupled single-port circuit in order to address the situation where the load is not proportionally increased. In [50], a double voltage source is proposed to analyze multi-feed load center. In [51], a measurement-based monitoring method for a load area fed by N tie lines is proposed which monitors the transfer limits of the *N* infeed lines.

Among the above works, VSA for N-1 contingency, especially the transmission contingency, has not been addressed despite its important role in daily operation and control. In [52], contingency analysis is provided with artificial neural network with the requirement of a large amount of training based on CPF results.

2.2 Voltage Stability Control

Sensitivity analyses for voltage stability assessment (VSA) and control have been widely discussed in the literature. In [53], Begovic and Phadke derived the sensitivities of total generated reactive power w.r.t. power injection at various locations. In [43], Greene, Dobson, and Alvarado propose a general formula of LMS w.r.t. arbitrary parameters (including load shedding, reactive compensation, and generator re-dispatch). The same authors present a computationally efficient sensitivity of the transfer capability w.r.t. the arbitrary parameters in [54]. In more recent work [55], Capitanescu and Van Cutsem proposes a unified sensitivity analysis of voltage and extends applicable sensitivity to not only bifurcation points, but also low yet stable voltages. A novel LM to MVA sensitivity ranking algorithm is proposed in [56], which will identify severe single branch outages. In [57], sensitivity analysis combing linear sensitivities and eigenvalue analyses is studied for the purpose of voltage contingency rankings. Sensitivities are most useful for

voltage stability control applications [58]–[61] where the sensitivities w.r.t. control actions greatly simplify the nonlinear optimal control problems by linearized model of voltage stability/security constraints.

Though the efficiency of the computation of LM or similar voltage stability margins has been improved, the calculation of these model-based sensitivities requires detailed system model, Jacobian matrix, and calculation of eigenvalues. Therefore, such model-based sensitivities may not be good candidates for online applications.

Recently, measurement-based VSA and control methods utilizing phasor measurement units (PMU) have demonstrated great potentials for online applications. These methods estimate the Thevenin equivalent (TE) circuits for individual load buses directly from measurements and assess the stability margins; otherwise, these actions take control based on simplified TE circuits. The efficiency is significantly improved when compared with model-based VSAs. However, an efficient measurement-based LMS has not yet been studied.

CHAPTER 3

A COMPARATIVE STUDY OF MEASUREMENT-BASED THEVENIN EQUIVALENTS IDENTIFICATION METHODS

This chapter presents a comparative study of measurement-based Thevenin equivalents identification methods. For various measurement-based techniques, the fundamental idea behind them is to identify the Thevenin equivalents (TE) of the outer system seen from the nodes/areas of interests, and then assess the voltage stability margin based on the equivalent circuits. Therefore, fast and accurate identification of the TE is crucial for such online monitoring applications. Though several identification methods have been proposed claiming to achieve good performance, they have not been explicitly compared with each other. This work presents an analogous comparative study of four different methods. After a brief introduction, the four methods are compared in the aspects of time complexity and measurement needed by using an algorithm analysis. Then they are tested on the measurements generated from time domain simulations of the Northeast Power Coordinating Council (NPCC) 140-bus system. Following the case study, a detailed performance analysis is given, and the results can serve as a general guidance on choosing the TE identification methods and the corresponding parameters.

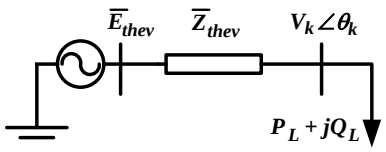

Figure 2. Simple 2-bus electric system.

3.1 Thevenin Equivalence and Impedance

Consider a simple 2-bus electric circuit shown in Figure 2 The load bus k is connected with a load of $\bar{S}_k = P_L + jQ_L$ and has a voltage of $\bar{V}_k$. The generator bus has a voltage of $\bar{E}_{Th}$ and is a connected bus through Thevenin impedance $\bar{Z}_{Th}$ with the load.

The following equation holds for the circuit.

$$\bar{I}_k^* = \bar{S}_k / \bar{V}_k = (\bar{E}_{Th} - \bar{V}_k)^* / \bar{Z}_{Th}^* \tag{3-1}$$

It can be rewritten as

$$V_k^2 - \bar{E}_{Th}^* \cdot \bar{V}_k + \bar{S}_k \cdot \bar{Z}_{Th}^* = 0 \tag{3-2}$$

For a given load, there are, at most, 2 voltage solutions for bus k. If you continue increasing the load from 0, maximum transfer will occur when there is only one voltage solution. It is when

$$V_k = \bar{E}_{Th}^* / 2 \tag{3-3}$$

$$\bar{Z}_{Th}^* = V_k^2 / \bar{S}_k = \bar{Z}_k^* \tag{3-4}$$

Equation (3-4) indicates that when the system reaches the maximum transfer limit, the load impedance matches the Thevenin impedance. Beyond this point, the system is voltage unstable. With regard to a load bus in a more complex power system, if the TE circuit of the rest of the system can be identified, the impedance matching criterion derived from the simple 2-bus system can be used to assess the voltage stability margin.

3.2 Thevenin Equivalents Identification Methods

Given the set of measurements, there is more than one method to identify the TEs. In this section, four of the various identification methods are introduced in the order of the time they first appeared in literature.

3.2.1 Least Squares (LS) Method

Rewrite equation (3-1) as:

$$\bar{E}_{Th} = \bar{V}_k + \bar{Z}_{Th}\bar{I}_k \tag{3-5}$$

Denote $\bar{E}_{Th} = E_r + jE_i$, $\bar{V}_k = u + jw$, and $\bar{I}_k = g + jh$. Equation (3-5) can be expressed in matrix form

$$\begin{bmatrix} 1 & 0 & -g & h \\ 0 & 1 & -h & -g \end{bmatrix} \times \begin{bmatrix} E_r \\ E_i \\ R_{Th} \\ X_{Th} \end{bmatrix} = \begin{bmatrix} u \\ w \end{bmatrix} \tag{3-6}$$

In (3-6), *g*, *h*, *u*, and *w* are known variables from the measurement. E_r, E_i, R_{Th}, and X_{Th} are unknowns representing the TE. The format in (3-6) resembles the basic state estimation problem. However, one set of measure (*g*, *h*, *u*, *w*) will not give an estimation of TEs since there are four unknowns and two equations.

The assumption that the TE remains constant for a short time window is made for solving (3-6). When there are N sets of measurements in the time window, there are 2N equations and still four unknown variables. Least squares (LS) method is often used to solve the TE.

3.2.2 Method Based on Tellegen's Theorem (TT)

This method is derived based on Tellegen's theorem (TT), or more precisely based on the different forms of TT.

$$\hat{I}^T \Delta U - \hat{U}^T \Delta I = 0 \tag{3-7}$$

where ΔU and ΔI represent the changes in the voltage and current phasors of all the branches and buses of the incremented network, and $\hat{U}$ and $\hat{I}$ are the voltage and current phasors of all the branches and buses of the adjoint network. The incremented network is a base-case network subject to either: 1) power change in a given bus, or 2) power system network modification. The adjoint network should be topologically identical to the increment network for (3-7) to hold.

A two-bus adjoined network $\hat{N}$ may be constructed as in Figure 2. The original Thevenin network, *N*, is obviously topologically identical to $\hat{N}$. Therefore, (3-7) can be applied to the artificially constructed adjoint network and to the TE circuit. Furthermore, let the adjoint network have the measurements of the base-case network. By simple substitution, maximum transfer limit of the adjoint network is reached when

$$\begin{gathered} \hat{Z}_{Th} = \hat{Z}_k \\ \left|\Delta U_k / \Delta I_k\right| = \left|U_k / I_k\right| \end{gathered} \tag{3-8}$$

In order to avoid the case ΔI becoming close to zero, a threshold of ε is introduced. If ΔI is greater than ε, Thevenin impedance is updated. If not, the Thevenin impedance remains unchanged.

A simple normalized impedance-stability index (ISI) is defined according to (8) in [5]. In our comparative study, simply comparing the magnitude of the impedance should be sufficient.

3.2.3 Adaptive Method (AD)

This method was proposed by Corsi *et al*. in 2008 [33]. The assumption of $R_{Th} \approx 0$ is made for the reason that $X_{Th} \gg R_{Th}$ for high voltage level buses. By neglecting R_{Th}, (3-5) can be rewritten into two equations.

$$E_{Th} \cos\beta = V_k \cos\theta \tag{3-9}$$

$$E_{Th} \sin\beta = X_{Th} I_k + V_k \sin\theta \tag{3-10}$$

However, there are still three unknown variables, but only two equations. The idea behind the adaptive method is to first give an estimation of E_{Th}; second, solve the Thevenin equivalent accordingly; then adaptively update the E_{Th}, depending on the difference between X_{Th} of two consecutive time stamps.

To give an initial estimation of E_{Th}, two upper and lower bound are calculated.

$$E_{Th}^{0} = (E_{Th}^{\max} + E_{Th}^{\min})/2 \tag{3-11}$$

where $E_{Th}^{\min} = V_k$ and $E_{Th}^{\max} = V_k \cos\theta / \cos\beta$.

The algorithm can be expressed as follows:

Step 1) Estimate E_{Th}^{0} according to (3-11)

Step 2) Calculate X_{Th}^{0} and β^{0}

Step 3) Calculate E_{Th}^{i} according to the conditions:

If $dZ_k^i \cdot dX_{Th}^i < 0$ then $E_{Th}^i = E_{Th}^i + \varepsilon_E$

If $dZ_k^i \cdot dX_{Th}^i > 0$ then $E_{Th}^i = E_{Th}^i - \varepsilon_E$

If $dZ_k^i = 0$ then $E_{Th}^i = E_{Th}^i$

Step 4) Calculate X_{Th}^i and β^i

Step 5) Increment *i* and go to Step 3

where $dZ_k^i = Z_k^i - Z_k^{i-1}$ and $dX_{Th}^i = X_{Th}^i - X_{Th}^{i-1}$. X_{Th}^{i*} is an intermediate evaluation of X_{Th}^i that takes into account the V_k^i, I_k^i, X_{Th}^{i-1}, and β^{i-1}, $\varepsilon_E = \min(\left|E_{Th}^{i-1} - V_k^i\right|, \left|E_{Th}^{i-1} - E_{Th}^{\max}, k \cdot E_{Th}^{i-1}\right|)$, with *k* being a pre-specified parameter.

3.2.4 Method Based on Coupled Single-Port Circuit (CP)

In [7], the power system is modeled as a multi-port network. All the generators and load buses are brought outside of the network. The branches and the tie bus—the buses with no current injection—are modeled inside the network. The system can be described by

$$\begin{bmatrix} -I_L \\ 0 \\ I_G \end{bmatrix} = [Y] \begin{bmatrix} V_L \\ V_T \\ V_G \end{bmatrix} = \begin{bmatrix} Y_{LL} & Y_{LT} & Y_{LG} \\ Y_{TL} & Y_{TT} & Y_{TG} \\ Y_{GL} & Y_{GT} & Y_{GG} \end{bmatrix} \begin{bmatrix} V_L \\ V_T \\ V_G \end{bmatrix} \tag{3-12}$$

where the *Y* matrix is the system admittance matrix, *V* and *I* are vectors of voltage and current phasors, and the subscript *L*, *T*, and *G* represent load bus, tie bus, and generator bus, respectively.

Eliminate the voltage vectors of the tie buses by

$$
\begin{aligned}
V_L &= KV_G - Z_{LL} I_L \\
Z_{LL} &= (Y_{LL} - Y_{LT} Y_{TT}^{-1} Y_{TL})^{-1} \\
K &= Z_{LL} (Y_{LT} Y_{TT}^{-1} Y_{TG} - Y_{LG})
\end{aligned}
\tag{3-13}
$$

For load bus *k*, we can obtain

$$
\begin{aligned}
&V_{Lk} = E_{eqk} - (Z_{eqk} + Z_{couple-k}) I_{Lk} \\
&E_{eqk} = \left[KV_G\right]_k, Z_{eqk} = Z_{LL_{kk}}, Z_{couple-k} = \sum_{i=1, i \neq k}^{n} Z_{LL_{ik}} \frac{I_{Li}}{I_{Lk}}
\end{aligned}
\tag{3-14}
$$

By modeling the coupling effect of other loads into $Z_{couple\text{-}k}$, the TE can be found through the first equation in (3-14). The Thevenin voltage is determined by the generator terminal voltage through matrix *K*. The Thevenin impedance is determined by the diagonal element of Z_{LL} and the coupling of other loads through the network.

Assume measurements of voltage phasors at all generator terminals, as well as voltage and current phasors at load bus *k*, are available from PMUs, and that the system admittance matrix is also available. The TE seen from bus *k* can be calculated using (3-14).

For equation (3-14) to hold, it is assumed that all the loads are increasing at the same rate, which will leave the current ratio of two load buses at nearly constant.

3.3 Analysis of Algorithms

If compared with traditional model-based analyses, all the methods introduced in Section II obviously need less computation effort. They all have simple computation processes and are good candidates for online implementation. In this section, the time complexity and measurement needed of the four methods will be analyzed and compared with each other.

Without loss of generality, we assume the systems of interest have N buses. There are N_G generator buses, N_T tie buses, and N_L load buses, respectively. The measurements needed and the time complexities to calculate the TE for M load buses at one time step are considered.

3.3.1 Least Squares (LS) Method

To calculate the TE of M load buses, all the M load buses should be equipped with PMUs.

The computation time is closely related to the size of the time window, W. Typically, the time window will be several seconds. If there are 30 measurements per second, W will be around 100. The core of LS is to calculate the over-determined linear system represented in (3-6). Rewrite (3-6) as $Ax = b$, where A is a $2W \times 4$ matrix, x is a 4×1 vector, and b is a $2W \times 1$ vector. Using LS, $x = (A^TA)^{-1}A^Tb$. It takes $O(4 \cdot 2w \cdot 4)$ to multiply A^T by A, $O(4 \cdot 2w)$ to multiply A^T by b, and $O(4^3)$ to compute the LU factorization of A^TA and use that to compute the last product. Asymptotically, the run time is $O(W)$. Therefore, the time complexity for calculating M load buses are $O(MW)$.

3.3.2 Method Based on Tellegen's Theorem (TT)

This method is also based on local measurements and will need M PMUs to be installed on the M load buses.

Despite pages of theorems and proofs behind this method, it simply uses the equations in (3-8) to calculate Thevenin impedance from measurements, and then

calculates the Thevenin voltage using (3-5). The run time of one load bus is O(1), and the run time of M load buses will be O(M).

3.3.3 Adaptive Method (AD)

Similarly to the previous two methods, AD will also need M PMUs to be installed on the M load buses.

Though, in every time step, $E_{Th}^{\max}$ will be calculated and there are a few conditional statements to update the E_{Th}. The run time for one load bus is still O(1), and the run time for M load buses will be O(M).

3.3.4 Method Based on Coupled Single-Port Circuit (CP)

For the CP method, monitoring the M load buses in addition to the installation of M PMUs on the corresponding load buses, N_G PMUs need to be installed on all the generator buses. Therefore, the total number of PMUs is M+N_G. Also, the CP method will need the system admittance matrix from the supervisory control and data acquisition (SCADA) system.

As for computational time, the calculation of K matrix in (3-13) serves as an overhead. The K matrix will not change until there is a change of topology or generator status. The time complexity of calculating K matrix is O(N^3), considering that N_G, N_T, and N_L = O(N).

After the K matrix is updated, the Thevenin voltage for a load bus k can be calculated according to (3-14). The run time is O(N_G) for one bus, then it takes O(1) time

to calculate the impedance. Therefore, this part takes O(N_G) for a single load bus and O(MN_G) for an M load bus.

To sum up this section, LS, TT, and AD methods will need PMUs installed at the buses to be monitored; CP methods will need extra PMUs installed at all generator buses.

As for time complexity, TT and AD methods are both O(M) for calculating M load buses at one time step. The run time of LS and CP methods depends on specific problems. However, for CP method, an overhead of O(N^3) will potentially become a burden for a large system.

3.4 Case Studies

All four methods are tested on the NPCC 140-bus system [62]. The system consists of 48 generators, 140 buses, and 223 transmission lines. In the base case, the NPCC system has a total load of 27.7 GW and 4.3 GVar, among which Area 1—the New England region—has a total load of 5048 MW and 1161 MVar. The base case of NPCC system is stressed intentionally for the purpose of creating the voltage collapse scenario.

Measurements are from time-domain simulations of the test system using the TSAT software from DSA Tools. Time-domain simulation will capture the slow dynamics of generators and exciters, which significantly contribute to voltage instability. While some of the methods were tested on power flow results, the performance under the time-domain simulation will be more realistic.

Excessive loading in multiple locations often causes voltage collapse, and the Western Electricity Coordinating Council (WECC) guideline [63] suggests ramping up all loads of the study area in the simulation. In our study, continuously increasing loads

of multiple locations is used to simulate the voltage collapse scenario. Two scenarios have been created. In Scenario 1, all loads at Area 1—the New England region—are ramping up at the rate of 6 MW and 1.2 MVar per second, starting from 5 seconds until collapsing. In Scenario 2, all the loads of the NPCC system are ramping up at the rate of 6 MW and 1.2 MVar per second, starting from 5 seconds until collapsing. The New England region is reported to suffer from voltage instability and is therefore chosen as the area of load increasing in Scenario 1.

The voltages of 10 selected buses in the voltage collapse of Scenario 1 and Scenario 2 are shown in Figure 3 and Figure 4, respectively. For Scenario 1, it is seen that the system collapses at 212 seconds. The loads in Area 1 increase 1242 MW and 248.2 MVar—roughly 20% of the Area 1 load—before reaching the collapsing point. As for Scenario 2, the collapse happens at 437 seconds when loads of all areas have increased 2622 MW and 524.4 MVar—roughly 10% of the load of all areas.

The measurements used to test the TE identification methods are from the two simulation scenarios. A sampling rate of 30 stamps per second for PMUs is assumed. The integration step of the time domain simulation is 0.0167 second, which gives 60 data per second. Only half of the data is chosen as the pseudo measurement.

3.4.1 Scenario 1 Test Results

In the case study, measurements from all the load buses in Area 1 are tested using the four methods. Test results on measurements from different load buses yield similar results in monitoring the stability margin. Therefore, due to limited space, only the test results of measurements at Bus 31 are presented. Bus 31 is chosen as the load bus to

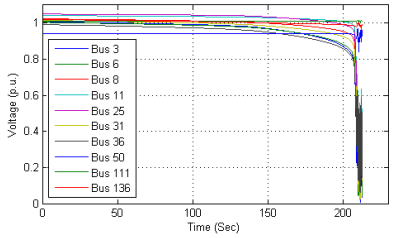

Figure 3. Voltages of selected buses of Scenario 1.

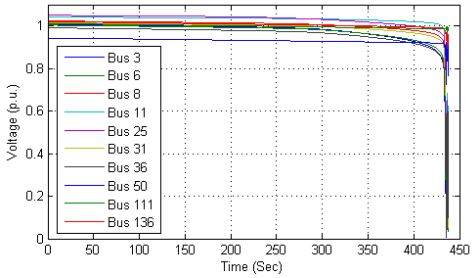

Figure 4. Voltages of selected buses of Scenario 2.

monitor the voltage stability because it is the second largest load bus in Area 1, and it is at the boundary of Area 1 that connects to the remaining system.

Only the results of the Thevenin impedances are shown. The Thevenin impedance and Thevenin voltage depend on each other through (5). The same values of Thevenin impedance will lead to the same values of Thevenin voltage when measurements are the same. The results of the four methods are shown in Figure 5 through Figure 8, respectively.

The results of LS method and TT method are very close to each other. According to Figure 5 and Figure 6, in the beginning, the Thevenin impedance is around 10 times smaller than the load impedance. As the load increases, the load impedance decreases, while at the same time, the Thevenin impedance increases. At 210 seconds, the Thevenin impedance and the load impedance match each other, which coincides with the voltage collapse.

The Thevenin impedance calculated by the AD method is consistently increasing after the initializing phase in the first 10 seconds. However, the impedance is much smaller compared with the impedances calculated by the first two methods. Moreover, it captures the little jumps around second 110 and second 130, which are also captured in the first two methods. However, in the final seconds, there is still a relatively large gap between the load and Thevenin impedances.

The fact that Thevenin impedance does not hold constant is mainly because only the load in Area 1 is ramping up, but other loads remain constant. The idea shown in (14), which represents the other loads in the impedance, is not very reliable considering the

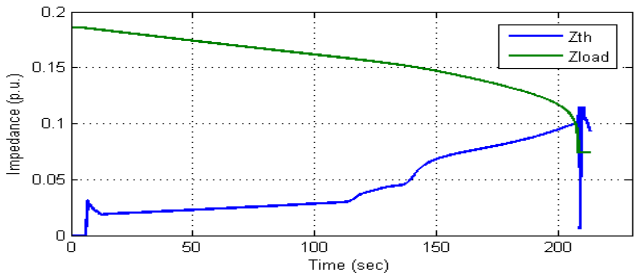

Figure 5. Thevenin impedance of LS method for Scenario 1.

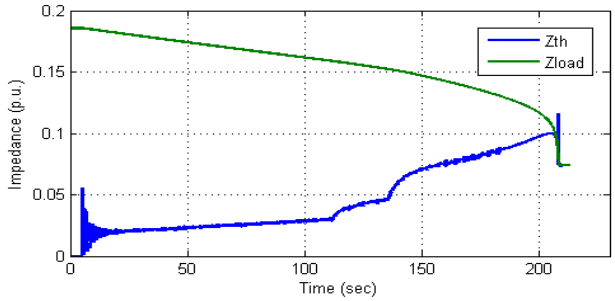

Figure 6. Thevenin impedance of TT method for Scenario 1.

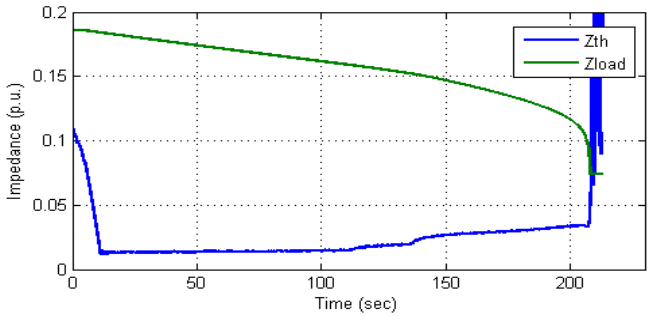

Figure 7. Thevenin impedance of AD method for Scenario 1.

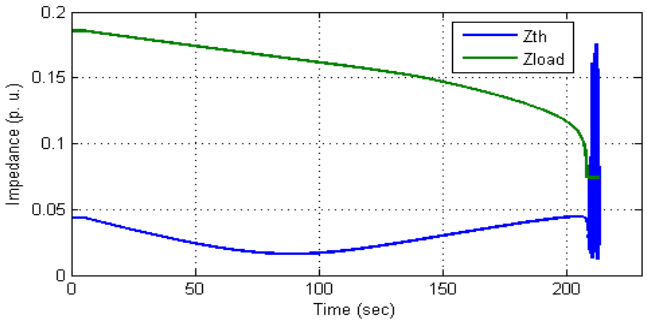

Figure 8. Thevenin impedance of CP method for Scenario 1.

ratio of currents of other loads outside Area 1 to the current of load Bus 31 will change significantly during the simulation.

3.4.2 Scenario 2 Test Results

The calculated Thevenin impedances of the four methods are presented in Figure 9 through Figure 12. The performance of the LS method is consistent with Scenario 1, as shown in Figure 9. Thevenin impedance matches load impedance slightly before the collapse happens.

The TT method, as shown in Figure 10, successfully indicates the voltage collapse. However, there are significant variations in the calculated Thevenin impedances of adjacent time stamps. The variation for Scenario 2 is much more severe compared with the curve shown in Figure 6, where the variation can hardly be noticed. The reason is that the ΔI between 2 nearby time step in Scenario 2 is generally smaller than Scenario 1, which makes $\Delta U / \Delta I$ more sensitive. Though the absolute values of load ramping rates are identical, the load ramping rate for a specific load bus in Scenario 2 is smaller than that in Scenario 1 because more loads are sharing the load ramping. The average ΔI is 4.38e-4 in Scenario 1. In Scenario 2, this value is 1.1067e-4, approximately one fourth of the value computed in Scenario 1. Meanwhile, the threshold ε is set as 5e-5 in both cases.

A possible solution to smooth the variation is to increase ε a little, hoping to limit cases wherein a small number is being divided. Figure 13 shows the results when ε is set as 1e-4, which is twice the previous value. This way, the TT method loses track of the Thevenin impedance in the first 290 seconds. Even for the Thevenin impedance that the

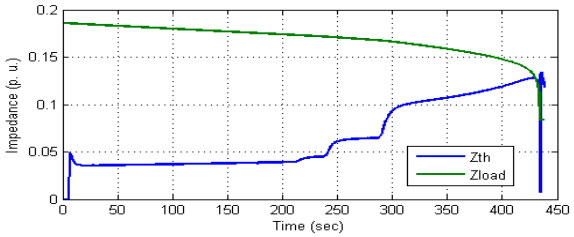

Figure 9. Thevenin impedance of LS method for Scenario 2

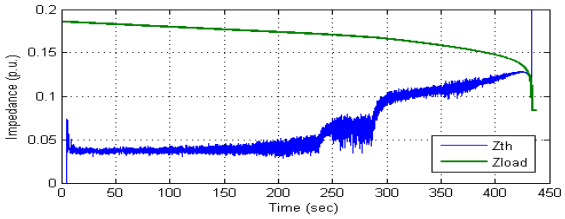

Figure 10. Thevenin impedance of TT method for Scenario 2

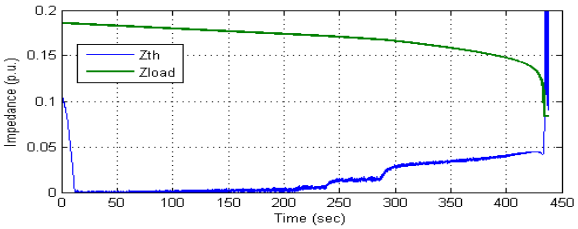

Figure 11. Thevenin impedance of AD method for Scenario 2

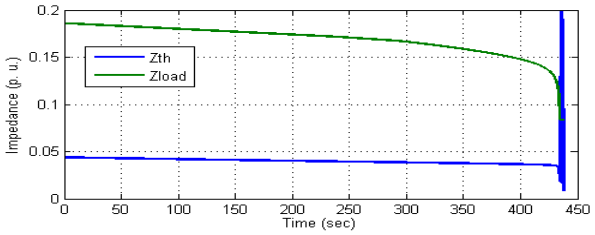

Figure 12. Thevenin impedance of CP method for Scenario 2

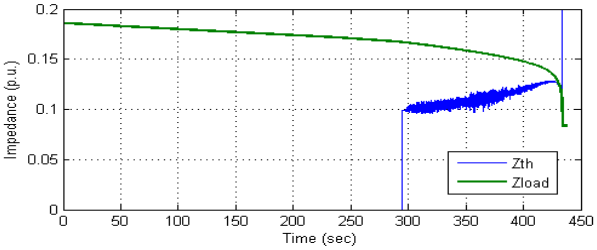

Figure 13. Thevenin impedance of TT method with ε set as 1e-4.

TT method detects, the variations still exist with no signs of relieving. From this case, increasing the threshold value does not smooth the curve but may lose track of the slower change of Thevenin impedance.

According to Figure 9, the performance of the AD method is similar to Scenario 1. The calculated Thevenin impedance is smaller than the values calculated by the LS and TT methods. In the final seconds, the AD method still indicates a relatively large margin for voltage stability. A possible explanation is that the assumption $X_{Th} \gg R_{Th}$ is significantly erroneous in this case. In fact, Figure 14 shows the Thevenin resistance and reactance calculated by the LS method, at which point the reactance dominates the resistance in the beginning. However, as load increases, the resistance increases faster and becomes greater than the reactance after 300 seconds.

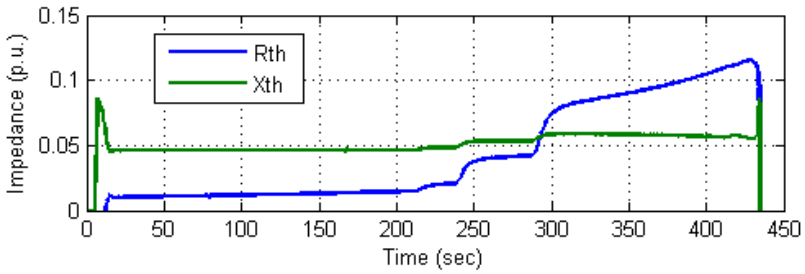

Figure 14. Resistance vs reactance using LS method for Scenario 2.

As for the CP method, the Thevenin impedance is almost constant throughout the simulation with some slight decrease. The idea of integrating the other load into the Thevenin impedance works well in this case. However, it does not indicate the voltage collapse that occurs in the end.

3.5 Conclusion

In this chapter, four TE identification methods (i.e., least squares method (LS), Tellegen's theorem method (TT), adaptive method (AD), and coupled single-port circuit method (CP)) are compared theoretically and on the NPCC test system. The analysis of the algorithms of the four methods provides a comparison of the time complexity and requirements for PMU availability. The case study on the two voltage collapse scenarios of the NPCC system tests the ability of the four methods in monitoring the system collapse point. In this particular case study, LS and TT methods successfully indicate the system collapse, while AD and CP methods fail to do so. Further analysis of the performance of the four methods is given in Chapter 3.4. Though one cannot evaluate the methods based on the performance of one particular system, the general analysis can provide guidance for researchers interested in choosing one of the four methods according to their own.

CHAPTER 4

HYBRID VOLTAGE STABILITY ASSESSMENT (VSA) FOR N-1 CONTINGENCY

The existing measurement-based VSA deals with the normal case, but not any contingency case because there is no measurement data for a contingency case which is hypothetical. In this chapter, a hybrid VSA method is proposed based on both model-based and measurement-based techniques. First, an enhanced model-based sensitivity analysis estimating the post-contingency status is proposed, and then it is combined with the measurement-based Thevenin equivalent approach. The proposed sensitivity analysis has the feature of simplicity, which is aligned with the measurement-based Thevenin equivalent. Test results with the IEEE 14, 39, and 118-bus system show that the proposed sensitivity is highly accurate in estimating N-1 contingency system variables and the proposed hybrid VSA method for N-1 contingency captures the insecure contingencies successfully. The proposed method greatly broadens the practical application of PMUs for VSA under N-1 contingency.

4.1. Sensitivities for Calculating Post-Contingencies Variables

In previous sensitivity analyses for transmission contingency, a line outage is typically transformed to changes of bus injections. Different transformations were introduced in the literature [41] [42], as previously mentioned. In this section, a new transformation is proposed with a rigorous mathematical proof, and the outage sensitivity factors based on the transformation are developed.

4.1.1 Proposed Transformation and Proof of Equivalence

As shown in Figure 15, System *A* is a system in normal state, with a line flow S_{mn} from bus *m* to bus *n* and S_{nm} from bus *n* to bus *m*. The rest of the system is not shown for simplicity. System A^c is the post contingency case of System *A* after the line *mn* outage where the superscript c stands for contingency. System *B* has the same settings as System *A*, except that System *B* does not have branch *mn*. Also, the bus injection at bus *m* is S_m^{inj} -S_{mn} and the bus injection at bus n is S_n^{inj}-S_{nm}, where S_m^{inj} and S_n^{inj} are the bus injections at bus *m* and *n*, respectively, in System *A*. System B^c is the post contingency status case of System B when S_{mn} and S_{nm} are added to Bus *m* and *n*, respectively.

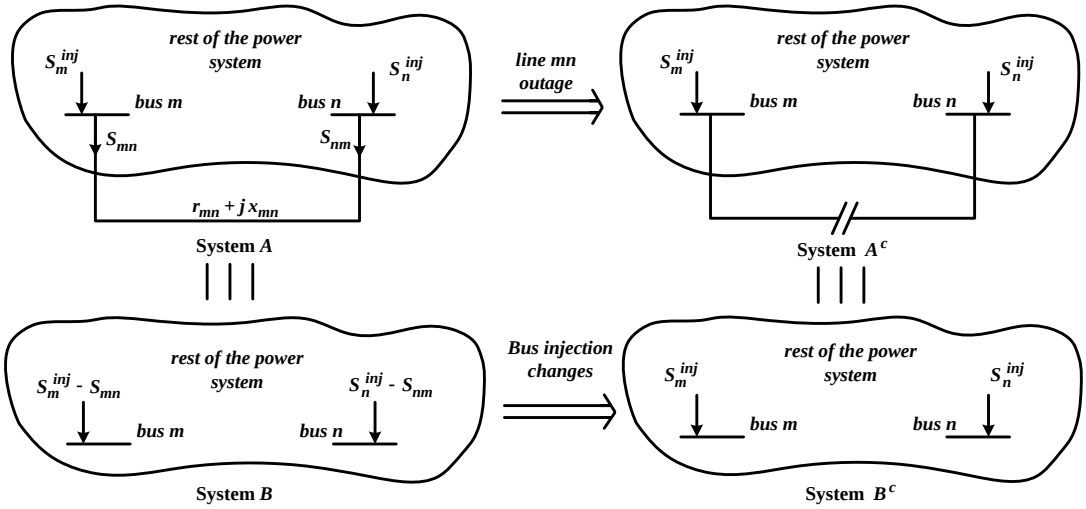

Figure 15. Proposed transformation.

The proposed transformation is to transform System *A* to System *B*, then use System *B* to predict System B^c by changing the bus injections at buses *m* and *n*, and finally transform System B^c to System A^c which represents the post-contingency status of

interest. In other literatures, similar transformations were raised but not proven. Though achieving acceptable accuracy, these transformations are not necessarily rigorous till proven. The Proof of the equivalence between Systems *A* and System *B* as well as that that between Systems A^c and B^c is given next.

For a power system, the nodal power equations are:

$$\Delta P_i = P_i^{inj} - V_i \sum_{j=1}^{N} V_j Y_{ij} \cos(\theta_i - \theta_j - \phi_{ij}) = 0 \tag{4-1}$$

$$\Delta Q_i = Q_i^{inj} - V_i \sum_{j=1}^{N} V_j Y_{ij} \sin(\theta_i - \theta_j - \phi_{ij}) = 0 \tag{4-2}$$

where

$i = 1 \sim N$ where N is the number of buses in the system;

V_i (or V_j) is the voltage magnitude of bus i (or j);

θ_i (or θ_j) is the voltage angle at bus i (or j);

P_i^{inj} (or Q_i^{inj}) is the real (or reactive) injection at bus i; and

Y_{ij} (or ϕ_{ij}) is the magnitude (or angle) of the element in the system admittance matrix.

Assume N_{PQ} is the number of PQ buses and N_{PV} is the number of PV buses in the system. Therefore, there will be $2N_{PQ}+N_{PV}$ unknown variables: voltage angles for $N_{PQ}+N_{PV}$ buses and voltage magnitude for N_{PQ} buses. Let the unknown variables be vector $\vec{x}$. Let $\vec{f}(\vec{x}) = \vec{0}$ represent (4-1) of $N_{PQ}+N_{PV}$ buses and (4-2) of N_{PQ} buses. To solve the load flow is to solve

$$\vec{f}(\vec{x}) = \vec{0} \tag{4-3}$$

Assume $\vec{x}_A$ is the load flow solution for System A such that $\vec{f}_A(\vec{x}_A)=\vec{0}$, and $\vec{x}_B$ is the load flow solution for System B such that $\vec{f}_B(\vec{x}_B)=\vec{0}$. Though both System A and B have more than one solution for (3), there is only one feasible solution around 1.0 p.u. voltage magnitude. To prove equivalence is to show $\vec{x}_A=\vec{x}_B$. Since $\vec{x}_A$ and $\vec{x}_B$ are the feasible solution, it is to show $\vec{f}_B(\vec{x}_A)=\vec{0}$. This is the key of the rigorous proof to be presented next.

Assume that the symbols introduced in (4-1) and (4-2) represent the values in System A. Underscores are used to represent the values in System B.

Differences between Systems A and B are as follows:

a) the different nodal injections at buses *m* and *n*; and

b) the branch *mn*.

The first difference will only matter corresponding to (4-1) and (4-2) for buses *m* and *n*. The second difference will only affect Y_{mn} , Y_{nm} , Y_{nn}, and Y_{mm} in the admittance matrix, which also only appear in (4-1) and (4-2) for buses m and n. To sum up, only the equations related to the injections at buses *m* and *n* are different for $\vec{f}_A(\vec{x}_A)=\vec{0}$ and $\vec{f}_B(\vec{x}_B)=\vec{0}$. Therefore, $\vec{f}_B(\vec{x}_A)=\vec{0}$ holds for the equations other than those related to the injections at buses *m* and *n*. Thus, we only need to prove that $\vec{x}_A$ also satisfies the equations related to the injections at buses *m* and *n*.

For the admittance matrix *Y* of System *A*, the element $Y_{ij}=G_{ij}+jB_{ij}$ is given by

$$Y_{ij}=-y_{ij}, i\neq j \tag{4-4}$$

$$Y_{ii} = \sum_{j} y_{ij} + y_{ig} \tag{4-5}$$

$$y_{ig} = j \sum_{Y_{ij} \neq 0} \frac{b_{ijg}}{2} \tag{4-6}$$

where $y_{ij}=g_{ij}+jb_{ij}$ is the admittance of branch ij; y_{ig} is the ground admittance of bus i; and $j \cdot b_{ijg}/2$ is the shunt admittance of line ij.

Again, underscores are used to represent the values in System *B* values. For The elements of the admittance matrix *Y*, the element is given by

$$\underline{Y_{ij}} = Y_{ij}, ij \notin \{mm, nn, mn, nm\} \tag{4-7}$$

$$\underline{Y_{mn}} = \underline{Y_{nm}} = 0 \tag{4-8}$$

$$\underline{Y_{mm}} = Y_{mm} - y_{mn} - jb_{mng} / 2 \tag{4-9}$$

$$\underline{Y_{nn}} = Y_{nn} - y_{mn} - jb_{mng} / 2 \tag{4-10}$$

The line flow between buses *m* and *n* is given by

$$P_{mn} = V_m V_n Y_{mn} \cos(\theta_m - \theta_n - \phi_{mn}) + V_m^2 g_{mn} \tag{4-11}$$

$$Q_{mn} = V_m V_n Y_{mn} sin(\theta_m - \theta_n - \phi_{mn}) - V_m^2 (b_{mn} + b_{mng} / 2) \tag{4-12}$$

The types of buses m and n will lead to different number of equations. First, consider the situation that both *m* and *n* are PQ buses. We may rewrite the bus injection equations for buses *m* and *n* in System *B*. Thus, the real power injection equation is given by:

$$
\begin{aligned}
\underline{\Delta P_m}(\vec{x}_A) &= \underline{P_m^{inj}} - V_m \sum_{j=1}^{N} V_j \underline{Y_{mj}} \cos(\theta_m - \theta_j - \underline{\phi_{mj}}) \\
&= P_m^{inj} - P_{mn} - V_m \sum_{j=1, j\neq m,n}^{N} V_j Y_{mj} \cos(\theta_m - \theta_j - \phi_{mj}) - V_m{}^2 \underline{Y_{mm}} \cos(\underline{\phi_{mm}}) \\
&\quad - V_m V_n \underline{Y_{mn}} \cos(\theta_m - \theta_n - \underline{\phi_{mn}}) \\
&= P_m^{inj} - P_{mn} - V_m \sum_{j=1}^{N} V_j Y_{mj} \cos(\theta_m - \theta_j - \phi_{mj}) + V_m{}^2 Y_{mm} \cos(\phi_{mm}) + V_m V_n Y_{mn} \cos(\theta_m - \theta_n - \phi_{mn}) \\
&\quad - V_m{}^2 \underline{Y_{mm}} \cos(\underline{\phi_{mm}}) - V_m V_n \underline{Y_{mn}} \cos(\theta_m - \theta_n - \underline{\phi_{mn}}) \\
&\overset{(1)}{=} - P_{mn} + V_m{}^2 Y_{mm} \cos(\phi_{mm}) + V_m V_n Y_{mn} \cos(\theta_m - \theta_n - \phi_{mn}) - V_m{}^2 \underline{Y_{mm}} \cos(\underline{\phi_{mm}}) \\
&\quad - V_m V_n \underline{Y_{mn}} \cos(\theta_m - \theta_n - \underline{\phi_{mn}}) \\
&\overset{\underline{Y_{mn}}=0}{=} - P_{mn} + V_m{}^2 (G_{mm} - \underline{G_{mm}}) + V_m V_n Y_{mn} \cos(\theta_m - \theta_n - \phi_{mn}) \\
&\overset{(9)}{=} - P_{mn} + V_m{}^2 (g_{mn}) + V_m V_n Y_{mn} \cos(\theta_m - \theta_n - \phi_{mn}) \\
&\overset{(11)}{=} 0
\end{aligned}
\tag{4-13}
$$

The reactive power injection equation is given by:

$$
\begin{aligned}
\underline{\Delta Q_m}(\vec{x}_A) &= \underline{Q_m^{inj}} - V_m \sum_{j=1}^{N} V_j \underline{Y_{mj}} \sin(\theta_m - \theta_j - \underline{\phi_{mj}}) \\
&= Q_m^{inj} - Q_{mn} - V_m \sum_{j=1, j\neq m,n}^{N} V_j Y_{mj} \sin(\theta_m - \theta_j - \phi_{mj}) - V_m{}^2 \underline{Y_{mm}} \sin(\underline{\phi_{mm}}) \\
&\quad - V_m V_n \underline{Y_{mn}} \sin(\theta_m - \theta_n - \underline{\phi_{mn}}) \\
&= Q_m^{inj} - Q_{mn} - V_m \sum_{j=1}^{N} V_j Y_{mj} \sin(\theta_m - \theta_j - \phi_{mj}) + V_m{}^2 Y_{mm} \sin(-\phi_{mm}) + V_m V_n Y_{mn} \sin(\theta_m - \theta_n - \phi_{mn}) \\
&\quad - V_m{}^2 \underline{Y_{mm}} \sin(-\underline{\phi_{mm}}) - V_m V_n \underline{Y_{mn}} \sin(\theta_m - \theta_n - \underline{\phi_{mn}}) \\
&\overset{(2)}{=} - Q_{mn} + V_m{}^2 Y_{mm} \sin(-\phi_{mm}) + V_m V_n Y_{mn} \sin(\theta_m - \theta_n - \phi_{mn}) - V_m{}^2 \underline{Y_{mm}} \sin(-\underline{\phi_{mm}}) \\
&\quad - V_m V_n \underline{Y_{mn}} \sin(\theta_m - \theta_n - \underline{\phi_{mn}}) \\
&\overset{\underline{Y_{mn}}=0}{=} - Q_{mn} + V_m{}^2 (-B_{mm} - \underline{B_{mm}}) + V_m V_n Y_{mn} \sin(\theta_m - \theta_n - \phi_{mn}) \\
&\overset{(9)}{=} - Q_{mn} - V_m{}^2 (b_{mn} + b_{mng/2}) + V_m V_n Y_{mn} \sin(\theta_m - \theta_n - \phi_{mn}) \\
&\overset{(12)}{=} 0
\end{aligned}
\tag{4-14}
$$

Substituting *m* with *n* and *n* with *m* in (4-13) and (4-14), we have

$$\underline{\Delta P}_n(\bar{x}_A) = 0 \tag{4-15}$$

$$\underline{\Delta Q}_n(\bar{x}_A) = 0 \tag{4-16}$$

If we combine (4-13) and (4-16), $\vec{f}_B(\vec{x}_A) = \vec{0}$ is true. Thus, System *A* and System *B* are mutually equivalent from the viewpoint of steady-state power flows.

If bus *m* or bus *n* is a PV bus, then Eq. (4-2) considering the reactive power injection for that bus cannot be included in the formation of $\vec{f}(\vec{x}) = \vec{0}$. If one of the two buses is the slack bus, both equations for real and reactive power injection will not be included in $\vec{f}(\vec{x}) = \vec{0}$. However, the change of bus types will not affect (4-1), (4-2), and (4-4)-(4-12), which will not affect the conclusion that System A and System B are equivalent. As a matter of fact, it only changes the number of unknown variables and equations.

Therefore, it is concluded that System *A* and System *B* are equivalent regardless of the types of buses *m* and *n*.

For System A^c and System B^c, it is seen from Figure 15 that they have the identical topology and bus injections, so they must be equivalent. Besides, if we set line flow *mn* to zero, Systems A and B become A^c and B^c, respectively.

4.1.2 Proposed Sensitivity Based on the Transformation

A commonly used approach to solve nonlinear load flow equations in (4-3) is the Newton-Raphson method. The Jacobian matrix in each iteration is given as follows:

$$J = \frac{\partial f(x)}{\partial x} \tag{4-17}$$

Based on the Jacobian matrix, the sensitivity can be formulated as

$$\Delta\vec{x} = J^{-1}\Delta\vec{f}(\vec{x}) \tag{4-18}$$

where $\Delta\vec{f}(\vec{x})$ is the vector of nodal injection change which is numerally equal to the outage line flow, and $\Delta\vec{x}$ is the change of system variables.

There are two types of outages, generation/load outage and line outage. For the first type, generation or load outages can be directly represented by nodal injection change. Thus, it is not discussed in this dissertation. While for the line outage, various transformations have been explored to represent the line outages in nodal injection change.

Since the equivalence of System *A* and System *B* has been proven, it is natural to transform *A* to *B* by adding the line flow to nodal injection and remove the outage line. Then, by adding nodal change to System *B*, sensitivity based on (4-18) can predict the status of System B^c, which is equivalent to system A^c, the post-contingency case of System *A*.

1.1. Piece-wise-linear Sensitivity Considering Q Limit Violations

Practically, in power flow model, most PV buses have upper and lower limits for reactive power. After a severe contingency, there may be violations of Q limits at some buses, say Bus *x*. If this happens, the PV bus should be considered a PQ bus with the same scheduled P and the scheduled Q set at the violated Q limit. If only the sensitivity of the initial condition is used, Bus *x* will be treated as a PV bus in the post-contingency state. The voltage magnitude will be the same as before. However, after the PV-PQ transition, the voltage magnitude of that bus will drop for lack of reactive supply. This

will cause significant error. Therefore, a piece-wise-linear sensitivity model is proposed next to deal with the PV to PQ transition should be introduced.

First, a new index called Status Change Coefficient Factor, F, is introduced. When a contingency happens, the reactive power of a PV bus may violate either the upper or lower limit. As shown in Figure 16. Status change coefficient factor F, Q_0 is the reactive generation at a bus at normal state and Q_c is the predicted reactive generation using the sensitivity factors derived in this iteration. Q_{upper} and Q_{lower} are the upper and lower limits, respectively, for reactive power generation. The F factor is defined as

$$F = \begin{cases} \dfrac{Q_{upper} - Q_0}{Q_c - Q_0}, \text{Q upper limit is violated} \\ \dfrac{Q_0 - Q_{lower}}{Q_0 - Q_c}, \text{Q lower limit is violated} \end{cases} \tag{19}$$

It is seen from Figure 16 that when the reactive power limits are violated at a specific bus, F for that bus will be between 0 and 1. Assume that $\Delta f(x)$, the hypothetical nodal injection, and Q are linearly related. Then F can be used to identify when the Q limit is first violated at that bus. The smallest F of all buses, say F_j, approximates the point where the first PV bus in the system violates its limit when $F_j \cdot \Delta f(x)$ is applied to the system.

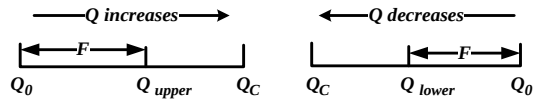

Figure 16. Status change coefficient factor F.

Therefore, the result in the range of [$F_j \cdot \Delta f(x)$, $\Delta f(x)$] (i.e., beyond the point where the first violation occurs) is no longer acceptable. Thus, the original sensitivity can be

applied only in the range of [0, $F_j \cdot \Delta f(x)$] in which the specific bus is considered a PV bus. In the range of [$F_j \cdot \Delta f(x)$, $\Delta f(x)$], the bus is converted from a PV bus to PQ, therefore, the system Jacobian matrix needs to be modified accordingly. After modifying the Jacobian and finding the new sensitivity factors, we may apply the remaining amount of bus injection change, $(1-F_j) \cdot \Delta f(x)$. Then, if we still have another Q violation at a second bus after converting the first PV bus to PQ, then we will have to convert the second PV bus to PQ. Thus, a total of three segments will be identified in the overall range of [0, $\Delta f(x)$]. This process continues until no Q violation is found, after the scheduled Δf(x) is fully applied to the system. The algorithm is illustrated in Figure 17.

4.2 Hybrid Voltage Stability Assessment

Presently, model-based contingency analysis such as continuation power flow (CPF) for voltage stability assessment (VSA) is widely applied to predict voltage stability margin. If applied online, though capable of foreseeing contingencies which may cause voltage instability, such approach requires significant amount of computational resources. Practically, in some utilities, only selected contingencies are analysed on a 15 minutes base.

An alternative approach, measurement based VSA, assesses voltage stability directly based on measurement data. The core technique is to approximate the Thevenin equivalent of the external system based on real-time measurement data and then predict the stability margin by comparing the load bus with its external system.

The 2-bus Thevenin equivalent circuit is shown in Figure 18. The 4 unknown variables are the magnitudes and angles of Thevenin voltage and impedance. A given

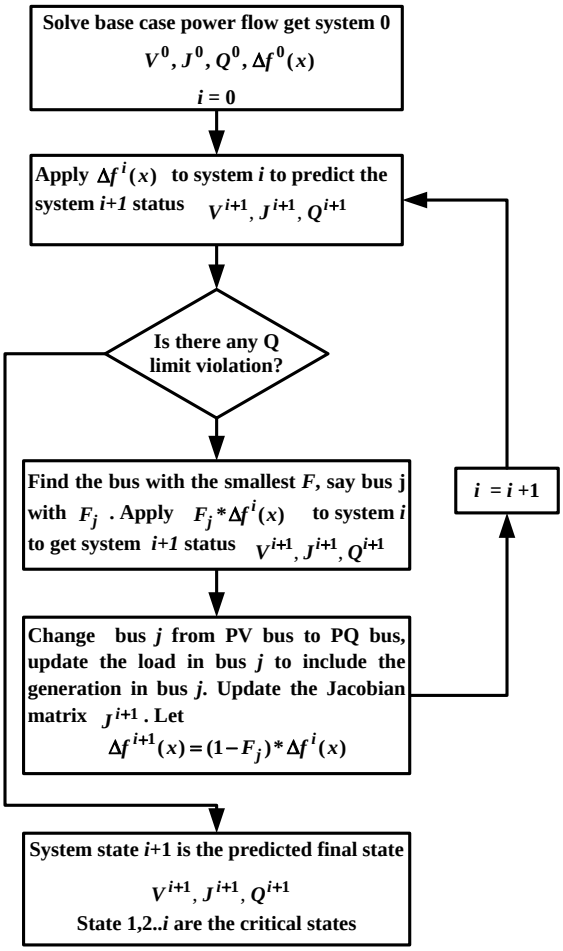

Figure 17. Algorithm considering Q limits.

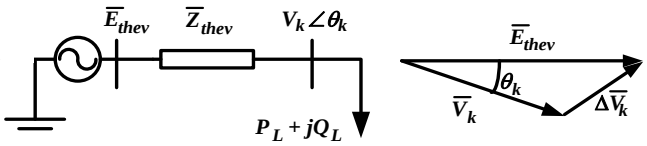

Figure 18. VSI for hybrid VSA.

measurement set at a time stamp will provide two equations using Kirchhoff's law. Therefore, with the assumption that the Thevenin equivalent remains constant in a time frame, two or more sets of measurements will be sufficient in estimating the parameters using Least-Square method.

After the Thevenin equivalent is identified, voltage stability margin can be estimated based on the characteristics of the two-bus circuit. The Voltage Stability Index (VSI) in [13] is employed here to indicate the stability margin. The VSI is formulated in (4-20). When the VSI decreases to 1, the system approaches to the unstable point (i.e., the nose point or the bifurcation point) in typical PV curves.

$$VSI = \left| \frac{V_k}{\Delta V_k} \right| \tag{4-20}$$

Since such approach only uses measurement as input instead of information of the complex system model, the computational burden is small which is desirable for real-time applications. However, due to the lack of system information under N-1 contingency, the capability of this approach has been limited to normal state.

With the contingency sensitivity analysis derived in the previous section, a hybrid VSA method for N-1 contingency is proposed based on a combination of the model-based contingency sensitivity and the measurement-based Thevenin equivalent. Since there is no multiple power flow runs (as opposed to the CPF approach), the hybrid approach is computationally efficient.

The hybrid VSA is shown in Figure 19. In the flow chart: 1) subscript i stands for the bus ID; 2) superscript c_j stands for the j^{th} contingency; 3) N is the total number of

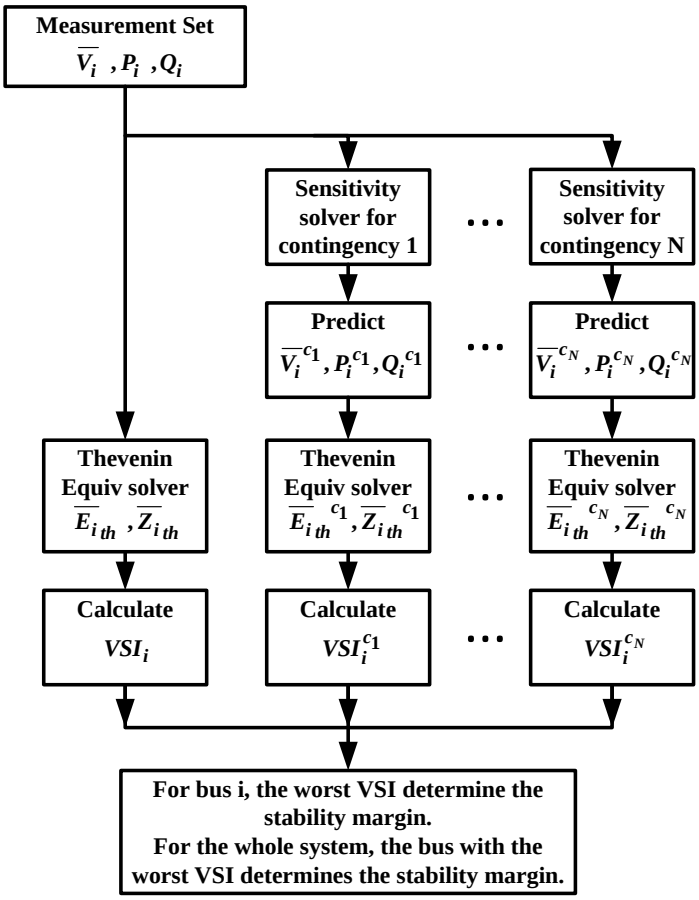

Figure 19. Flowchart of the proposed hybrid VSA.

contingencies; 4) subscript *th* stands for Thevenin equivalence; and 5) VSI stands for voltage stability index, i.e., an index which represents the system voltage stability margin.

The left most branch in Figure 19 is the same as the measurement-based approach in calculating the VSI for bus *i* under normal case (i.e., N-0). The remaining *N* branches in the right are parallel processes to calculate the VSI for *N* single contingency cases.

In each of the parallel branch, the algorithm first calculates the proposed sensitivity factors based on the measurement, i.e., the present system status, and then predicts the post-contingency status. These first two steps are model-based approaches utilizing the system data. After that, it calculates the Thevenin equivalent and provides the VSI for the post-contingency system. These two steps are measurement-based except that the input is not directly from measurement but from predicted post-contingency values.

Note, this method assumes that the system is observable at all studied buses which is aligned with previous works [13] [49]. That is because when calculating the sensitivity, the system status must be known to form the Jacobian matrix.

As long as the prediction of post-contingency cases achieves excellent accuracy, the VSIs for N-1 contingency can provide good references for the system stability margin. Moreover, since both of the prediction process and the measurement-based approach are computationally efficient and highly parallelizable, the whole approach can speed up the process of N-1 contingency analysis and has great potential for online implementation.

4.3 Case Studies

In this section, first, the proposed sensitivity calculation is tested with the IEEE 14-bus system [64] for normal operating condition and is compared with the results from [41] and [42]. The IEEE 14-bus system is chosen for the sensitivity test because it is also the test system used in [41] and [42]. Details such as the bus voltage magnitudes and angles are provided for two severe contingencies under the base case load level. Then, the proposed sensitivity is further tested on the IEEE 14, 39, and 118-bus systems [64] for all possible line outages in the load range between the normal condition and the collapsing point. Finally, the HBVSA is tested on the IEEE 14, 39, and 118-bus systems to demonstrate its ability in online monitoring of the stability margins of N-1 contingencies, when a load increase scenario is studied.

4.3.1 Test of the Proposed Sensitivity on IEEE 14-Bus System

The IEEE 14-bus system which is the test system in [41] and [42] is used to test the sensitivity in this subsection in order to compare the proposed sensitivity calculation with the previous methods. For this system, two contingencies, line 2-4 outage and line 5-6 outage, under normal loading condition are considered.

The first contingency, line 2-4 outage, will not cause any reactive (Q) violation which means it is not a severe contingency. The results from the proposed sensitivity model, as well as the results using two previous methods in [41] and [42], are presented in Table 1 and Table 2 for comparison.

Table 1 shows the predicted voltage magnitudes. The column ‘Exact Value’ lists the exact post-contingency voltage magnitude by re-running the post-contingency power

Table 1: Comparison of Predicted Voltage Magnitude

Bus No	Exact Value	Method in [41]		Method in [42]		Proposed method	
		Predicted	|Error| (%)	Predicted	|Error| (%)	Predicted	|Error| (%)
1	1.0600	1.0600	--	1.0600	--	1.0600	--
2	1.0450	1.0450	--	1.0450	--	1.0450	--
3	1.0100	1.0100	--	1.0100	--	1.0100	--
4	1.0071	1.0093	0.22	1.0079	0.08	1.0070	0.01
5	1.0112	1.0136	0.23	1.0120	0.08	1.0115	0.03
6	1.0700	1.0700	--	1.0700	--	1.0700	--
7	1.0564	1.0575	0.11	1.0567	0.03	1.0563	0.00
8	1.0900	1.0900	--	1.0900	--	1.0900	--
9	1.0504	1.0518	0.13	1.0508	0.04	1.0504	0.00
10	1.0463	1.0475	0.11	1.0466	0.03	1.0463	0.00
11	1.0544	1.0551	0.06	1.0546	0.02	1.0544	0.00
12	1.0548	1.0549	0.01	1.0549	0.00	1.0548	0.00
13	1.0495	1.0497	0.02	1.0495	0.01	1.0495	0.00
14	1.0319	1.0328	0.08	1.0322	0.02	1.0319	0.00
Ave. of |Error| (%)			0.11		0.03		0.00

Table 2: Comparison of Predicted Voltage Angles

Bus No	Exact Value (degree)	Method in [41]		Method in [42]		Proposed method	
		Predict (degree)	|Error| (%)	Predict (degree)	|Error| (%)	Predict (degree)	|Error| (%)
1	0.0000	0.0000	--	0.0000	0.00	0.0000	--
2	-4.5038	-4.6946	4.24	-4.4792	0.55	-4.4805	0.52
3	-14.131	-13.601	3.75	-14.069	0.44	-14.075	0.40
4	-13.234	-12.092	8.62	-13.160	0.55	-13.148	0.65
5	-10.765	-9.9934	7.17	-10.713	0.49	-10.706	0.55
6	-16.593	-15.683	5.49	-16.526	0.41	-16.524	0.42
7	-16.145	-15.062	6.71	-16.074	0.44	-16.064	0.50
8	-16.145	-15.062	6.71	-16.074	0.44	-16.064	0.50
9	-17.646	-16.594	5.96	-17.576	0.39	-17.567	0.44
10	-17.745	-16.718	5.78	-17.676	0.39	-17.668	0.43
11	-17.300	-16.331	5.60	-17.232	0.39	-17.227	0.42
12	-17.475	-16.554	5.27	-17.407	0.39	-17.405	0.40
13	-17.575	-16.645	5.29	-17.508	0.38	-17.505	0.40
14	-18.622	-17.622	5.37	-18.553	0.37	-18.547	0.40
Avg. of |Error| (%)			5.43		0.40		0.43

flow. Although all three methods achieve acceptable results, the proposed method performs even better than the other two.

Note, Bus1 is the slack bus, and Buses 2, 3, and 6 are PV buses. Thus, the error is not applicable to these buses.

Table 2 shows the voltage phase angle of the predicted results. Similarly, the column ‘Exact Value’ comes from the post-contingency power flow. From the table, the proposed method and the method in [42] are very accurate in predicting the angles with an average error of 0.43% and 0.40%, respectively. However, method in [41] is not so accurate at an average error of 5.43%.

From the above results, the proposed method predicts the post-contingency status at a very high accuracy. The performance of the proposed method is very close to the method in [42] when there is no Q limit violation.

The second contingency, line 5-6 outage, is considered a severe contingency because this line has a large volume of power flow under normal case and its outage causes Q limit violation at Bus 6. The approach shown in Figure 17 is employed here to deal the Q limit violation.

Note, since Ref. [41] does not address this Q violation, so it cannot be compared with the proposed sensitivity approach. Also, the approach in [42] is improved and enhanced in this study. Although, rigorously speaking, it is not completely fair to compare the proposed approach with the one in [42], the comparison is carried out to illustrate the advantage of the proposed method. Details are elaborated next.

Before making any further comparison between the proposed method and the one

in [42], it should be mentioned that the exact results of post-contingency status used in the two methods are not the same because of the way the outage is modeled. In [42], with the consideration of line outage, only the series impedance of that branch is taken out. While in this research, both the series impedance and the shunt admittance are taken out when an outage occurs. Since the shunt branch is part of the transmission PI (π) model, it is more reasonable to take out the shunt admittance with the series impedance to model a contingency event.

Consequently, in the prediction of the post-contingency variables, the load injection change used in [42] only considers the line flow through the series impedance. In contrast, the proposed method considers the flow change through the series impedance as well as the shunt admittance, which is more reasonable.

Table 3: Predicted Voltage for Line 5-6 Outage

Bus No	Magnitude (p.u.)			Angle (degree)		
	Exact	Linear	P.W.L.	Exact	Linear	P.W.L.
1	1.0600	1.0600	1.0600	0.0000	0.0000	0.0000
2	1.0450	1.0450	1.0450	-5.1355	-5.0588	-5.0946
3	1.0100	1.0100	1.0100	-13.187	-13.025	-13.107
4	1.0140	1.0206	1.0161	-10.977	-10.897	-10.911
5	1.0243	1.0291	1.0259	-8.6054	-8.5375	-8.5540
6	1.0073	1.0700	1.0195	-27.009	-26.628	-26.383
7	1.0534	1.0693	1.0577	-17.281	-16.911	-17.064
8	1.0900	1.0900	1.0900	-17.281	-16.911	-17.064
9	1.0443	1.0735	1.0515	-20.569	-20.004	-20.257
10	1.0305	1.0671	1.0393	-21.976	-21.450	-21.626
11	1.0159	1.0668	1.0271	-24.555	-24.126	-24.096
12	0.9937	1.0554	1.0061	-27.415	-26.961	-26.799
13	0.9945	1.0544	1.0068	-27.003	-26.527	-26.417
14	1.0029	1.0478	1.0134	-24.368	-23.814	-23.949
Avg. of |Error|		3.69%	0.82%		1.73%	1.43%

The predicted voltages for line 5-6 outage are shown in Table 3. The result from

the algorithm considering Q limits is labelled with “P.W.L.” and that from ignoring Q limits is labelled with “Linear”. Obviously, Table 3 shows the advantage of P.W.L. approach when Q limits are violated.

Ref. [42] presents only the predicted voltage magnitudes which reports an average error of 1.58% compared with the exact value. The proposed scheme has improved the accuracy by 50% in this case. Ref. [42] provides the predicted reactive power generation and line flow whose accuracy is closely related to the accuracy of voltage angles. Thus, the comparison of the predicted reactive power is shown in Table 4 and Table 5. The numerical results show that the proposed method is more accurate than the previous methods. This is reasonable because this work provides a more reasonable outage model than those in the literature.

4.3.2 Extensive Test of the Sensitivity with Three Systems in Broad Load Ranges for All N-1 Contingencies

The previous subchapter provides a detailed study at a particular load level (i.e., the base case load level) for two contingencies for the IEEE 14-bus system, as well as a comparison with the results from the literature. Next, in this subsection, the proposed sensitivity is extensively tested on three different systems (i.e., the IEEE 14, 39, and 118-bus systems) for all branch outages except those causing islands like a branch connecting a generation bus only. Also, the tests are carried out in a broad load range between the base case load and the maximum load at the collapse point.

For each system, the PV curve for normal condition, namely the N-0 case, is first calculated using continuation power flow (CPF). The power flow solutions on the PV

Table 4: Comparison of Predicted Var Generation

Gen No	Method in [42]				Proposed Method			
	Exact (p.u.)	Pred. (p.u.)	|Error|		Exact (p.u.)	Pred. (p.u.)	|Error|	
			p.u.	%			p.u.	%
1	-20.16	-20.94	0.78	3.87	-19.73	-20.11	0.39	1.93
2	42.82	38.29	4.53	10.5	44.21	41.82	2.39	5.41
3	25.37	23.02	2.35	9.26	27.15	25.91	1.24	4.57
6	24.00	24.00	0.00	0.00	24.00	24.00	0.00	0.00
8	22.25	17.19	5.06	22.7	22.65	20.01	2.65	11.7
Avg. Error			2.54	9.29			1.33	4.71

Table 5: Comparison of Predicted Reactive Line Flow

Branch No	Method in [42]				Proposed method			
	Exact (p.u.)	Pred. (p.u.)	Error (p.u.)	|Error| (%)	Exact (p.u.)	Pred. (p.u.)	Error (p.u.)	|Error| (%)
1-2	-21.46	-20.95	0.51	2.38	-21.48	-21.19	0.29	1.35
1-5	1.30	0.02	1.28	98.46	1.75	1.08	0.67	38.29
2-3	3.30	3.35	0.05	1.52	3.29	3.33	0.03	1.22
2-4	-1.48	-3.58	2.10	141.89	-0.65	-1.75	1.09	169.23
2-5	-1.22	-2.80	1.58	129.51	-0.68	-1.50	0.82	120.59
3-4	3.77	1.66	2.11	55.97	5.53	4.42	1.11	20.07
4-5	8.42	10.16	1.74	20.67	8.70	9.76	1.06	12.18
4-7	-4.83	-7.87	3.04	62.94	-5.06	-6.27	1.21	23.91
4-9	3.22	0.54	2.68	83.23	3.16	2.08	1.07	34.18
6-11	5.39	5.37	0.02	0.37	5.39	5.33	0.06	1.11
6-12	3.26	3.26	0.00	0.00	3.26	3.20	0.06	1.84
6-13	7.85	7.86	0.01	0.13	7.85	7.71	0.14	1.78
7-8	-21.52	-16.75	4.77	22.17	-21.89	-19.42	2.48	11.28
7-9	10.26	4.26	6.00	58.48	10.38	7.50	2.88	27.75
9-10	4.90	1.62	3.28	66.94	4.91	3.44	1.47	29.94
9-14	3.88	1.74	2.14	55.15	3.89	3.05	0.84	21.59
10-11	-1.76	-4.41	2.65	150.57	-1.76	-2.64	0.87	50.00
12-13	1.59	1.62	0.03	1.89	1.59	1.53	0.06	3.77
13-14	3.53	3.79	0.26	7.37	3.53	3.68	0.16	4.25
Avg.			1.80	50.51			0.44	30.23

curve can be viewed to mimic the measurements from PMUs. Then, the proposed sensitivity model is combined with the N-0 voltages to estimate the N-1 voltages for a specific branch outage, and this can be applied to draw the N-1 PV curve once various load levels are considered.

Since this extensive test involves a large amount of data which are not suitable to be shown in tables, two types of N-1 PV curves, one *estimated* from the sensitivity and the N-0 voltages and the other *calculated* based on the actual N-1 CPF runs, are depicted and compared in figures.

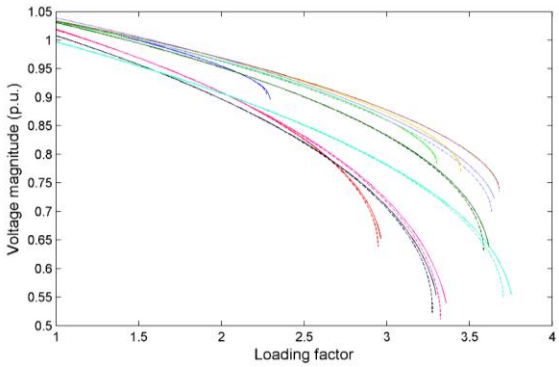

Figure 20. Voltage magnitude for N-1 contingencies of IEEE 14-bus system.

The test results for the IEEE 14-bus system are shown in Figure 20. The PV curves for Bus 14, which is the critical/weakest load bus, are chosen. The solid lines are the estimated values using the proposed sensitivity and N-0 voltages, while the dashed lines are the benchmark PV curves calculated using CPF under N-1 contingency. Different contingencies are distinguished using different colors. The X-axis represents the loading factor which can be multiplied with the base load level to obtain the actual load. In other words, a loading factor of 1.0 represents the base case. A total number of

17 line outages are considered but only the top 10 most severe outages are shown in Figure 20 due to the space limit. Based on the figure, the solid curves overlap with the dashed curves except at the very end close to the nose points. The errors at the end are larger than at other sections in the curves. This is reasonable because the increasing line flow tends to give less accurate results due to the linear estimation based on sensitivity, when the loading factor grows. Nevertheless, such error is still very small, generally less than 2% in terms of the power at the collapse point, which is clearly shown in Figure 20. Thus, the results are considered very accurate.

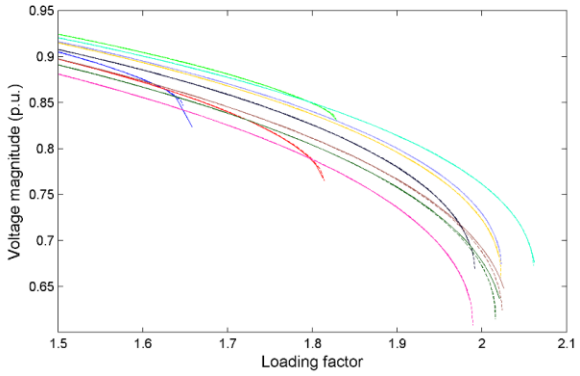

Figure 21. Voltage magnitude for N-1 contingencies of IEEE 39-bus system.

Figure 21 demonstrates the test results for the IEEE 39-bus system. The PV curves for Bus 7, which is the critical/weakest load bus, are chosen. Similarly, the solid lines are from the sensitivity-based estimation, while the dashed lines are from an actual CPF calculation under N-1 contingency. Due to the space limit, only the top 10 most severe outages are included. For better illustration, the PV curves start from 1.5 loading factor of the base case load. Note, the excluded portion of the curves between 1 and 1.5

times of the base load shows perfect overlap between the dashed and solid curves. As shown in Figure 21, the sensitivity also performs very well for the IEEE 39-bus system at all N-1 contingencies between the base case and the maximum load levels.

Test results for the IEEE 118-bus system are presented in Figure 22. The critical/weakest load bus is Bus 44, and there are a total number of 177 line outages examined. Again, only the top 10 most severe outages are presented in Figure 8 for easy illustration. Similarly, the solid lines are estimated results based on the proposed sensitivity, while the dashed lines are from the actual CPF calculation under N-1 contingency. Similar observations can be concluded that the sensitivity-based estimation gives very accurate N-1 PV curves.

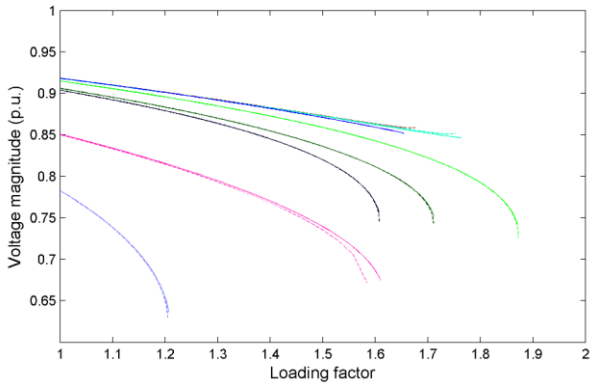

Figure 22. Voltage magnitude for N-1 contingencies of IEEE 118-bus system.

4.3.3 Test of the HBVSA

The previous subsection 4.3.2 demonstrates the validity of the proposed sensitivity at three systems under N-1 contingencies with a broad range of load levels, which is between the base case load level and the maximum load level right at the nose

points. In this subsection, the model-based sensitivity will be combined with the measurement-based approach to evaluate the system's voltage stability margin under various N-1 contingencies. Here, the voltage stability index (VSI) introduced in equation (4-20) is employed to estimate the N-1 stability margin, which is defined as the distance in % between the base case and the VSI-based nose point. Note, under measurement based techniques, the VSI-based noise point is defined using the VSI value. That is, VSI is greater than 1.0 if the system operates at the upper portion of the PV curve for a specific N-1 contingency; while the VSI decreases to 1.0 or below if the system is considered at the nose point and therefore unsecure for that contingency.

For the IEEE 14-bus system, the stability margins from HBVSA (using VSI-based nose point criterion) and actual N-1 CPF are presented in Figure 23. Similarly, the results of the IEEE 39-bus system are shown in Figure 24, and the results of the 30 most severe contingencies (due to space limit) for the IEEE 118-bus system are shown in Figure 25. According to these three figures, the stability margins calculated by HBVSA based on N-0 voltages and the proposed sensitivity calculation are close to the actual margins from N-1 CPF. The average errors in estimating the system stability margin for the three cases for all outages (not limited to 30 most severe contingencies for the 118-bus system) are presented in Table 6. It is shown that the HBVSA is able to estimate the stability margin very accurately.

Table 6: Average Errors of Stability Margins

	IEEE 14-bus system	*IEEE 39-bus system*	*IEEE 118-bus system*
Average error	0.63%	0.23%	0.21%

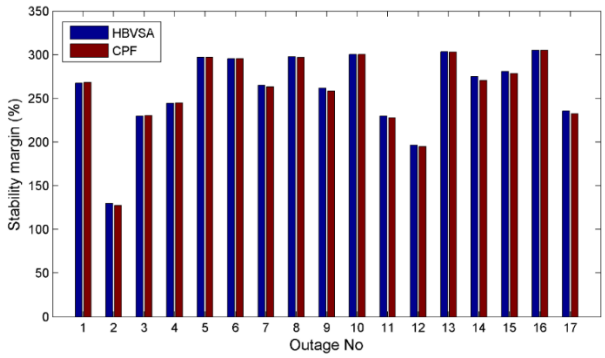

Figure 23. Stability margin for line outages of the IEEE 14-bus system.

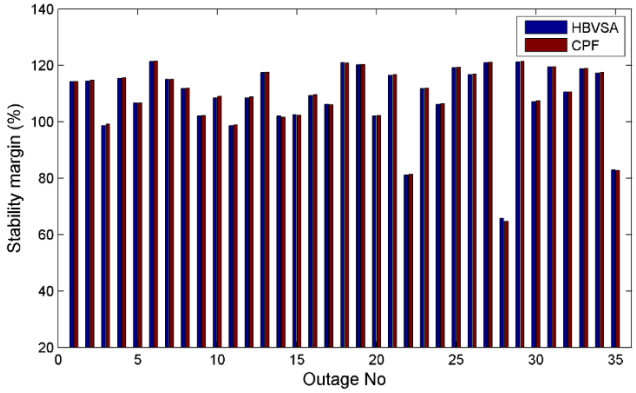

Figure 24. Stability margin for line outages of the IEEE 39-bus system.

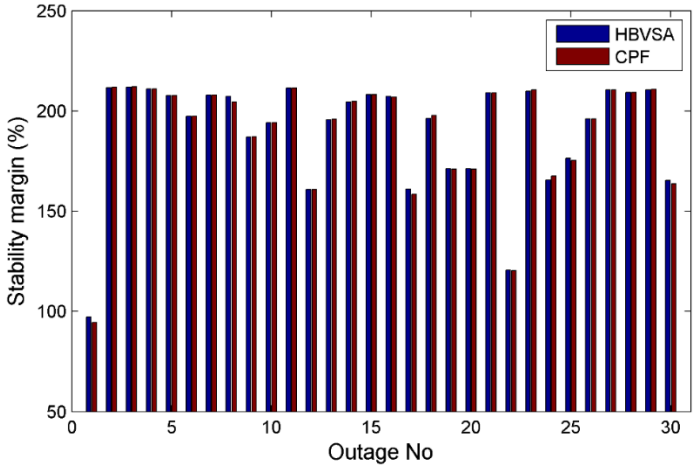

Figure 25. Stability margin for line outages of the IEEE 118-bus system.

In order to better illustrate HBVSA, a load increasing simulation scenario is created. In this scenario, the load of the whole system increases continuously with small randomly embedded noises for more than 1000 seconds. The voltage magnitude of Bus 44 for this scenario is shown in Figure 26 (a) where the voltage decreases as the load increases. With PMUs installed, the voltage for N-0 can be monitored by the system operator in the control room. With the proposed HBVSA, the system operator will be able to keep track of the voltages under N-1 as shown in Figure 26 (b) as well as the VSI for those contingencies shown in Figure 26 (c) in real time. Once again, only the top 30 most severe contingencies are shown due to space limit and for easy illustration. By combing the model-based sensitivity with the measurement-based VSA, the HBVSA using N-1 VSI (as shown in Figure 26(c)) provides clear information about how far the system is away from voltages instability under N-1 contingencies. Since the N-1 VSI is obtained in real time based on measured N-0 voltages and the model-based sensitivity matrices which can be calculated in real time because it is only related to topology (obtained offline) and the present operating point (from measurement). Thus, this will significantly increase the situation awareness by identifying the most critical contingency and monitoring the security margin.

Another observation is that according to Figure 26 (c), at the end of the simulation the VSI of the blue curve (line 8-5 outage) reaches 1.0, which means the system reaches an insecure state. However, this contingency is not the most severe one in terms of voltage drops, as shown in Figure 26(b). Thus, Figure 26(b) and (c) clearly verify that the most critical contingency in terms of voltage stability may not be the contingency causing

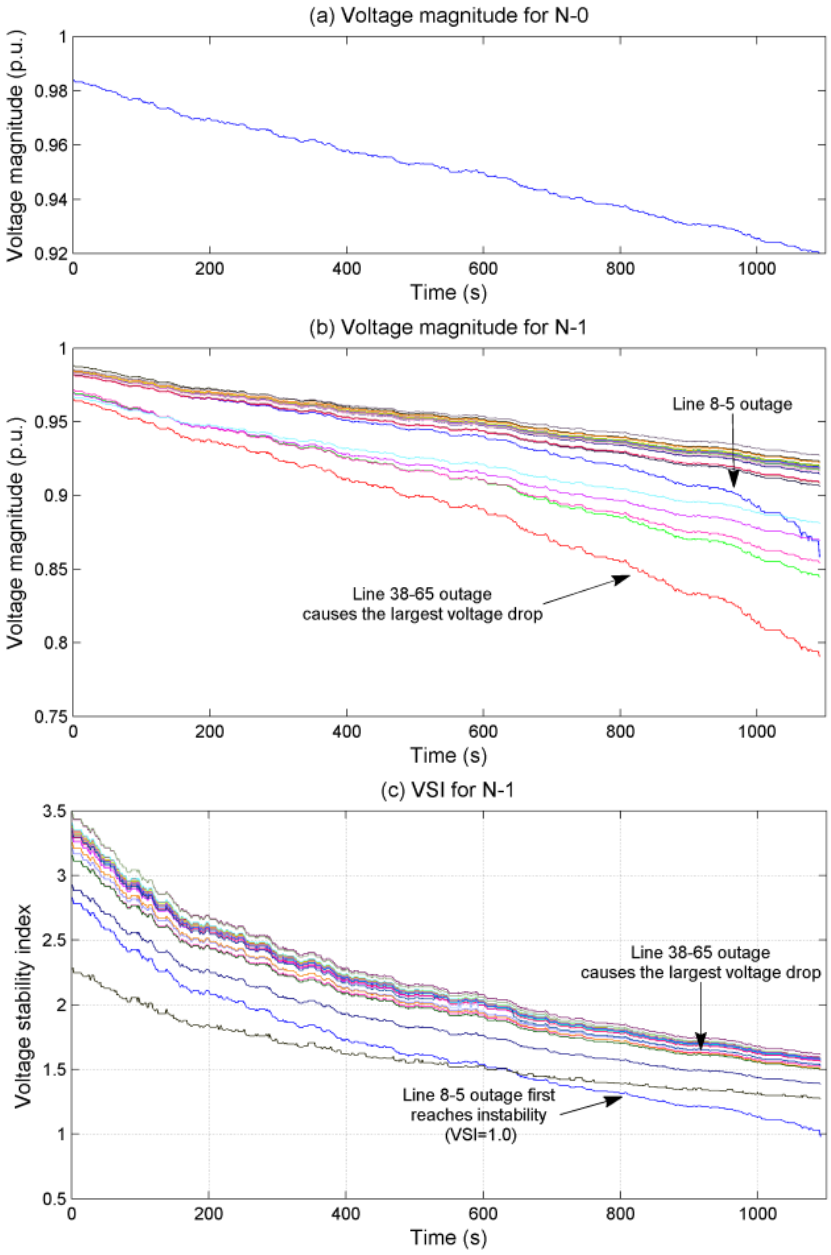

Figure 26. Illustration of the HBVSA under N-1 contingency.

the largest voltage drop.

4.4 Conclusion

In this chapter, a hybrid voltage stability assessment (VSA) method is proposed for N-1 contingency. With the proposed model-based contingency sensitivity and the measurement-based VSA technique, the hybrid VSA method solves the challenge of VSA under contingency cases. This broadens the application of PMUs in actual practices.

This chapter proposes a model-based sensitivity calculation method for estimating the post-contingency system status. The transformation in deriving the sensitivity is mathematically proven in the chapter. Test results on the IEEE 14-bus system show that the proposed method considerably reduces the estimation errors, especially when reactive power limits are violated. This is the advantage of the proposed method over the methods in the literature.

Case studies of the proposed sensitivity on IEEE 14, 39, and 118-bus systems for all line outages demonstrate that it is suitable and accurate for estimating post-contingency status for VSA applications. The proposed HBVSA method, which is based on the estimated post-contingency system status, shows good accuracy in estimating the stability margin for the N-1 contingency on all the three test systems. Finally, a loadincreasing scenario simulated on the IEEE 118 system illustrates the ability that the HBVSA can assist the system operators with monitoring the stability margin for N-1 contingencies.

Besides the accuracy, the proposed method has several advantages from the computational aspect. First, the developed sensitivity model can predict the post-contingency with little computational resources compared with traditional CPF. Second,

the procedure in calculating the VSI is computationally efficient. Third, the proposed scheme as shown in Figure 18 is suitable for parallel implementation and thus has a promising potential in online applications. This can be a future work of this research.

CHAPTER 5

MEASUREMENT-BASED WIDE-AREA LOADING MARGIN SENSITIVITY AND ITS APPLICATION IN VOLTAGE STABILITY CONTROL

Sensitivity analyses have been widely studied in the realm of voltage stability assessment (VSA) and control. Existing model-based sensitivities for VSA require full detailed system models as well as non-trivial amount of computation; therefore, they are not ideal for online applications. Based on the recently developed single-port circuit model, this work proposes measurement-based wide-area loading margin sensitivity (WALMS) that is suitable for real-time deployment. With the measurements from wide-area measurement systems, the WALMS model can be used to derive the analytical expression of the sensitivity of loading margin (LM) versus power injection and generator terminal voltage. Consequently, the WALMS is highly efficient to be calculated if compared with its model-based counterparts. In addition, a multi-step control strategy for voltage stability integrating the WALMS is considered with the purpose to demonstrate the applicability of the proposed sensitivity. Case study on the IEEE 39-bus system verifies the WALMS and validates the multi-step control strategy. Further, the proposed WALMS is extensively tested on the IEEE 14, 57, and 300-bus systems. Evidently, the measurement-based WALMS has great potential to be integrated to online VSA and control applications.

5.1 Voltage Stability Assessment Using Coupled Single-Port Circuit Concept

This work is based on the coupled single-port circuit concept proposed in [34]. A power system can be modeled as a multi-port network and can be described by [34]

$$\begin{bmatrix} -\boldsymbol{I}_L \\ 0 \\ \boldsymbol{I}_G \end{bmatrix} = [\boldsymbol{Y}] \begin{bmatrix} \boldsymbol{V}_L \\ \boldsymbol{V}_T \\ \boldsymbol{V}_G \end{bmatrix} = \begin{bmatrix} \boldsymbol{Y}_{LL} & \boldsymbol{Y}_{LT} & \boldsymbol{Y}_{LG} \\ \boldsymbol{Y}_{TL} & \boldsymbol{Y}_{TT} & \boldsymbol{Y}_{TG} \\ \boldsymbol{Y}_{GL} & \boldsymbol{Y}_{GT} & \boldsymbol{Y}_{GG} \end{bmatrix} \begin{bmatrix} \boldsymbol{V}_L \\ \boldsymbol{V}_T \\ \boldsymbol{V}_G \end{bmatrix} \tag{5-1}$$

where the $\boldsymbol{Y}$ matrix is the system admittance matrix, $\boldsymbol{V}$ and $\boldsymbol{I}$ are vectors of voltage and current phasors, and the subscripts *L*, *T*, and *G* represent sets of the load bus, tie bus, and generator bus, respectively.

Eliminating the voltage vectors of the tie buses, we have [34]

$$\begin{aligned} \boldsymbol{V}_L &= \boldsymbol{K}\boldsymbol{V}_G - \boldsymbol{Z}_{LL}\boldsymbol{I}_L \\ \boldsymbol{Z}_{LL} &= (\boldsymbol{Y}_{LL} - \boldsymbol{Y}_{LT}\boldsymbol{Y}_{TT}^{-1}\boldsymbol{Y}_{TL})^{-1} \\ \boldsymbol{K} &= \boldsymbol{Z}_{LL}(\boldsymbol{Y}_{LT}\boldsymbol{Y}_{TT}^{-1}\boldsymbol{Y}_{TG} - \boldsymbol{Y}_{LG}) \end{aligned} \tag{5-2}$$

For load bus i, we have [34],

$$\boldsymbol{V}_i = \boldsymbol{E}_{eq,i} - (\boldsymbol{Z}_{ii} + \boldsymbol{Z}_{cp,i})\boldsymbol{I}_i = \boldsymbol{E}_{eq,i} - \boldsymbol{Z}_{eq,i} \cdot \boldsymbol{I}_i \tag{5-3}$$

$$\boldsymbol{E}_{eq,i} = [\boldsymbol{K}\boldsymbol{V}_G]_i = \sum_{g \in G} \boldsymbol{K}_{ig}\boldsymbol{V}_g \tag{5-4}$$

$$\boldsymbol{Z}_{cp,i} = \sum_{j \in L,\, j \neq i} \boldsymbol{Z}_{ij}\frac{\boldsymbol{I}_j}{\boldsymbol{I}_i} = \sum_{j \in L,\, j \neq i} \boldsymbol{Z}_{ij}\frac{\boldsymbol{S}_j^* \boldsymbol{V}_i^*}{\boldsymbol{S}_i^* \boldsymbol{V}_j^*} \tag{5-5}$$

where $\boldsymbol{Z}_{ii}$ is the diagonal element of $\boldsymbol{Z}_{LL}$ for load bus *i*, and $\boldsymbol{Z}_{ij}$ is the element in $\boldsymbol{Z}_{LL}$, the coupling impedance corresponding to load bus *i* and to load bus *j*; $\boldsymbol{Z}_{cp,i}$ is the coupled impedance for load bus *i*; $\boldsymbol{K}_{ig}$ is the element in $\boldsymbol{K}$ matrix corresponding to load bus *i* and generator bus *g*.

By modeling the coupling effect of other loads into $\boldsymbol{Z}_{cp,i}$, the TE can be found through (5-3) and (5-5) and is depicted in Figure 27. The Thevenin voltage $\boldsymbol{E}_{eq,i}$ is determined by the generator terminal voltages through matrix $\boldsymbol{K}$. The Thevenin impedance $\boldsymbol{Z}_{eq,i}$ is determined by the diagonal element of $\boldsymbol{Z}_{LL}$ and the coupling of other loads through corresponding elements in $\boldsymbol{Z}_{LL}$.

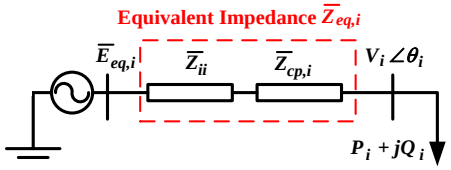

Figure 27. Coupled single-port circuit

Assuming that the measurements of voltage phasors at all generator terminals and voltage and current phasors at load bus i are available from PMUs and the system admittance matrix is also available. The TE as seen from bus i can be calculated using (3) [34].

For the pattern of proportional load increasing, the LM of the load bus i can be calculated as below:

$$\begin{aligned}\lambda_i &= f\left(E_{eq,i}, R_{eq,i}, X_{eq,i}, P_i, Q_i\right) \\ &= \frac{E_{eq,i}{}^2\left(\sqrt{\left(R_{eq,i}^2 + X_{eq,i}^2\right)\left(P_i^2 + Q_i^2\right)} - R_{eq,i}P_i - X_{eq,i}Q_i\right)}{2\left(X_{eq,i}P_i - R_{eq,i}Q_i\right)^2} - 1\end{aligned} \tag{6}$$

where $R_{eq,i}$ and $X_{eq,i}$ are the real and imaginary parts of $\boldsymbol{Z}_{eq,i}$, respectively, and are defined in (5-7) and (5-8); P_i and Q_i are the real and reactive power consumptions at bus i; and $E_{eq,i}$ is the magnitude of $\boldsymbol{E}_{eqi}$.

$$R_{eq,i} = R_{ii} + \sum_{\substack{k\in L \\ k\neq i}} \frac{V_i}{V_k S_i^2} \begin{pmatrix} \left(R_{ik}\cos\theta_{ki} - X_{ik}\sin\theta_{ki}\right)\left(P_i P_k + Q_i Q_k\right) \\ -\left(R_{ik}\sin\theta_{ki} + X_{ik}\cos\theta_{ki}\right)\left(Q_i P_k - P_i Q_k\right) \end{pmatrix} \tag{5-7}$$

$$X_{eq,i} = X_{ii} + \sum_{\substack{k\in L \\ k\neq i}} \frac{V_i}{V_k S_i^2} \begin{pmatrix} \left(R_{ik}\sin\theta_{ki} + X_{ik}\cos\theta_{ki}\right)\left(P_i P_k + Q_i Q_k\right) \\ +\left(R_{ik}\cos\theta_{ki} - X_{ik}\sin\theta_{ki}\right)\left(Q_i P_k - P_i Q_k\right) \end{pmatrix} \tag{5-8}$$

where $S_i^2 = P_i^2+Q_i^2$, $R_{ii}+\mathrm{j}X_{ii} = \boldsymbol{Z}_{ii}$, $R_{ik} + \mathrm{j}X_{ik} = \boldsymbol{Z}_{ik}$, and θ_{ki} is the angle between $\boldsymbol{V}_k$ and $\boldsymbol{V}_i$.

Note that the same load increasing pattern as [34] is assumed in this work. If a non-proportional pattern is involved, modification can be applied, as outlined in [36].

The LM of the system is determined by the smallest margin of all load buses (i.e., the critical bus):

$$\lambda_{sys} = \min\left\{\lambda_1, \lambda_2, \cdots, \lambda_n\right\} \tag{5-9}$$

5.2 Wide-Area Loading Margin Sensitivity

Usually, a power system should be operated with a LM no less than a predefined threshold. If the LM is below the predefined threshold as the operating condition shifts or a contingency occurs, a series of actions should be taken to increase the LM for voltage stability's viewpoint. Reactive power compensation, terminal voltage adjustment, and load shedding are among the most commonly involved actions. Therefore, the LMS to the reactive power injection, real power injection, and the terminal voltage of generator buses, are derived from the following.

5.2.1 LMS w.r.t. Reactive Power Injection

According to (5-6), the LM is a function of TE parameters ($E_{eq,j}$, $R_{eq,i}$, $X_{eq,i}$) as well as the nodal consumptions (P_i, Q_i). Furthermore, according to (5-7) and (5-8), $R_{eq,i}$

and $X_{eq,i}$ are dependent on (P_i, Q_i, V_i) as well as (P_j, Q_j, V_j) for $j \in L$ and $j \neq i$.

Based on (5-6) to (5-8), the LMS of bus i to the reactive load of bus j (j not equal to i) will have a different formulation than the LMS of bus i to the reactive load of bus i. To better differentiate the two formations, the former is referred to as cross-sensitivity and the latter is referred as self-sensitivity.

Cross-sensitivity:

The cross-sensitivity of LM of bus i to the reactive load of bus j can be derived as in (5-10):

$$\frac{\partial \lambda_i}{\partial Q_j} = \frac{\partial f}{\partial R_{eq,i}} \frac{\partial R_{eq,i}}{\partial Q_j} + \frac{\partial f}{\partial X_{eq,i}} \frac{\partial X_{eq,i}}{\partial Q_j} \tag{5-10}$$

where

$$\frac{\partial f}{\partial R_{eq,i}} = \frac{E_{eq,i}{}^2 \left(R_{eq,i} S_i / Z_{eq,i} - P_i \right)}{2\left(X_{eq,i} P_i - R_{eq,i} Q_i \right)^2} + \frac{2Q_i \left(\lambda_i + 1 \right)}{\left(X_{eq,i} P_i - R_{eq,i} Q_i \right)} \tag{5-11}$$

$$\frac{\partial f}{\partial X_{eq,i}} = \frac{E_{eq,i}{}^2 \left(X_{eq,i} S_i / Z_{eq,i} - Q_i \right)}{2\left(X_{eq,i} P_i - R_{eq,i} Q_i \right)^2} - \frac{2P_i \left(\lambda_i + 1 \right)}{\left(X_{eq,i} P_i - R_{eq,i} Q_i \right)} \tag{5-12}$$

$$\frac{\partial R_{eq,i}}{\partial Q_j} = \frac{V_i \left(\left(R_{ij} Q_i + X_{ij} P_i \right) \cos \theta_{ji} - \left(X_{ij} Q_i - R_{ij} P_i \right) \sin \theta_{ji} \right)}{V_j S_i^2} \tag{5-13}$$

$$\frac{\partial X_{eq,i}}{\partial Q_j} = \frac{V_i \left(\left(R_{ij} Q_i + X_{ij} P_i \right) \sin \theta_{ji} + \left(X_{ij} Q_i - R_{ij} P_i \right) \cos \theta_{ji} \right)}{V_j S_i^2} \tag{5-14}$$

In (5-13) and (5-14), the impact of Q_j to voltage of V_j and V_i is not considered. From the viewpoint of power flow equations, it is true that the change of reactive injections will lead to the change of voltages at load buses. However, such impact to V_j/V_i

as a whole is trivial compared to the impact of Q_j to the items in the parentheses in (5-7) and (5-8).

Self-sensitivity:

The self-sensitivity of LM of bus i can be derived as in (5-15) where the derivatives of f to $R_{eq,i}$ and $X_{eq,i}$ are the same as (5-11) and (5-12).

$$\frac{\partial \lambda_i}{\partial Q_i} = \frac{\partial f}{\partial R_{eq,i}} \frac{\partial R_{eq,i}}{\partial Q_i} + \frac{\partial f}{\partial X_{eq,i}} \frac{\partial X_{eq,i}}{\partial Q_i} + \frac{\partial f}{\partial Q_i} \tag{5-15}$$

According to (5-6)

$$\frac{\partial f}{\partial Q_i} = \frac{E_{eq,i}{}^2 \left(Q_i Z_{eq,i} / S_i - X_i \right)}{2\left(X_{eq,i} P_i - R_{eq,i} Q_i \right)^2} + \frac{2R_i \left(\lambda_i + 1 \right)}{X_{eq,i} P_i - R_{eq,i} Q_i} \tag{5-16}$$

For the derivative of $R_{eq,i}$, $X_{eq,i}$ to Q_i, the change of V_i caused by ΔQ_i will be included in every summation item in (5-7) and (5-8), also the impact of ΔQ_i to V_i will be significantly higher compared with ΔQ_j to V_i. Therefore, V_i is considered as a function of Q_i. From the two-bus circuit shown in Figure 27, V_i, P_i, and Q_i should satisfy (5-17) [36].

$$V_i^4 + \left(2P_i R_{eq,i} + 2Q_i X_{eq,i} - E_{eq,i}^2 \right) V_i^2 + \left(R_{eq,i}^2 + X_{eq,i}^2 \right) \left(P_i^2 + Q_i^2 \right) = 0 \tag{5-17}$$

Take the derivative w.r.t. Q_i on both sides of (5-17):

$$A1 \partial V_i / \partial Q_i + A2 \partial R_{eq,i} / \partial Q_i + A3 \partial Q_{eq,i} / \partial Q_i + A4 = 0 \tag{5-18}$$

where

$$\begin{aligned} &A1 = 2V_i^3 + V_i \left(2P_i R_{eq,i} + 2Q_i X_{eq,i} - E_{eq,i}^2 \right) \\ &A2 = P_i V_i^2 + R_{eq,i} S_i^2, A3 = Q_i V_i^2 + X_{eq,i} S_i^2, A4 = X_{eq,i} V_i^2 + Q_i Z_{eq,i}^2 \end{aligned} \tag{5-19}$$

Take the derivative w.r.t. Q_i on both sides of (5-7) and (5-8):

$$\frac{\partial R_{eq,i}}{\partial Q_i} = \frac{R_{cp,i}}{V_i}\frac{\partial V_i}{\partial Q_i} + B1, \qquad \frac{\partial X_{eq,i}}{\partial Q_i} = \frac{X_{cp,i}}{V_i}\frac{\partial V_i}{\partial Q_i} + B2 \tag{5-20}$$

where

$$B1 = \frac{V_i}{S_i^2}\sum_{\substack{j\in L \\ j\neq i}} \frac{\left(R_{ij}Q_j - X_{ij}P_j\right)\cos\theta_{ji} - \left(R_{ij}P_j + X_{ij}Q_j\right)\sin\theta_{ji}}{V_j} - \frac{2Q_iR_{cp,i}}{S_i^2} \tag{5-21}$$

$$B2 = \frac{V_i}{S_i^2}\sum_{\substack{j\in L \\ j\neq i}} \frac{\left(R_{ij}P_j + X_{ij}Q_j\right)\cos\theta_{ji} + \left(R_{ij}Q_j - X_{ij}P_j\right)\sin\theta_{ji}}{V_j} - \frac{2Q_iX_{cp,i}}{S_i^2} \tag{5-22}$$

Substitute $\partial R_{eq,i}/\partial Q_i$ and $\partial X_{eq,i}/\partial Q_i$ in (5-18) with (5-20), we can easily calculate $\partial V_i/\partial Q_i$. Then, $\partial R_{eq,i}/\partial Q_i$ and $\partial X_{eq,i}/\partial Q_i$ can be solved based on (5-20). Finally, the proposed self-sensitivity shown in (5-15) can be calculated.

The calculation of self-sensitivity is more complex than cross-sensitivity because of the following reasons: 1) the third component in (5-15); 2) the summation in calculating $B1$ and $B2$ in (5-21) and (5-22); and 3) the inclusion of $\partial V_i/\partial Q_i$. Such extra efforts are well-justified in the sense that self-sensitivity is most likely the dominant sensitivity.

The sensitivity w.r.t. reactive power injection proposed here has been improved based on [18] in that 1) λ (i.e. the LM) is expressed without the power factor, which is related to P_i and Q_i; and 2) the self-sensitivity includes $\partial V_i/\partial Q_i$ in order to improve the accuracy.

Despite the above changes, the computational effort remains in the same scale as [18]. The computation of $\partial V_i/\partial Q_i$ is based on the two-bus circuit model and do not

involve the Jacobian power flow system. Furthermore, no additional information or measurement is needed in addition to the measurement-based VSA of [34].

5.2.2 LMS w.r.t. Real Power Injection

Similarly, the cross-sensitivity (the sensitivity of the LM of bus *i* to the real power load of bus *j* (*j* not equal to *i*)) and the self-sensitivity (sensitivity of LM of bus *i* to the real power load of bus *i*) are derived next.

Note that the LMSs in Section 5.2.2 and 5.2.3 are both newly developed and are never presented in [18] or other works.

Cross-sensitivity:

The cross-sensitivity of LM of bus *i* to the real power load of bus *j* ($j \neq i$) can be derived from (5-6):

$$\frac{\partial \lambda_i}{\partial P_j} = \frac{\partial f}{\partial R_{eq,i}} \frac{\partial R_{eq,i}}{\partial P_j} + \frac{\partial f}{\partial X_{eq,i}} \frac{\partial X_{eq,i}}{\partial P_j} \tag{5-23}$$

where

$$\frac{\partial R_{eq,i}}{\partial P_j} = \frac{V_i \left(\left(R_{ij} P_i - X_{ij} Q_i \right) \cos \theta_{ji} - \left(X_{ij} P_i + R_{ij} Q_i \right) \sin \theta_{ji} \right)}{V_j S_i^2} \tag{5-24}$$

$$\frac{\partial X_{eq,i}}{\partial P_j} = \frac{V_i \left(\left(R_{ij} P_i - X_{ij} Q_i \right) \sin \theta_{ji} + \left(X_{ij} P_i + R_{ij} Q_i \right) \cos \theta_{ji} \right)}{V_j S_i^2} \tag{5-25}$$

$\partial f / \partial R_{eq,i}$ and $\partial f / \partial X_{eq,i}$ are the same as in (5-11) and (5-12).

Self-sensitivity:

Based on (5-6), the self-sensitivity of LM of bus *i* to the real power load of bus *i* can be expressed in (5-26) as:

$$\frac{\partial \lambda_i}{\partial P_i} = \frac{\partial f}{\partial R_{eq,i}} \frac{\partial R_{eq,i}}{\partial P_i} + \frac{\partial f}{\partial X_{eq,i}} \frac{\partial X_{eq,i}}{\partial P_i} + \frac{\partial f}{\partial P_i} \tag{5-26}$$

According to (5-6), $\partial f/\partial P_i$ can be derived in (5-27) as:

$$\frac{\partial f}{\partial P_i} = \frac{E_{eq,i}{}^2 \left(P_i Z_{eq,i}/S_i - R_i \right)}{2\left(X_{eq,i} P_i - R_{eq,i} Q_i \right)^2} - \frac{2X_i \left(\lambda_i + 1 \right)}{X_{eq,i} P_i - R_{eq,i} Q_i} \tag{5-27}$$

Equation (5-28) can be achieved by taking the derivative w.r.t. P_i on both sides of (5-17).

$$A1 \partial V_i / \partial P_i + A2 \partial R_{eq,i} / \partial P_i + A3 \partial Q_{eq,i} / \partial P_i + A5 = 0 \tag{5-28}$$

where $A1$, $A2$, and $A3$ have the same forms as in (5-19) and

$$A5 = R_{eq,i} V_i^2 + P_i Z_{eq,i}^2 \tag{5-29}$$

Take the derivative, w.r.t. P_i, on both sides of (5-7) and (5-8):

$$\frac{\partial R_{eq,i}}{\partial P_i} = \frac{R_{cp,i}}{V_i} \frac{\partial V_i}{\partial P_i} + C1, \qquad \frac{\partial X_{eq,i}}{\partial P_i} = \frac{X_{cp,i}}{V_i} \frac{\partial V_i}{\partial P_i} + C2 \tag{5-30}$$

where

$$C1 = \frac{V_i}{S_i^2} \sum_{\substack{j \in L \\ j \neq i}} \frac{\left(R_{ij} P_j + X_{ij} Q_j \right) \cos \theta_{ji} + \left(R_{ij} Q_j - X_{ij} P_j \right) \sin \theta_{ji}}{V_j} - \frac{2 P_i R_{cp,i}}{S_i^2} \tag{5-31}$$

$$C2 = \frac{V_i}{S_i^2} \sum_{\substack{j \in L \\ j \neq i}} \frac{\left(X_{ij} P_j - R_{ij} Q_j \right) \cos \theta_{ji} + \left(R_{ij} P_j + X_{ij} Q_j \right) \sin \theta_{ji}}{V_j} - \frac{2 P_i X_{cp,i}}{S_i^2} \tag{5-32}$$

If we substitute $\partial R_{eq,i}/\partial P_i$ and $\partial X_{eq,i}/\partial P_i$ in (5-28) with (5-30), $\partial V_i/\partial P_i$ can be directly computed. Then $\partial R_{eq,i}/\partial P_i$ and $\partial X_{eq,i}/\partial P_i$ can be solved according to (5-30). Finally, the proposed self-sensitivity shown in (5-26) can be calculated.

5.2.3 LMS w.r.t. Terminal Voltage of Generator Bus

According to (5-4), $\boldsymbol{E}_{eq,i}$, the Thevenin voltage of load bus i, is determined by the terminal voltages of generator buses through $\boldsymbol{K}$ matrix. However, the other elements in (5-6) are not dependent on V_g, $g \in G$. Therefore, the sensitivity of LMs of load bus i to the generator terminal voltage at bus g, V_g ($g \in G$), can be derived as:

$$\frac{\partial \lambda_i}{\partial V_g} = \frac{\partial f}{\partial E_{eq,i}^2} \cdot \frac{\partial E_{eq,i}^2}{\partial V_g} = \frac{\lambda_i + 1}{{E_{eq,i}}^2} \cdot \frac{\partial E_{eq,i}^2}{\partial V_g} \tag{5-33}$$

Let $E_{re,i}$ and $E_{im,i}$ denote the real and imaginary part of $\boldsymbol{E}_{eq,i}$, and $K_{re,ig}$ and $K_{im,ig}$ denote the real and imaginary part of $\boldsymbol{K}_{ig}$. Based on the $\boldsymbol{E}_{eq,i}$ expression in (5-4), $E^2_{eq,i}$ can be expressed as:

$$\begin{aligned} E_{eq,i}^2 &= E_{re,i}^2 + E_{im,i}^2 \\ E_{re,i} &= \sum_{g \in G} V_g \left(K_{re,ig} \cos\delta_g - K_{im,ig} \sin\delta_g \right) \\ E_{im,i} &= \sum_{g \in G} V_g \left(K_{re,ig} \sin\delta_g + K_{im,ig} \cos\delta_g \right) \end{aligned} \tag{5-34}$$

where V_g and δ_g are the magnitude and angle of terminal voltage of generator bus g, respectively; G is the generator bus set.

With (5-34), $\partial E^2_{eq,i}/\partial V_g$ can be derived as follows:

$$\begin{aligned} \partial E_{eq,i}^2 \big/ \partial V_g = {} & 2E_{re,i} \left(K_{re,ig} \cos\delta_g - K_{im,ig} \sin\delta_g \right) \\ & + 2E_{im,i} \left(K_{re,ig} \sin\delta_g + K_{im,ig} \cos\delta_g \right) \end{aligned} \tag{5-35}$$

If (5-33) and (5-35) are combined, the LMS w.r.t. generator terminal voltage can be solved.

5.3 Voltage Stability Control Based on WALMS

The WALMS derived in Section 5.2 are based on the two-bus coupled single-port circuit shown in Figure 27, and can be calculated with minimum complexity from the wide-area measurements. Thus, it is more suitable to be deployed online compared with its model-based counterparts.

If implemented online, the proposed WALMS will provide valuable information for system operators to take proper control actions to maintain sufficient voltage stability margins. The measurement-based WALMS can also act as a complement of the model-based sensitivity and they can validate one another. In general, the proposed WALMS is able to function similarly as the model-based LMSs in various applications.

It is not our priority to explore the potential of the WALMS in various applications. However, here we propose a simple yet effective VSA control strategy based on the WALMS in order to better demonstrate and verify the proposed WALMS.

A common practice regarding VSA is to operate the system with a predefined LM (say, 10% for normal status and 5% for post-contingency status) to ensure that the system is free from voltage instability [59]. Such a predefined margin is usually calculated offline, in advance, with the predicted load profile and selected contingencies. If the system fails to meet such margin in real time, system operators must take proper control actions to increase the LM.

Usually, there are sets of available control actions that a system operator can take. Choosing how to select from various options is essentially an optimization problem. If nonlinearity of the power system is fully modeled, such problems usually require

significant amounts of computational resources to solve, especially for large systems.

Based on the WALMS, a straightforward multi-step control strategy for voltage stability is proposed. The proposed control strategy takes advantage of the simplicity of WALMS and is able to efficiently make the decision of which control action to take and what amount to apply in a multi-step process.

For a power system, let $\boldsymbol{\lambda}^{(0)}$ and $\boldsymbol{\lambda}^{(k)}$ be the vector of LMs at Step 0 (i.e., the initial system status) and Step k, respectively. Let $\boldsymbol{u}^{(k)}$ be the vector of control actions at Step k. With the three types of WALMS derived in Section 5.2, $\boldsymbol{u}^{(k)}$ should consist of [$\Delta\boldsymbol{P}_L^{(k)}$, $\Delta\boldsymbol{Q}_L^{(k)}$, $\Delta\boldsymbol{V}_G^{(k)}$], or a subset of it that contains the candidate locations only.

The proposed control strategy is able to deal with controls of three categories: 1) reactive power compensation, 2) generator terminal voltage increment, and 3) load shedding. Regarding the three categories, the proposed control strategy takes the control actions in the order of 1), 2), and then 3). At decision Step k, the algorithm first searches the available category with the highest order and then within that category the control strategy takes the available control action with the largest sensitivity (absolute value) at that step and forms control vector $\boldsymbol{u}^{(k)}$ (discussed in the following). Then, the LM after Step k is updated, according to (5-36).

$$\boldsymbol{\lambda}^{(k)} = \boldsymbol{\lambda}^{(k-1)} + \left[\partial\boldsymbol{\lambda} / \partial\boldsymbol{u}\right] \cdot \boldsymbol{u}^{(k)} \tag{5-36}$$

If the smallest value in $\boldsymbol{\lambda}^{(k)}$ is larger than the desired LM, then the multi-step decision process is terminated, and the control decisions of all the steps are applied; otherwise, the decision process goes to Step k+1. The proposed control strategy is illustrated in Figure 28 and described in detail in the remainder of this section.

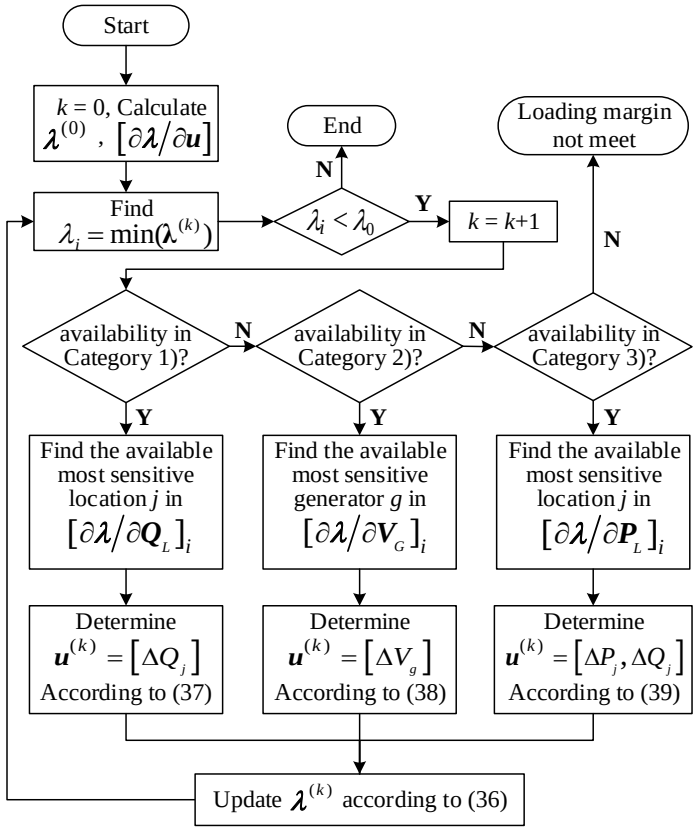

Figure 28. Flowchart of the proposed control strategy.

5.3.1 Category 1) Reactive Power Compensation

Reactive power compensation provided near the weakest load buses (i.e., load buses with the smallest LM) are among the most effective control actions [53]; therefore, this category is assigned the highest priority, always considered first. Within this category, the candidate location with the sensitivity of the largest absolute value is considered first because the same amount of compensation will increase the LM most among all candidate locations.

Let λ_0 be the desired LM, bus i be the bus with the smallest LM. If $\lambda_i < \lambda_0$. The amount of reactive power compensation to be applied at bus j, the candidate location with the largest sensitivity, can be determined by

$$\Delta Q_j = \max\left(\Delta Q_{j,\text{req}} = \frac{\lambda_0 - \lambda_i}{\partial \lambda_i / \partial Q_j}, \Delta Q_{j,\text{lim}} \right) \tag{5-37}$$

where $\Delta Q_{j,\text{lim}}$ is the capacity of the reactive compensation at bus j and is a negative number, meaning opposite direction of load increasing. $\Delta Q_{j,\text{req}}$ (also negative) is the amount of compensation required to meet the LM λ_0.

According to (5-37), when the compensation at bus j alone is capable of lifting the LM to meet λ_0 (i.e., $\Delta Q_{j,\text{req}} > \Delta Q_{j,\text{lim}}$) the amount to be compensated is $\Delta Q_{j,\text{req}}$. Otherwise, if $\Delta Q_{j,\text{req}} < \Delta Q_{j,\text{lim}}$, after $\Delta Q_{j,\text{lim}}$ is applied, the LM still fails to meet λ_0. For the latter case, the $\Delta Q_{j,\text{lim}}$ is applied. For Category 1, $\boldsymbol{u}^{(k)} = [\Delta Q_j]$ is formed and LM vector $\boldsymbol{\lambda}$ is updated based on (5-36).

If the updated $\boldsymbol{\lambda}$ does not meet λ_0, further actions need to be taken. If there is not any candidate bus with reactive compensation capability, the control algorithm will

search control actions in Category 2.

5.3.2 Category 2) Generator Terminal Voltage Increment

Increasing the terminal voltage at generator buses is equivalent to apply reactive compensation at the corresponding buses. The terminal voltage is chosen here to quantify this control category; for a generator bus, the terminal voltage is regulated and the amount of reactive compensation is determined by the setting of the terminal voltage.

This category is considered after Category 1 because generator buses are usually located with some distance to the weakest load buses and as a result, the compensation of reactive power at the generator buses is less effective compared to the compensation at nearby load buses due to the high percentage of reactive losses along the transfer path.

Similarly, within this category, the candidate generator bus with the largest sensitivity (e.g., bus g) is first considered. The increment is determined by (5-38).

$$\Delta V_g = \min\left(\Delta V_{g,\text{req}} = \frac{\lambda_0 - \lambda_i}{\partial \lambda_i / \partial V_g}, \Delta V_{g,\max} \right) \tag{5-38}$$

where $\Delta V_{g,\text{req}}$ is the voltage increment required to increase the LM to λ_0. According to (5-38), if $\Delta V_{g,\text{req}}$ is smaller than $\Delta V_{g,\max}$, the maximum allowable increment at bus g, the voltage is increased by $\Delta V_{g,\text{req}}$. Otherwise, $\Delta V_{g,\max}$ is applied.

For this category, $\boldsymbol{u}^{(k)} = [\Delta V_g]$ is formed and LM vector $\boldsymbol{\lambda}$ is updated based on (5-36).

If the updated LM still does not meet λ_0, the algorithm will search the candidate location with the largest sensitivity among the remaining candidates in this category. If no such candidate exists, the algorithm will search Category 3.

5.3.3 Category 3) Load Shedding

Load shedding is a last resort for voltage stability control and is usually associated with the highest costs [61]. Therefore, it is the category with the lowest priority. Within this category, the algorithm will first search the candidate location with the sensitivity of the largest absolute value (e.g., bus *j*). It is assumed that the amount of load to be shed shares the same power factor, φ_j, with the load before shedding. The amount of load to be shed can be determined by

$$\begin{aligned} \Delta P_j &= \max\left(\Delta P_{j,\text{req}} = \frac{\lambda_0 - \lambda_i}{\partial\lambda_i/\partial P_j + \partial\lambda_i/\partial Q_j \cdot \tan\varphi_j}, \Delta P_{j,\text{lim}} \right) \\ \Delta Q_j &= \Delta P_j \cdot \tan\varphi_j \end{aligned} \tag{5-39}$$

where $\Delta P_{j,\text{lim}}$ is the limit of the real power shedding at location *j* and is a negative value indicating the decrease of load. In (5-39), the power factor remains the same throughout the second equation. For load shedding, control vector $\boldsymbol{u}^{(k)} = [\Delta P_j, \Delta Q_j]$ is formed and $\boldsymbol{\lambda}$ is updated based on (5-36).

If the updated $\boldsymbol{\lambda}$ does not meet λ_0, one more step will be taken in this category to decide upon the next location of load shedding. If after all available load-shedding controls have been applied and the system still cannot satisfy the desired LM, then additional controls should be included. For example, the limit for load shedding should be increased; otherwise, more locations should be considered for load shedding. The algorithm will exit and provide this warning to the system operator.

Note that the multiple steps are decision-steps only. After the algorithm ends, as shown in Figure 28, all the controls in the k-steps should be applied to the system in order

to improve the voltage stability margin. Furthermore, the sensitivity matrix is formed only once in the beginning and subsequently remains the same. In each step, the critical bus (i.e., the load bus with the smallest LM) is identified to determine the system level margin. Between these different steps, the critical bus may shift, as the increments of the margin resulting from the differentiation for different buses controls of previous steps are different.

5.4 Case Studies

In this section, the proposed WALMS and the multi-step control strategy are comprehensively tested on the IEEE 39-bus system, which is also known as the 10-machine ISO New England power system [65]. Extensive tests of the WALMS on the IEEE 14, 57, and 300-bus systems [64] are also conducted.

In order to verify the proposed WALMS, the IEEE 39-bus system is intentionally stressed by scaling up the load to 215% of the base load. The stressed system provides an insecure scenario where the LM of the system for N-0 (i.e., without any contingency) is under λ_0, which is set as 10% in this study. The LMs of buses 4, 7, 8, and 15, all below λ_0, are summarized in Table 7. According to the table, the LM of the system is determined by the bus 4, the critical bus, with a LM of 4.67%. In the remainder of this section, the results are based on analogously stressed system conditions, if not explicitly stated otherwise.

Table 7: Loading Margins of Insecure Buses

Bus No	*Bus 4*	*Bus 7*	*Bus 8*	*Bus 15*
Loading margin	4.67%	5.25%	4.91%	6.07%

5.4.1 Verification of WALMS w.r.t. Reactive Power Injection

The WALMS w.r.t. the reactive power injection is calculated based on (5-10) to (5-22). A sensitivity matrix, $[\partial \boldsymbol{\lambda}/\partial \boldsymbol{Q}_L]$, is obtained where the (i, j) element represents $\partial\lambda_i/\partial Q_j$ which is the sensitivity of LM of bus i w.r.t. the reactive load at bus j. The matrix is depicted in Figure 29(a). According to Figure 29(a), all $\partial\lambda_i/\partial Q_j$ values are negative which means an increase of Q load (i.e., reduction of Q compensation) at any bus j leads to a decrease of LM at any bus i. Another observation is that the diagonal elements and elements nearby are greater (in terms of absolute values) than other elements. This indicates the reactive compensation at nearby locations will impact the LM of buses more than all other locations.

To verify the sensitivity, 100 MVar (1.0 p.u.) of reactive compensation is applied at every load bus, respectively, and the LMs of all load buses after the change are calculated. The change of LM over -1.0 p.u. is considered as the actual sensitivity and is used to benchmark the proposed WALMS. The errors are summarized in Table 8. Moreover, in order to better illustrate the verification process, the self-sensitivity of bus 4, along with the cross-sensitivity of buses 4 to 12 are verified in Figure 29(b) and (c), respectively. Bus 4 is the critical bus and the accuracy regarding its LM is the most important for system operator.

As shown in Figure 29(b) and Figure 29(c), the load reduction (equivalent to reactive compensation) is conducted in 10 steps. The blue curve with square marks represent the actual LM after the change while the red curve with diamond curve represent the linear predicted LM by multiplying the WALMS with the amount of

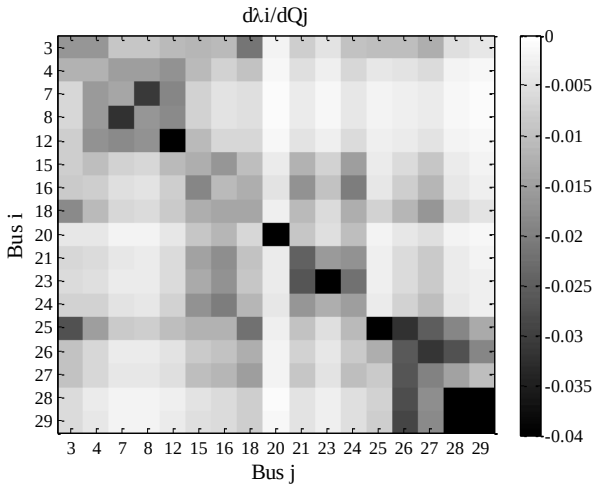

(a) Matrix of WALMS w.r.t. reactive power injection.

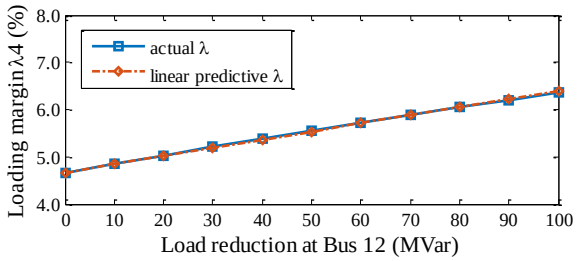

(b) Verification of self-sensitivity of bus 4.

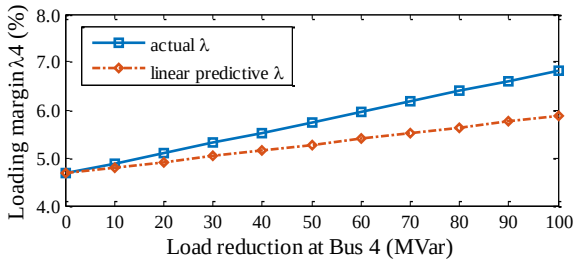

(c) Verification of cross-sensitivity of bus 4 to bus 12.

Figure 29. Verification of WALMS w.r.t. the reactive power injection

Table 8: Errors of WALMS to Reactive Power

	All buses	*Bus 4, 7, 8 and 15*
Max. Error (%)	2.37%	1.68%
Ave. Error (%)	0.53%	0.24%
Std. Dev. (%)	0.47%	0.27%

reduction. For the self-sensitivity, the error of LM at 100 MVar is less than 1.0%. For the cross-sensitivity, the error is less than 0.1%. According to Table 8, the average error is at 0.53% for all buses and 0.24% for the four insecure buses.

The errors regarding the insecure buses are more meaningful because control actions will be taken based on these values. For buses with a LM far beyond λ_0, their sensitivities are very unlikely to be used.

Note that the accuracy achieved by the improved WALMS has been significantly improved compared with [18] due to several modifications introduced in Section 5.2.1.

5.4.2 Verification of WALMS w.r.t. Real Power Injection

The WALMS w.r.t. real power is calculated according to (5-23) to (5-32). The sensitivity matrix, $[\partial \boldsymbol{\lambda}/\partial \boldsymbol{P}_L]$, is obtained and shown in Figure 30(a). Similar to Figure 29(a), the matrix is dominated by the diagonal and near-diagonal elements.

The self-sensitivity of bus 4 and the sensitivity of bus 4 to real power at bus 8, the largest cross-sensitivity, are depicted in Figure 30(b) and Figure 30(c), respectively. According to the figures, after 100 MW load reduction, the predicted LM is within 1% error compared with the actual LM.

The errors are summarized in Table 9. The maximum error and standard deviation of errors of the insecure buses are smaller than those of all buses. However, the average errors for the two categories are almost the same at around 0.6%.

5.4.3 Verification of WALMS w.r.t. Generator Terminal Voltage

The WALMS w.r.t. generator terminal voltage is calculated based on (5-33) to (5-35). The sensitivity matrix, $[\partial \boldsymbol{\lambda}/\partial \boldsymbol{V}_G]$, is shown in Figure 31(a). Note that the values

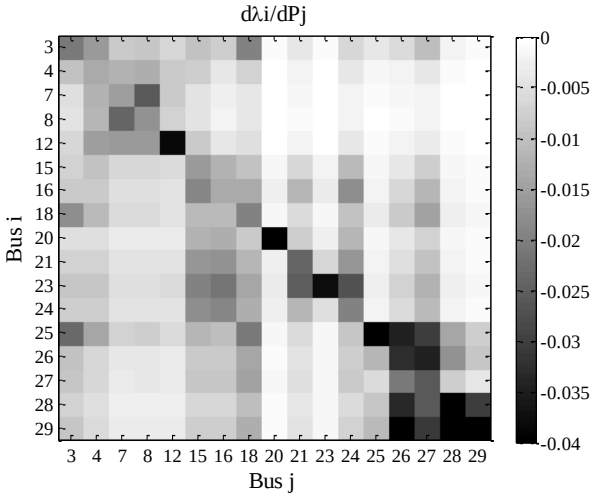

(a) Matrix of WALMS w.r.t. reactive power injection.

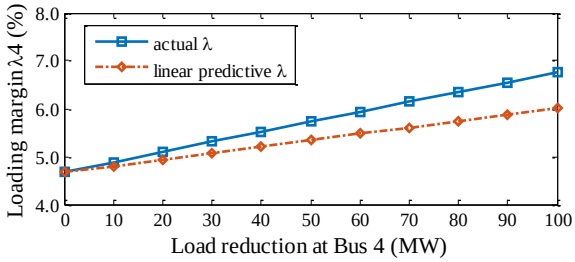

(b) Verification of self-sensitivity of bus 4.

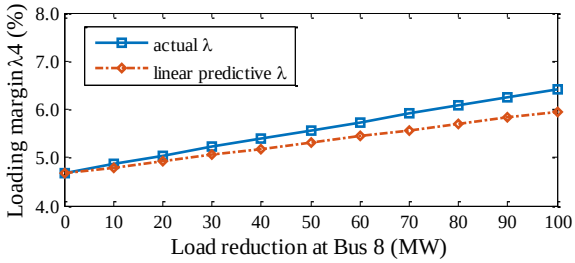

(c) Verification of cross-sensitivity of Bus 4 to Bus 8.

Figure 30. Verification of WALMS w.r.t. the real power injection.

Table 9: Errors of WALMS to Real Power

	All buses	*Bus 4, 7, 8, and 15*
Max. Error (%)	2.65%	1.23%
Ave. Error (%)	0.61%	0.68%
Std. Dev. (%)	0.44%	0.37%

shown in the figure are the values of the actual sensitivities, scaled by 0.05. This is because the upper bound of voltage variation is usually limited by the ability of the reactive power the generator can supply and usually a variation of 0.05 p.u. in terminal voltage is a large amount. Scaling by 0.05, the values are more comparable to the previous two types of sensitivities. Similarly, the generators near the load buses tend to have larger impact. Take bus 29 for example, the largest sensitivity is the one w.r.t. to generator 38, which is the nearest generator bus.

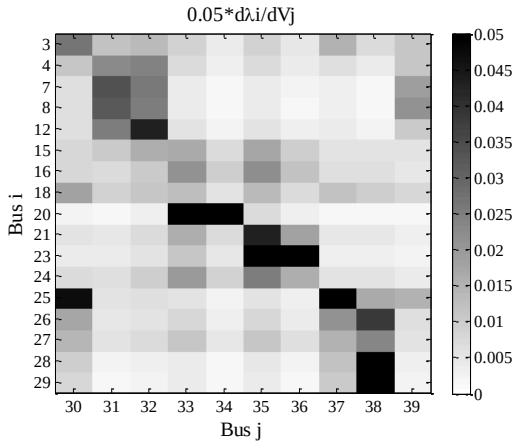

(a) Matrix of WALMS w.r.t. generator terminal voltage.

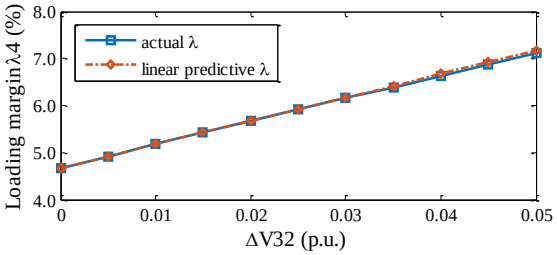

(b) Verification of sensitivity of bus 4 to terminal voltage of bus 32.

Figure 31. Verification of WALMS w.r.t. generator terminal voltage.

The largest sensitivity of bus 4, the WALMS of bus 4 to generator terminal voltage at bus 32 is depicted in detail in Figure 31(b). The errors of the sensitivity matrix

are summarized in Table 10. According to the table, the errors for all buses are similar to the previous two types, and the errors for the insecure buses are significantly smaller.

5.4.4 Validation of the Proposed Control Strategy

As mentioned in the beginning of the case study, a LM of 4.67% will leave the stressed system insecure because it is below the predefined threshold of 10%. With the sensitivity calculated in Subsections 5.4.1, 5.4.2, and 5.4.3, the proposed control strategy is applied.

The available control actions are listed in Table 11 (in positive value for convenience). The decisions at each step are listed in Table 12 and the LMs of the insecure buses (i.e., Bus 4, 7, 8, and 15) are shown in Figure 32.

- At Step 0, the algorithm detects that the system is insecure and the critical bus is bus 4 with a LM of 4.67%. Then the algorithm goes to Step 1 to determine which action to take.
- At Step 1, since there are two locations available for Category 1 control, the algorithm compares the WALMS of bus 4 to the reactive compensation at buses 7 and 8. The two sensitivities are -0.016 versus -0.015; thus, bus 7 is chosen and the amount to compensate is determined through (5-37). As shown in Figure 32, after Step 1, the LM is still below 10% and the critical bus remains bus 4.
- At Step 2, 100 MVar at bus 8 is compensated according to (5-37). An interesting change is that after this step, the critical bus shifts from bus 4 to bus 15 as depicted in Figure 32.

Table 10: Errors of WALMS to Generator Terminal Voltage

	All buses	*Bus 4, 7, 8 and 15*
Max. Error (%)	3.15%	0.56%
Ave. Error (%)	0.65%	0.25%
Std. Dev. (%)	0.58%	0.15%

Table 11: Candidate Control Actions

Control Category	*Location*	*Amount*
Category 1)	Bus 7, 8	100 MVar per Bus
Category 2)	Generator at Bus 32	0.05 p.u.
Category 3)	Bus 4, 7, 8, 15	100 MW per Bus

Table 12: Decision at Each Step

Step No.	*Category*	*Location*	*Amount*	*Critical Bus*
Step 1	1)	Bus 7	100 MVar	Bus 4
Step 2	1)	Bus 8	100 MVar	Bus 4
Step 3	2)	Bus 32	0.05 p.u.	Bus 15
Step 4	3)	Bus 15	44.5 MW	Bus 15

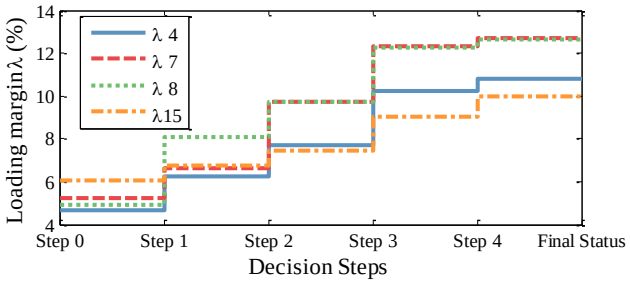

Figure 32. Loading margins of insecure buses at each decision step.

- At Step 3, the WALMS of bus 15 is examined rather than that of bus 4. Since Category 1 control is not available anymore, Category 2 voltage increment of the generator at bus 32 is selected and the amount to be increased is 0.05 p.u. determined by (5-38). After this step, bus 15 is still under 10%, and Category 3, the load shedding, is taken in Step 4.
- At Step 4, the most sensitive location for load shedding turns out to be bus 15 itself, and the amount to be shed is 44.5 MW and 21.3 MVar based on (39). After this step, the LM at bus 15 is improved to 10%, which terminates the algorithm and all the 4 steps should be applied to the system.

Indeed, after the four steps are applied, the actual LM of the system is 11.08% determined by bus 15. The total errors after the four steps are only 1.08%. The LM is within a reasonable range considering that in the decision steps, the algorithm does not require an update of the sensitivities.

5.4.5 Extensive Validation of WALMS on IEEE Test Systems

To further verify the WALMS as well as to demonstrate the application of the proposed WALMS, case studies on the IEEE 14, 57, and 300-bus systems [64] are conducted. The average error on the LMS of the top 1/3 insecure load buses are summarized in Table 13. The WALMS of the remaining 2/3 load buses are not included for practical reason since their loading margins are way above the critical region. As shown in Table 13, the proposed WALMS performs well in all the three test systems. Due to the length limit, the validation of the control strategy is not presented.

Table 13: Average Absolute Errors of WALMS in IEEE Test Systems

LMS w.r.t.	*IEEE 14-bus System*	*IEEE 57-bus System*	*IEEE 300-bus System*
Q (%)	1.00%	0.34%	0.76%
P (%)	1.27%	0.41%	1.64%
V (%)	0.38%	0.28%	0.07%

5.5 Conclusion

Two major contributions of this work can be summarized as: 1) the derivation of analytical expression of measurement- based WALMS using the coupled single-port circuit; and 2) the development of the multi-step control strategy for voltage stability based on the WALMS.

With the advantage of the simplicity of the measurement- based VSA, the WALMS is computationally efficient if compared with the existing model-based sensitivities which require the detailed system Jacobian matrix and eigenvalues calculation. The WALMS w.r.t. real power injection, reactive power injection, and generator terminal voltage, is derived and verified on the IEEE 14, 39, 57, and 300-bus systems. It has been demonstrated that the WALMS achieves good accuracy on the test systems. On the other hand, benefiting from the WALMS, a straightforward yet effective voltage control strategy is proposed. Validation of the control strategy on the 39-bus system shows decent results and the potential of online applications. Further, the application of the WALMS is not limited to the proposed control strategy but can be integrated in various applications for VSA and control. Those can be explored in future works.

CHAPTER 6

MITIGATING OVERESTIMATION OF VOLTAGE STABILITY MARGIN BY COUPLED SINGLE-PORT CIRCUIT MODELS

Wide-area measurement-based voltage stability assessment (VSA) by coupled single-port circuit models has been widely discussed recently. This method models the coupling effects of load buses within a meshed network into extra impedance of a single-port model for each load bus. In simulation studies, overestimations of voltage stability margin using this approach have been observed when critical load bus or buses are decoupled from other load buses. In this chapter, the overestimations are reported for the first time through examples and are further analyzed in details. Moreover, to mitigate such overestimations, two methods are proposed: one method uses a mitigation factor based on actual system reactive power response; the other method changes the types of certain weak generation buses when forming the coupled impedance. Both approaches are applied to a sample 4-bus system as well as the IEEE 118-bus system and successfully mitigate the overestimations.

6.1 Overestimations of Voltage Stability Margins

The coupled single-port circuit (CSPC) method has been introduced in Chapter 5.1 and is therefore not described again in this chapter. Although CSPC method achieves decent results in standard as well as practical test systems, overestimation can be observed in certain system topologies under certain load increasing scenarios as explained in this section.

6.1.1 Observed Overestimation in IEEE 118-Bus System

The overestimation is first observed in IEEE 118-bus system [64] when all the loads and generation are increasing proportionally. The loading margins of selected critical buses using CSPC method are shown in Figure 33. According to Figure 33, the most critical bus is Bus 44 with the smallest LM of 3.81 which means the system can support 381% of the base load. However, the LM of the system calculated through continuation power flow is 2.19 and is represented by the red line in Figure 33 (The continuation power flow result used in this study is from MATPOWER 5.1 [66] under MATLAB R2013b environment). It is clear that CSPC method overestimates the voltage stability margin of the IEEE 118-bus system in this case. The mismatch in terms of LM is around 1.62 or 162%.

Further examining the topology of the system around Bus 44, it is found that the small pocket containing Bus 44 is ‘isolated’ by several generator buses from the outside system as shown in Figure 34. In Figure 34, the open lines are branches that connect to the rest of the system. With this special topology, load buses 43, 44, and 45 are decoupled from other load buses because the elements of $\boldsymbol{Z}_{LL}$ in (5-2) corresponding to the coupling effects of outside load buses are all zero.

6.1.2 Analysis on the Sample 4-Bus System

To better demonstrate the correlation between the special isolation topology and the overestimation in voltage stability margin, a sample 4-bus system is built. The topology of the system is shown in Figure 35. The transmission lines are assumed to be identical with a reactance of 0.2 p.u. Load bus L_1 and L_2 each has a load of (100 MW, 30

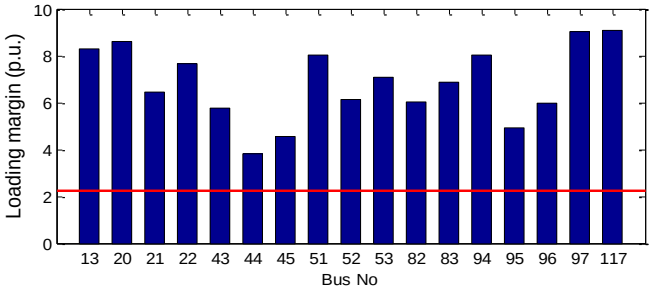

Figure 33. Loading margin of selected buses of IEEE 118-bus system.

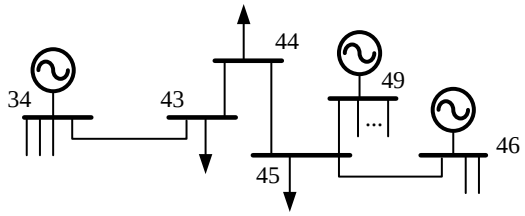

Figure 34. Partial diagram of IEEE 118-bus system near Bus 44.

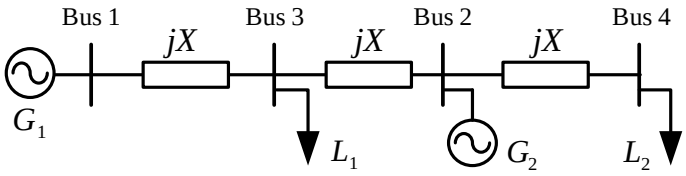

Figure 35. Sample 4-bus system.

MVar) with a 100 MVA base. The scheduled voltage magnitudes at both G_1 and G_2 are set to 1.0 p.u. G_1 (Bus 1) is the slack bus. G_2 (Bus 2) is a PV bus.

In the sample 4-bus system, L_1 is isolated by G_1 and G_2 from the other load bus L_2 and is to mimic the load pocket illustrated in Figure 35 in the IEEE 118-bus system.

Voltage stability studies using both CSPC method and the standard CPF are conducted on this system. Different scenarios of generation dispatch between G_1 and G_2 are considered. Because the resistances are all 0, if G_2 is set to generate PG_2 MW, the real power output of G_1 will be (200 – PG_2) MW. In the simulation, 10 different dispatch scenarios are considered where the output of G_2 increases from 20 MW to 200 MW. All the loads and generations are increased proportionally up until the voltage collapsing point.

The results are shown in Figure 36. The loading margins (LM) of load bus L_1 and L_2 calculated by the CSPC method are represented by the blue and green bars respectively. The red bars represent the LMs calculated with CPF.

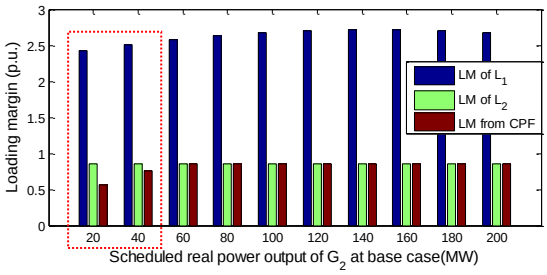

Figure 36. Loading margin of sample 4-bus system.

It is observed that, in the 10 scenarios, according to the CSPC method the critical bus is always L_2 (green bar). When the dispatched real power generation of G_2 at the base

case is larger than 60 MW, the results of the CSPC method are consistent with CPF. However, when the output of G_2 at the base case is less than 60 MW, the overestimation is observed where the estimated LMs of both L_1 and L_2 using CSPC are larger than the results from CPF.

Furthermore, for the scenario where the output of G_2 is 20 MW, the load impedances and the estimated Thevenin equivalent (TE) impedances of L_1 and L_2 using CSPC as load increases to up until the voltage collapsing point is plotted in Figure 37. As load increases, the load impedances (dashed curves) are decreasing while the TE impedances keep constant. Theoretically, at the collapsing point, the TE impedance should equal to the load impedance. However, in Figure 37, it is clearly that the two impedances of each load bus (same color) do not match at the end. Since the load impedances are the actual values from measurements, it is reasonable to state that the TE impedances are underestimated which eventually causes the overestimation of the voltage stability margin.

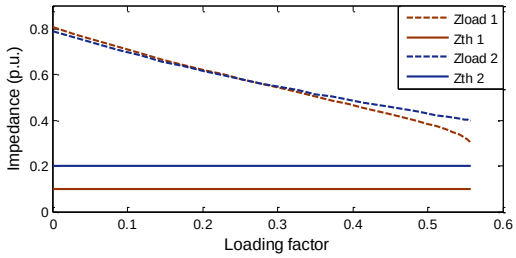

Figure 37. Load impedances v.s. TE impedance as load increases.

The isolation of L_1 to L_2 is just the reason to the underestimation of TE impedance depicted in Figure 37. According to (4), the coupling impedance of other load buses is

related to the corresponding element in $\boldsymbol{Z}_{LL}$. In this system, because of such isolation, the off-diagonal elements of $\boldsymbol{Z}_{LL}$ calculated through (2) are 0 and the TE impedance is just the self-impedance. However, the coupling effects of L_2 to L_1 shall not be completely ignored.

When the output of G_2 is much smaller than the load of L_2, the increase of load at L_2 will not be met by the increase of generation at G_2. Consequently, G_1 will support part of the increased load through Line 1-3 and Line 3-2. This increased flow will take some capacity of the transfer path from G_1 to L_1 and will reduce the voltage stability margin of L_1. By ignoring the coupling effects, the transfer capacity taken by L_2 will not be considered when calculate the voltage stability margin of L_1 which eventually results the illustrated overestimation of stability margin. This is the situation when the real power output of G_2 is 20 and 40 MW.

On the other hand, when G_2 has enough capacity to support L_2, this coupling efforts could be totally ignored since the increase of L_2 will not affect the flow of Line 1-3 or Line 3-2. This explains why as G_2 increases the overestimation disappears.

Moreover, in the critical load pocket of the IEEE 118-bus system depicted in Fig. 2, the generator bus, Bus 34, that isolates the load pocket from the rest of the system has a scheduled real power output of 0. That is to say the adjacent load buses to Bus 34 will easily cast their impacts on the stability margins of Bus 44 bypass Bus 34.

6.1.3 General Comments

Through the analysis on the 4-bus system and the 118-bus system, it can be concluded that the overestimation tends to happen when the following two conditions are

met:

1) The critical load bus or buses are isolated from the rest of load buses by several generator buses as depicted in Figure 34 or Figure 35.

2) Among the generator buses that separate the critical load bus or buses, at least one of them is a 'weak' generator bus whose real power output is so small that adjacent load buses will cast their impact bypass this generator bus. In the sample 4-bus system, the weak bus is G_2 and in the IEEE 118-bus system, the weak bus is Bus 34.

When the critical load bus or buses of a system meets the above mentioned two conditions, it is suggested to compare the results of CSPC method with other standard method in order to identify possible overestimation situations.

6.2 Methods to Mitigate the Overestimations

If the aforementioned overestimation is observed, it is crucial that an effective mitigation approach is applied. Otherwise, the overestimation will give the system operators optimistic results and may delay the identification of critical system operating conditions. In this section, two possible approaches to mitigate the overestimations are presented.

6.2.1 Modified Coupled Single-Port Model (MD)

This approach was originally proposed by Liu and Chu in [36] for compensating underestimation of voltage stability margin using coupled single-port circuit under non-proportional increased load.

In order to compensate the underestimation, a shunt admittance Y_{Ci} is added to the

*i*th equivalent branch as shown in Figure 38. Essentially, a mitigation factor α_i is multiplied to the TE impedance. α_i can be solved by letting the system reactive power response equal to reactive power response of the equivalent system as shown in Figure 38.

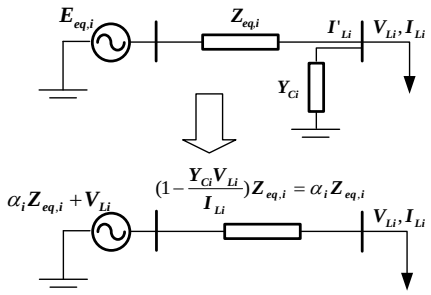

Figure 38. Equivalent series compensation for *i*th equivalent branch.

The detailed steps for solving α_i used in this work is the same as in [36] and is not elaborated here due to the page limit. Basically, it is to solve a quadratic equation.

A slight modification is made to let the mitigation factor work for the overestimation in this study. In [36], the voltage stability is underestimated which means the TE impedance is overestimated. Therefore, the authors set a feasible range of α_i to (0, 1] which forces the modified TE impedance less than the initial value. While, in order to mitigate the overestimation of voltage stability margin, or the underestimation of TE impedance in this study, the feasible range of α_i should be extended to (0, ∞). When α_i is larger than 1, the mitigation factor mitigates the overestimation introduced in this study, when it is smaller than 1, the mitigation factor compensates the underestimation reported in [36].

6.2.2 Negative Load Model (NL)

As explained in Chapter 6.1, the overestimation of stability margin is caused by isolation of critical load buses by weak generator buses. One straightforward solution is to change type of the weak generator buses to load buses and treat them as negative loads. This way, the isolation of the critical bus or buses is broken and the coupling of outside loads can be modeled into the TE impedance of the critical load since the corresponding elements in $\boldsymbol{Z_{LL}}$ calculated through (5-2) will be filled by non-zero elements.

Although to change the type of the weak generator buses is very simple, to identify the isolation and the weak generator buses is not an easy task. In this study, we assume this information is known. In the future work, an algorithm to identify the potential isolation and spot the weak generator buses will be explored.

6.3 Simulation Results

In this section, the two methods introduced in Chapter 6.2 are applied to the sample 4-bus system and the IEEE 118-bus system in order to mitigate the observed overestimations.

6.3.1 Application to the Sample 4-Bus System

The scenario where the output of G_2 is 20 MW in the base case is considered. As reported in Chapter 6.1.2, overestimation of voltage stability margin is observed under this scenario. The simulation is conducted from base case to voltage collapsing point using CPF as load proportionally increases.

The impedances of the equivalent circuit for L_1 as load increases are depicted in Figure 39. The blue dashed curve is the impedance of the load which decreases as load increases. The solid blue curve is the TE impedance solved using original CSPC method. The red curve is the TE impedance solved by Modified Coupled Single-Port Model (MD). The green curve is the TE impedance solved by Negative Load Model (NL).

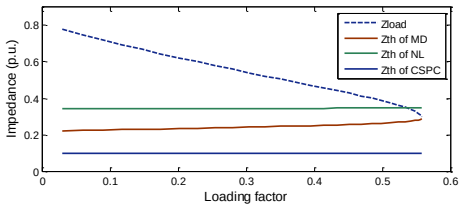

Figure 39. Impedances of equivalent circuit for L_1 as load increases.

The TE impedance of the MD method increases as load increases. The mitigation factors α for L_1 is illustrated Figure 40. The positive solutions are chosen while the negative ones are discarded. As can be seen in Figure 40, the kept mitigation factors are larger than 2.0 which justifies the necessity of extending the feasible range to $(0, \infty)$. In this case, based on the actual system reactive power response, the MD method successfully identifies the overestimation problem and adjusts the TE impedance in the correct positions. The TE impedance at the final moment meets the load impedance.

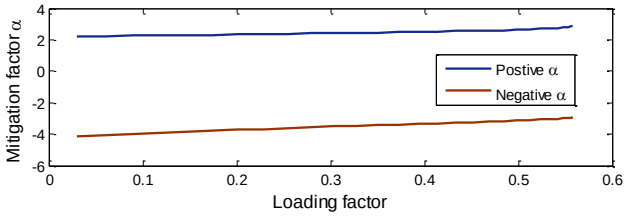

Figure 40. Mitigation factors of L_1 as load increases.

The TE impedance of NL method keeps mostly constant as load increases. However, the estimated TE impedance is slightly larger than the load impedance in the final moment. The impedance matching point actually comes earlier than the actual collapsing point. This means a slightly underestimation of loading margin is brought by NL method.However, both MD and NL methods improve the performance of the original CSPC method significantly. The loading margins estimated using different methods are demonstrated in Figure 41. The blue dashed curve is the LM from CPF and serves as the benchmark. The blue solid curve represents the results from original CSPC which is much higher than the correct values. The red curve represents the result from MD and the green curve represents the results from NL. According to Figure 41 both MD and NL achieve significant improvement in estimating the LM of L_1. MD introduces slightly overestimation while NL introduces slightly underestimation. Moreover, as load increases, the errors tend to reduce.

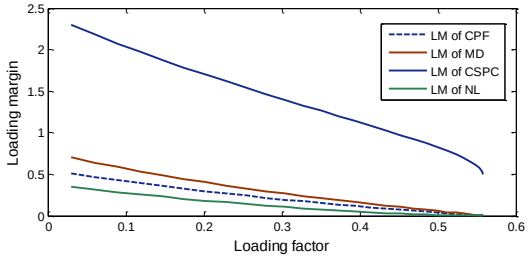

Figure 41. LMs of L_1 by different methods from base case to collapsing point.

6.3.2 Application to IEEE 118-Bus System

Both methods are then applied to the IEEE 118-bus system. When applying NL method, generator buses 34, 36, 41, and 42 are changed to load buses. These 4 generator

buses are all generator buses with 0 real power output near critical load buses.

The impedances of the equivalent circuit of Bus 44 are shown in Figure 42. The loading margins using different methods are depicted in Figure 43. As seen in Figure 42. the TE impedances are close to the load impedance at the final collapsing moment. According to Figure 43, NL method estimates the LM more accurately around base case. MD method, though less accurate around base case, is closer to the actual value when approaching the collapsing point. This is because the TE impedance estimated from MD method keeps being updated according to the actual system reactive response. As the operating point approaches closer to the collapsing point, MD approach shall be more accurate. On the other hand, the impedance of NL method keeps almost constant during the whole process. It gives a better estimation around base case, since along the projection, the TE impedance does not change much. However, at the final moment, the impedance of NL method does not exactly match the load impedance.

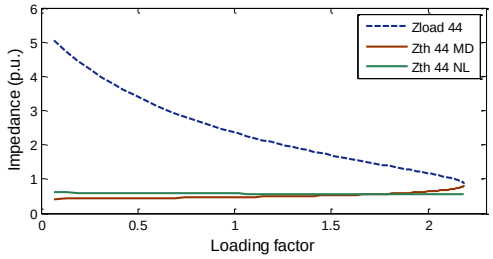

Figure 42. Impedances of equivalent circuit of Bus 44 in 118-bus system

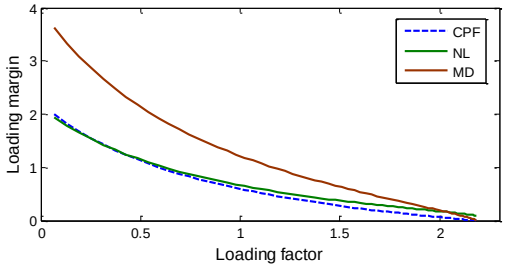

Figure 43. Loading margin of Bus 44 in 118-bus system

6.4 Conclusion

This work reports overestimation of voltage stability margin using coupled single-port circuit (CSPC) method. Through detailed analysis on a sample 4-bus system as well as the IEEE 118-bus system, it can be concluded that the observed overestimation occurs when the critical load bus or buses are isolated from rest of the system by weak generator buses. To mitigate such overestimation, two methods are raised, namely modified coupled single-port model (MD) method and negative load (NL) method. Both methods are applied to the 4-bus and 118-bus systems. Simulation results demonstrate that both methods mitigate the overestimation by original CSPC method. MD method will track the stability margin more accurately near the collapsing point while NL method can give a relative accurate prediction when the operating point is far from collapsing point. The authors suggest that when using CSPC method, it is necessary to check the two conditions summarized in Chapter 6.1.3 to identify potential overestimation problem. If the two conditions are met, the proposed methods should be taken to mitigate the overestimation.

CHAPTER 7

MEASUREMENT-BASED VOLTAGE STABILITY INDICATOR FOR VOLTAGE DEPENDENT LOAD

In most voltage stability analysis (VSA) literature including the recently developed measurement-based approaches, load model is considered as constant P and constant Q model, which is voltage independent. The constant PQ load model works fine under the assumption that the voltage of the load bus is close to nominal (1 p.u.). However, when the system is operating close to its limit, such assumption does not hold well. If the voltage is below the nominal level, the consumption of the real and reactive power should accordingly reduce. Constant PQ load is not able to model such voltage dependence characteristics and will eventually lead to a more conservative operating margin [13], [45], [67].

A widely-used load model that incorporates voltage dependence is the ZIP load model [68]. Under this load model, 100% of the real power is partitioned into constant impedance (Z) load, constant current (I) load, and constant power (P) load. The reactive power is also divided into Z, I, and P load models and the distribution may be different than the real power. Another voltage dependent load model is exponential load model [69]. Instead of representing ZIP component separately using a polynomial function, exponential load model uses relatively simple power function to represent the load characteristics.

With the phasor measurement units (PMUs) installed and the synchronized voltage and power consumption data captured, parameters of ZIP load models can be

easily identified [67], [70]. However, very few measurement-based VSA approaches incorporate the ZIP load models [71], [72] or exponential load models [73]. In [13], although ZIP load models are studied, the indicator will need to be used in combination with other system information such as reactive power depletion at certain generator buses to function well. Jia *et al.* proposed an improved L index in [69] which can consider the ZIP and exponential load model. However, it needs to use the system *Y* matrix and inherits some limitation of the *L* index.

The rest of this chapter is organized as follows: Chapter 7.1 studies the impact of two voltage dependent load models, ZIP load model and exponential load model, to voltage stability assessment; Chapter 7.2 introduces the proposed voltage stability indicator (VSI) for voltage dependent load models; Chapter 7.3 presents the case study on IEEE 14-Bus system and the implementation of the proposed VSI on large-scale test bed developed by the CURENT center; and Chapter 7.4 gives concluding remarks.

7.1 Impact of ZIP Load Model to Voltage Stability Assessment

The ZIP load model can be expressed mathematically as the following:

$$P = k_P \cdot (aV^2 + bV + c) \tag{7-1}$$

$$Q = k_Q \cdot (dV^2 + eV + f) \tag{7-2}$$

where P and Q are the actual real and reactive power consumption of the load; a, b, and c are the percentage of Z, I, and P load in real power respectively and should satisfy $a + b + c = 1$; d, e, and f are the percentage of Z, I, and P load in reactive power respectively and should satisfy $d + e + f = 1$; and k_P and k_Q are the loading factor of the load. In the

study, loading factor K (to represent both k_P and k_Q) is increased to stress the system and thereby to create the voltage collapsing scenario.

In (7-1) and (7-2), if a=d=1, the load is constant impedance load model; if b=e=1, the load is constant current load model; and if c=f=1, the load is constant power load.

In order to better understand the phenomena of voltage collapse under different load models, this section studies the impact of ZIP load model to voltage stability through both theoretical analysis and simulation study on a sample 2-bus system. Details of the sample 2-bus system can be found in the Appendix A.1. In this chapter, all the simulations are conducted using PSAT (Power System Analysis Toolbox) software [74], [75] in Matlab 2013b environment. Time domain simulation is used instead of traditional power flow based simulation in order to create the PMU data which is the input of the proposed algorithms.

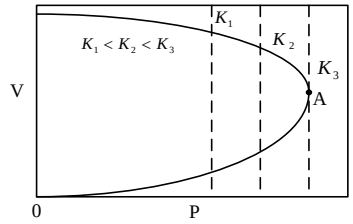

Figure 44. Constant power load and PV curve.

7.1.1 Constant P Load Model

When the load is modeled as constant power, the voltage collapse point will coincide with the maximum power point (nose point of the PV curve). The load model is voltage independent and the load characteristics can be described in the PV curve as a straight line perpendicular to the P axis as shown in Figure 44. By increasing the loading

factor, the load characteristics curve will move to the right of the figure. The collapsing point will be point A in Figure 44.

Among Z, I, and P load models, constant power load model is the most conservative model. If there are Z or I component load, the system may survive the nose point when the loading factor is increased. This will happen because at the nose curve the load consumption can be reduced due to the voltage dependent portion of the load when the load is increased.

To better illustrate the voltage collapse, time domain simulation is performed on a sample 2-Bus system. The 2-bus system consists of Bus 1, the generator bus, and Bus 2, the load bus. Bus 1 supports the load at Bus 2 through a single transmission line, Line 1-2. A synchronous generator with governor, exciter, and power system stabilizer is included in Bus 1.

The load at Bus 1 is increased 0.1% every 2 seconds. The PV curve of Bus 2 from the simulation is depicted in Figure 45. The system collapsed before going to the lower half of the PV curve. The largest power it can transfer is around 3.46 p.u.

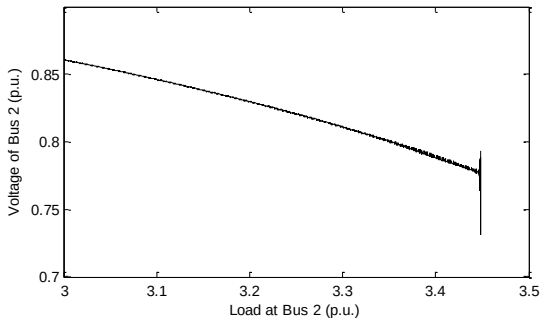

Figure 45. PV curve of Bus 2 in sample 2-bus system under P load.

7.1.2 Constant I Load Model

Constant current load is linearly dependent on the voltage magnitudes. The load characteristics of the constant current load can be described as a straight line crossing the origin on the PV curve as shown in Figure 46. By increasing the load current, the load characteristic line will lean towards the P axis more. Because the PV curve should also pass the origin, the load characteristics curve will always have an intersection point with the PV curve at the origin. This means, if 100% of constant current load is used, the system will not collapse due to voltage instability.

In order to demonstrate this finding, the load at Bus 2 is modeled as 100% constant I load and the loading factor is increased 0.4% per 1 second. The PV curve is depicted in Figure 47 and the lower part of PV curve is drawn in the simulation.

The reason that the system can operate through the nose curve towards the lower part of the PV curve is straightforward. After the nose curve, when loading factor is increasing, the real power consumption of the constant current load is also reducing due to its voltage dependent characteristics. In this simulation, it is demonstrated that constant current load will not contribute to voltage instability.

7.1.3 Constant Z Load Model

If the load is modeled as constant impedance, the voltage dependence is quadratic. Similarly, the load characteristics curve will cross the origin in the PV plane and therefore will always has an intersection point with the PV curve as shown in Figure 48. From this point of view, there will always be a solution when the Z load model is considered. From the view point of circuit theory, an increase of the loading factor is

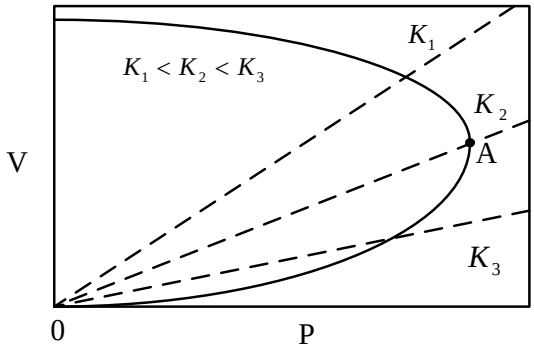

Figure 46. Constant current load and PV curve.

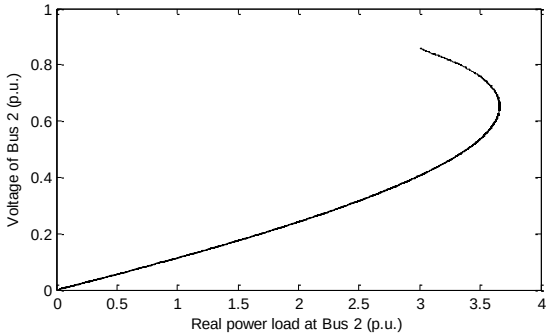

Figure 47. PV curve of Bus 2 in the sample 2-bus system under I load.

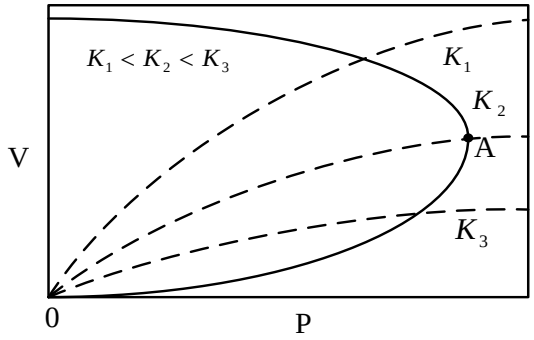

Figure 48. Constant impedance load and PV curve.

equivalent to a decrease of the load impedance. If a two bus equivalent of the load bus is considered, then no matter how small Z_{load} is, there will always be a solution of V. That is, in terms of voltage stability, constant impedance load will not contribute to voltage collapse.

The PV curve of constant Z load on the sample 2-bus system is identical to Figure 47 and therefore is not shown. In the simulation, it is demonstrated that constant Z load will not impact voltage stability.

7.1.4 ZIP Load Model

When all the three component exists in the load model or *a*, *b*, and *c* in (7-1) are all nonzero, the load characteristics curve will be a combination of three load characteristics. An illustration is given in Figure 49.

Because there are constant power loads, the load characteristics curve will no longer pass the origin. The intersection of the load curve and the P axis will be ($k_P \cdot c$, 0) according to (7-1) where $k_P \cdot c$ is just the real power of the constant power component. Because of this change, there will be a collapse point B where a further increase of loading factor K will result to an unsolved system as indicated in Figure 49.

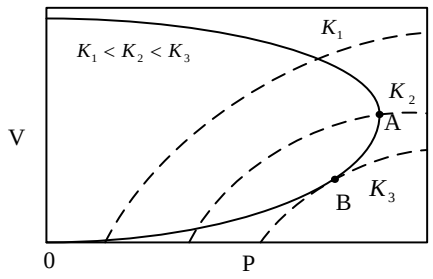

Figure 49. ZIP load and PV curve.

7.2 Impact of Exponential Load Model to Voltage Stability Assessment

The exponential load model describes the voltage dependence of load consumption as

$$P = k_P \cdot V^{\alpha_P} \tag{7-3}$$

$$Q = k_Q \cdot V^{\alpha_Q} \tag{7-4}$$

where α_P and α_Q are the coefficient for P and Q load. Although such load model is referred to as the "exponential" load model in literature, it is indeed a power function as shown in (7-3) and (7-4) where the exponent is constant. It will be referred to as the "exponential" load model in this dissertation for consistency with previous literatures.

The range of exponent α_P is usually [0, 2] as summarized in [76]. When α_P equals to 2, 1, and 0, the exponential load model is equivalent to constant Z, I, and P load respectively. When α_P is in the range of (1, 2), the load characteristics is similar to constant Z load model and is a concave function in PV plane as depicted in Figure 50(a). Similar to constant Z load, such characteristics will not contribute to voltage instability.

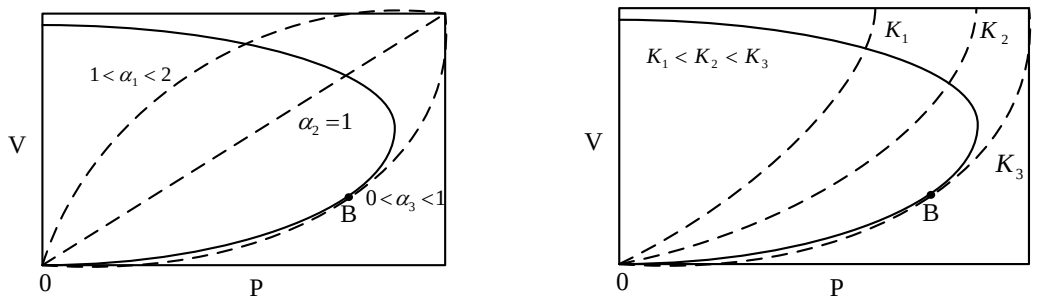

(a) under different α_P (b) with loading factor increase

Figure 50. Exponential load and PV curve.

When α_P is in the range of (0, 1), the load characteristics curve in PV plane becomes convex as shown in Figure 50(a). The load model will possibly contribute to voltage instability as the loading factor increases. As shown in Figure 50(b), when Point B is reached as the loading factor increases, the system is at the critical point. A slight increase of the loading factor, *K*, will push the load curve to the right further and will lead the system to no solution around the operating point. The voltage of the system will suddenly decrease to zero (the origin).

Note that the PV curve and the exponential load characteristics curve can have multiple intersection points other than the origin. Since it is hard to express the PV curve analytically, the number of intersections can hardly be discussed analytically. It is a good topic to discuss in the future for a thorough investigation.

7.3 Measurement-Based Voltage Stability Indicator for Voltage Dependent Load Models

As demonstrated in Figure 49, when the ZIP load model is in presence, Point B is the collapsing point rather than the maximum power point, A. Point B is the only solution of the power flow equation when the loading factor is K_3. Therefore, in Point B, the PV curve and the load characteristics curve (K_3) should have the same tangent line. In all other operating points on this PV curve, this condition is not met.

When an exponential load is considered and α_P is in the range of (0, 1), Point B in Figure 50(b) is the collapsing point rather than the maximum power point. Similar to the situation of ZIP load, in Point B and only in Point B, the PV curve and the load characteristics curve should share the same tangent line.

Essentially, the gradient of the tangent line in the PV plane describes the sensitivity between *P* and *V*. In this study, the sensitivity of *P* to *V*, i.e., $\partial P / \partial V$, is used instead of $\partial V / \partial P$. One of the consideration is that $\partial V / \partial P$ will be infinite at the maximum point A while $\partial P / \partial V$ is zero and can increase continuously across zero when the loading factor increases.

In the collapsing point B, the sensitivity of $\partial P / \partial V$ from the PV curve should equal to the $\partial P / \partial V$ from the load characteristic curve. For a load bus modelled as ZIP load, the Thevenin equivalent circuit can be calculated as mentioned in the previous chapters and can be represented in Figure 51. $\partial P / \partial V$ of the PV curve can be calculated based on the Thevenin equivalent to the left of the load bus.

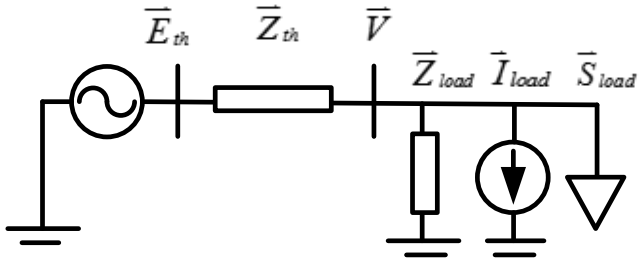

Figure 51. Equivalent circuit of a ZIP load bus.

In Chapter 5, it is derived that *P* and *V* of the load bus shall satisfy the following equation:

$$V_i^4 + \left(2P_i R_{eq,i} + 2Q_i X_{eq,i} - E_{eq,i}^2\right)V_i^2 + \left(R_{eq,i}^2 + X_{eq,i}^2\right)\left(P_i^2 + Q_i^2\right) = 0 \qquad (7\text{-}5)$$

If we take the derivative of *V* to both size of the equation in (7-5), $\partial P / \partial V$ of the PV curve can be calculated as

$$\frac{\partial P_i}{\partial V_i} = -\frac{2V_i^3 + V_i(2P_iR_{eq,i} + 2Q_iX_{eq,i} - E_{eq,i}^2)}{R_{eq,i}V_i^2 + P_iZ_{eq,i}^2} \tag{7-6}$$

On the other hand, $\partial P / \partial V$ of the ZIP load characteristics can be easily derived from (7-1). This is given by :

$$\frac{\partial P_i}{\partial V_i} = k_P(2aV_i + b) \tag{7-7}$$

Here, $\partial P / \partial V$ of the exponential load characteristics can be easily derived from (7-3). This is given by:

$$\frac{\partial P_i}{\partial V_i} = k_P \cdot \alpha_P \cdot V^{\alpha_P - 1} \tag{7-8}$$

As explained earlier, at the collapsing point B, the sensitivity calculated using (7-6) should equal to the sensitivity in (7-7) when the ZIP load model is used or should equal to the sensitivity in (7-8) when the exponential load model is used. It is proposed to use the angular difference between the two sensitivities as the indicator.

The proposed voltage stability indicator (VSI) can be expressed as:

$$VSI_i = \tan^{-1}\left(\partial P_i / \partial V_i \_ load\right) - \tan^{-1}\left(\partial P_i / \partial V_i \_ circuit\right) \tag{7-9}$$

When the calculated VSI or the angular difference between the two tangent lines is very small, voltage instability is indicated.

7.4 Simulation Results

In this section, the proposed VSI is tested on the IEEE 14-bus system and the large-scale test bed developed by the CURENT research center. All tests are performed using PSAT software in Matlab 2013b environment.

7.4.1 Results on the IEEE 14-Bus System with ZIP Load Model

The topology of the IEEE 14-bus system is shown in Figure 52 [64]. In the simulation, the loads at Buses 9, 10, 11, 12, 13, and 14, which consists of a load pocket in the upper part in Figure 52, are modeled as ZIP load with a percentage of 30% Z, 40% I, 30% P in both real and reactive power. Loading factors of the aforementioned load increases 0.4% per 1 seconds after the first 10 seconds of initialization.

The voltage magnitude of the 6 load buses are shown in Figure 53. As shown in the figure, the voltage collapsing happens at around 360 seconds. During the simulation, the voltage magnitude drops all the way towards the collapsing point.

The real power consumption at the 6 load buses is drawn in Figure 54. The loading factors are increasing as time passes. However, it is seen that the real power first increases and then decreases. It is clearly demonstrated that the maximum power point is not the voltage collapsing point. Also, it can be observed that although the percentage of the ZIP load is the same at different load buses, the time that the MPP is reached is different at different load buses.

The proposed VSI are calculated and depicted in Figure 55. The VSIs are zero at the first 20 seconds due to the initialization of the program. After the initialization, it is seen that the VSI is decreasing as the loading factor increases. At the time of voltage collapse, the VSI is very close to zero, indicating the sensitivities of P to V from the PV curve and the load model are very close. On the other hand, the VSI of [13], which is introduced in (4-20), is also applied and shown in Figure 56. By reaching 1, this VSI indicates unstable. It is seen that in around 260 seconds the VSI approaches 1. However,

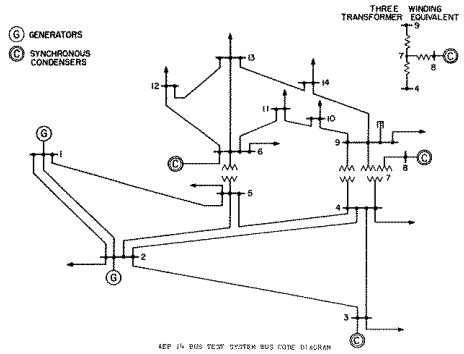

Figure 52. Topology of the IEEE 14-bus system.

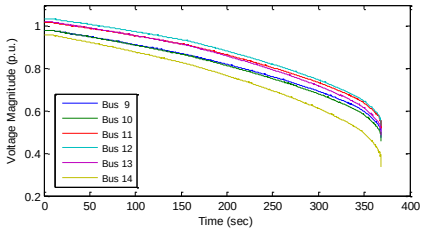

Figure 53. Voltage of 6 load buses in 14-bus system with the ZIP model.

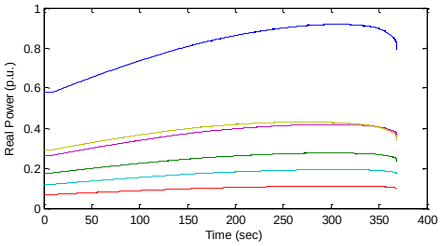

Figure 54. Real power consumption of 6 load buses.

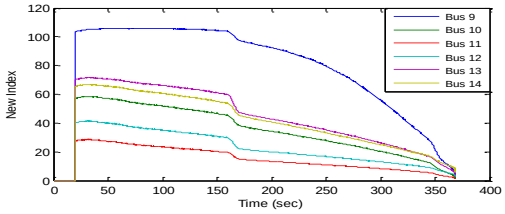

Figure 55. Proposed VSI for load buses in 14-bus system with the ZIP model.

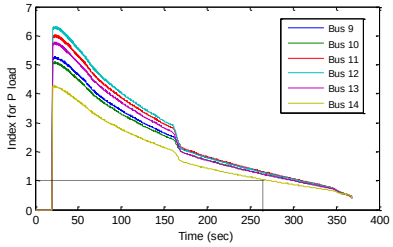

Figure 56. Index for P load in 14-bus system with ZIP model.

it is only the maximum power point for Bus 14 rather than the true collapsing point.

Also, the sensitivities of P to V from the PV curve and the load model are plotted in Figures 57 and 58, respectively. The PV sensitivity from the PV curve is first negative and then positive which is intuitive from Figure 49. The point where the PV sensitivity crosses zero corresponds to the maximum power point. It is seen that the sensitivity of Bus 14 reaches 0 around 260 seconds where the maximum power of Bus 14 is reached. On the other hand, the sensitivity from the load model is always positive and is increasing as shown in Figure 58.

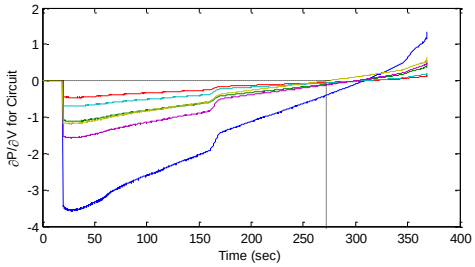

Figure 57. PV sensitivities from the circuits with ZIP load model.

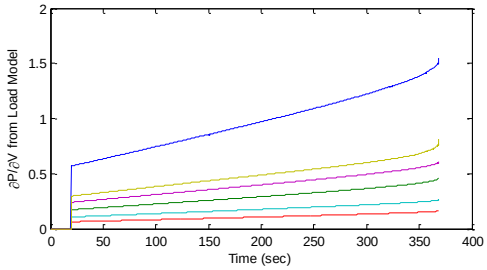

Figure 58. PV sensitivities from ZIP load model.

7.4.2 Results on IEEE 14-Bus System with Exponential Load Model

The same settings in Section 7.4.1 are applied here except that the load models of Buses 9, 10, 11, 12, 13, and 14 are changed to exponential load models with α_P and α_Q

both set to 0.5. The voltage magnitudes of the six load buses are depicted in Figure 59. Voltage collapse occurs around 267 seconds. From Figure 60, it is seen that the voltage collapse passes the maximum power point.

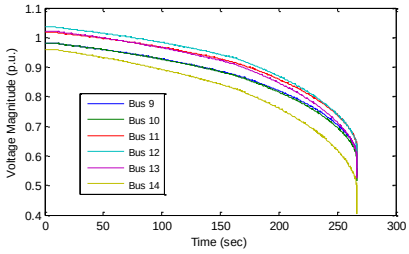

Figure 59. Voltage of load buses with exponential load model.

The proposed VSI is depicted in Figure 61. It is seen, at the collapsing point, the VSI is close to 0 accurately indicating the collapse. In Figure 62, the index for P load is presented. It is seen that in around 236 seconds, the index of Bus 14 reaches 1.0 and gives a conservative indication of voltage instability.

7.4.3 Results on Large-Scale Test Bed with ZIP Load Model

In this subsection, the proposed VSI is tested on a 181-bus reduced WECC (Western Electricity Coordinating Council) system which is developed at the CURENT research center as a large-scale test bed (LTB). The system has 181 buses and 29 generators. Time domain simulation is used in order to reach the voltage unstable point. The load buses in LADWP area (Los Angeles) are modeled as ZIP loads with 30% Z, 40% I and 30% P loads. In the simulation, the loading factors of load buses at LADWP area are increased 0.2% per second after the first 20 seconds initialization.

Voltage magnitudes of the 10 load buses are plot in Figure 63. It is seen that

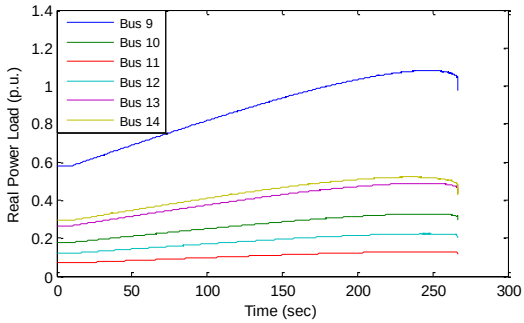

Figure 60. Real power load with exponential load mode.

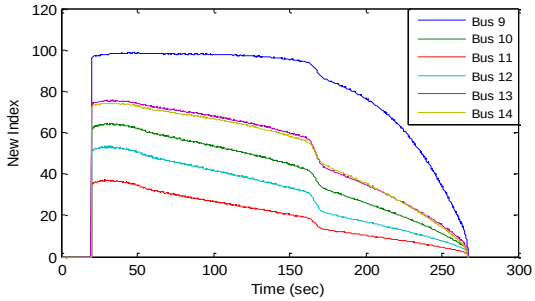

Figure 61. Proposed VSI in 14-bus system with exponential load model.

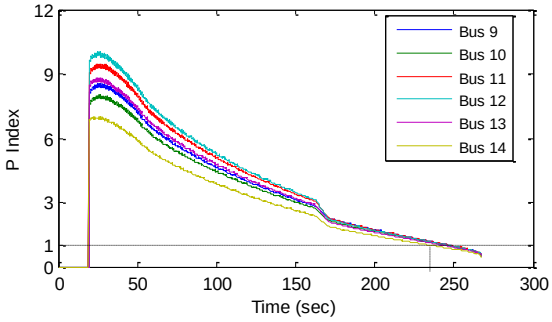

Figure 62. Index for P load in 14-bus system with exponential load model.

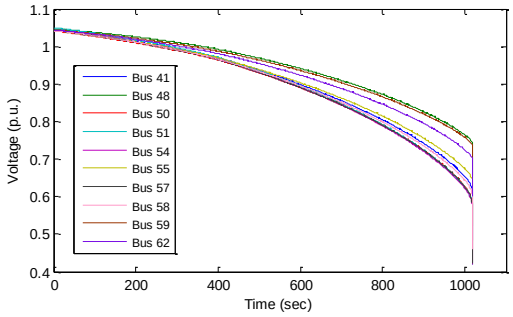

Figure 63. Voltage magnitudes of load buses in 181-bus WECC system.

voltage collapse happens around 1010 seconds. The real power loads of the 10 buses are depicted in Figure 64. At the end of the simulation, the real power loads are decreasing as loading factor increases. The maximum power point of Bus 50 is reached a little after 800 seconds.

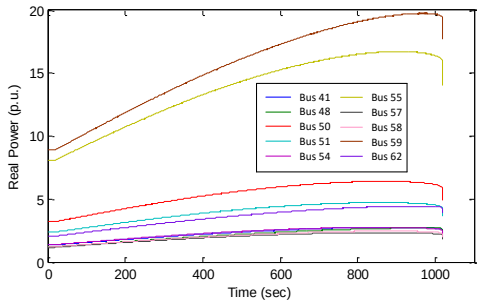

Figure 64. Real power of load buses in 181-bus WECC system.

The proposed VSIs are calculated on the 10 load buses and the results are shown in Figure 65. The VSIs are decreasing during the simulation and eventually reduce to close to 0 at the collapsing point. In comparison, The VSIs for P loads are also calculated and plotted in Figure 66. The VSIs for P load indicate instability around 850 seconds when it reaches 1.0. It is too conservative since the actual instability will not be reached 160 seconds later.

The PV sensitivities from the Thevenin circuit are shown in Figure 67. The sensitivities are first negative and increase as time passes. At the collapsing point, the sensitivities are positive indicating that the operating points are at lower half of the PV curves. The sensitivities are zoomed in around 800 seconds in Figure 68 where most of the sensitivity curves cross the zero line. It is seen that the first occurrence of sensitivity reaches 0 is around 860 seconds indicating that this load bus reaches its maximum power

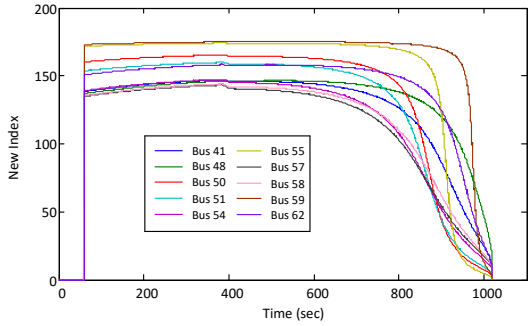

Figure 65. Proposed VSI in 181-bus WECC system.

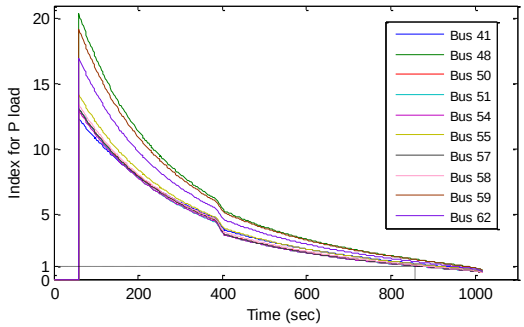

Figure 66. VSI for P load in 181-bus WECC system.

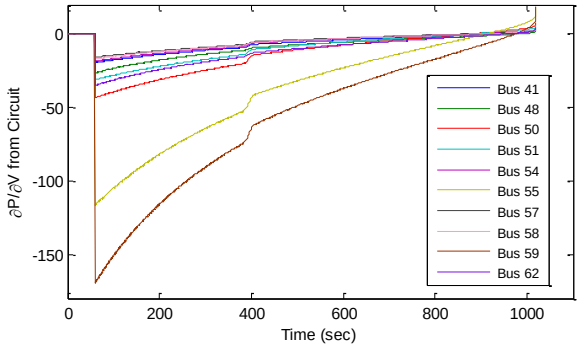

Figure 67. PV sensitivities from PV curve.

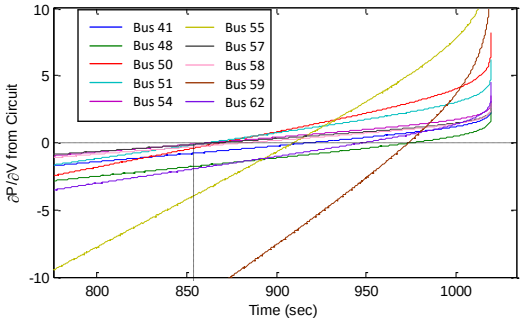

Figure 68. PV sensitivities from PV curve around 800 seconds.

point. Also, this time is aligned with the VSI in Figure 66 reaching 1.0. The sensitivities from the ZIP load model are shown in Figure 69. The sensitivities are always positive and are increasing through the whole simulation.

7.4.4 Results on Large-Scale Test Bed with Exponential Load Model

The same settings in Section 7.4.3 are applied here except that the load models of LADWP area are changed to exponential load models with α_P and α_Q set to 0.5. The voltage magnitude of Los Angeles area load buses are depicted in Figure 70. Voltage collapse occurs around 850 seconds.

The proposed VSI is calculated and illustrated in Figure 71. According to the figure, the proposed indicator decreases to zero at around 850 seconds. In comparison, the index for P load is shown in Figure 72. It is seen that the indicator reaches 1.0 around 750 seconds which is 100 seconds earlier than the actual collapsing point.

Through all the simulation results in section 7.4, it is demonstrated that the proposed VSI is effective in indicating the voltage collapse when voltage dependent load models, including both ZIP and exponential models, are in presence. On the other hand, traditional VSI will lead to a much more conservative results.

7.5 Conclusion

This chapter first analyzes the impact of ZIP and exponential load models to voltage stability through theoretical analysis and simulation. Then, a novel voltage stability index that is applicable to both ZIP and exponential load models is proposed with the utilization of special characteristics at the collapsing point where the PV curve

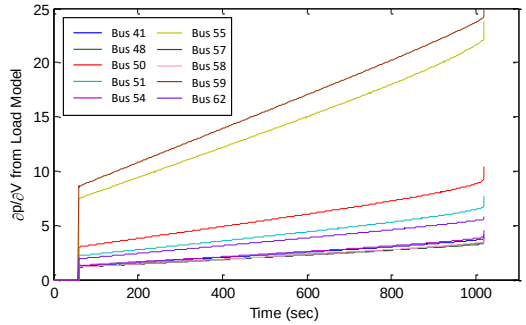

Figure 69. PV sensitivities from ZIP load model.

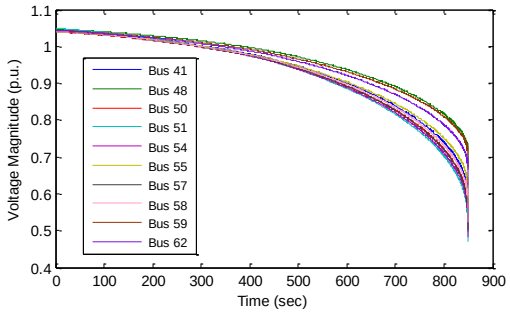

Figure 70. Voltage of LA area load with exponential load model.

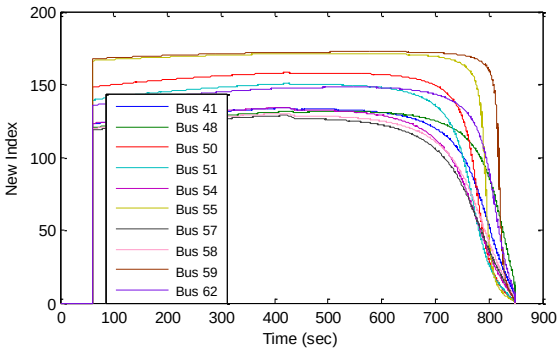

Figure 71. Proposed VSI for LA area load with exponential load model.

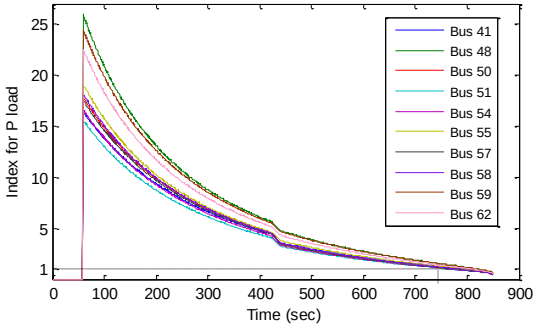

Figure 72. Index for P load in LTB with exponential load model.

and the load curve shares the same tangent line. Simulation results on both of the IEEE 14-bus system and the 181-bus WECC system developed by the CURENT center demonstrate promising results of the proposed VSI in indicating voltage instability when the ZIP and exponential load models are used.

CHAPTER 8

CONCLUSION AND RECOMMENDATIONS

8.1 Conclusion

This dissertation focuses on measurement-based voltage stability assessment and control. The contribution is summarized as follows:

First, a comparative study on four TE identification methods (i.e., least squares method (LS), Tellegen's theorem method (TT), adaptive method (AD), and coupled single-port circuit method (CP)) is presented. It serves as a guide for researchers to choose proper TE identification methods for their measurement-based VSA application.

Second, a hybrid voltage stability assessment (VSA) method for N-1 contingency is proposed which extends the application of measurement-based approach to the computational intense contingency analysis. With the proposed model-based contingency sensitivity and the measurement-based VSA technique, the hybrid VSA method solves the challenge of VSA under contingency cases.

Third, the proposed analytical expression of measurement-based WALMS provides a versatile measurement-based tool for voltage stability assessment and control. It can aid the system operators' decisions in real time under unstable or insecure operating conditions.

Fourth, the development of the multi-step control strategy for voltage stability based on the WALMS provides a real-time application of measurement-based voltage stability control.

Fifth, overestimation of voltage stability margin using coupled single-port circuit model is reported for the first time, and mitigation methods are proposed to correct such overestimation.

Finally, the impact of load model in voltage stability assessment is studied and a novel VSI for both ZIP load model and exponential load model is proposed.

8.2 Future Work

The following directions may be considered as future tasks in the frame of measurement-based voltage stability assessment and control.

1) Demand response can be included in the existing measurement-based voltage stability control scheme in order to lower the costs of preventive or corrective voltage stability controls.

2) More scenarios and demonstrations will be developed on large-scale power systems.

LIST OF REFERENCES

[1] C. W. Taylor, *Power System Voltage Stability*. New York: McGraw Hill Education, 1994.

[2] F. Li and Y. Wei, "A Probability-Driven Multilayer Framework for," vol. 3, no. 3, pp. 455–464, 2012.

[3] Y. Xu, Q. Hu, and F. Li, "Probabilistic model of payment cost minimization considering wind power and its uncertainty," *IEEE Trans. Sustain. Energy*, vol. 4, no. 3, pp. 716–724, 2013.

[4] C. Huang, F. Li, and Z. Jin, "Maximum Power Point Tracking Strategy for Large-Scale Wind Generation Systems Considering Wind Turbine Dynamics," *IEEE Trans. Ind. Electron.*, vol. 62, no. 4, pp. 2530–2539, 2015.

[5] L. Bai, F. Li, H. Cui, T. Jiang, H. Sun, and J. Zhu, "Interval optimization based operating strategy for gas-electricity integrated energy systems considering demand response and wind uncertainty," *Appl. Energy*, vol. 167, pp. 270–279, 2016.

[6] H. Chen, Y. Kong, G. Li, and L. Bai, "Conditional value-at-risk-based optimal spinning reserve for wind integrated power system," *Int. Trans. Electr. Energy Syst.*, p. n/a–n/a, 2016.

[7] H. Chen, R. Zhang, G. Li, L. Bai, and F. Li, "Economic dispatch of wind integrated power systems with energy storage considering composite operating costs," *IET Generation, Transmission & Distribution*, vol. 10, no. 5. pp. 1294–1303, 2016.

[8] H. Hu, Q. Shi, Z. He, J. He, and S. Gao, "Potential Harmonic Resonance Impacts of PV Inverter Filters on Distribution Systems," *IEEE Transactions on Sustainable Energy*, vol. 6, no. 1. pp. 151–161, 2015.

[9] H. Yuan and F. Li, "A Comparative Study of Measurement-Based Thevenin Equivalents Identification Methods," in *North American Power Symposium*, 2014, pp. 1–6.

[10] S. Nuthalapati and A. G. Phadke, "managing the grid," *IEEE Power Energy Mag.*, vol. 13, no. 5, pp. 10–12, 2015.

[11] J. Chai, J. Zhao, W. Yao, J. Guo, and Y. Liu, "Application of Wide Area Power System Measurement for Digital Authentication," in *T&D Conference and Exposition*, 2016, pp. 1–5.

[12] J. Guo, Y. Zhang, M. A. Young, M. J. Till, A. Dimitrovski, Y. Liu, P. Williging, and Y. Liu, "Design and Implementation of a Real-Time Off-Grid Operation Detection Tool from a Wide-Area Measurements Perspective," *IEEE Trans. Smart Grid*, vol. 6, no. 4, pp. 2080–2087, 2014.

[13] B. Milosevic and M. Begovic, "Voltage-stability protection and control using a wide-area network of phasor measurements," *IEEE Trans. Power Syst.*, vol. 18, no. 1, pp. 121–127, 2003.

[14] T. Jiang, H. Yuan, H. Jia, N. Zhou, and F. Li, "Stochastic subspace identification-

based approach for tracking inter-area oscillatory modes in bulk power system utilising synchrophasor measurements," *IET Gener. Transm. Distrib.*, vol. 9, no. 15, pp. 2409–2418, 2015.

[15] T. Jiang, L. Bai, H. Jia, H. Yuan, and F. Li, "Identification of voltage stability critical injection region in bulk power systems based on the relative gain of voltage coupling," *IET Gener. Transm. Distrib.*, vol. 10, no. 7, pp. 1495–1503, 2016.

[16] T. Jiang, H. Jia, H. Yuan, N. Zhou, and F. Li, "Projection Pursuit : A General Methodology of Wide-Area Coherency Detection in Bulk Power Grid," *IEEE Trans. Power Syst.*, pp. 1–11, 2015.

[17] T. Jiang, Y. Mu, H. Jia, N. Lu, H. Yuan, J. Yan, and W. Li, "A Novel Dominant Mode Estimation Method for Analyzing Inter-Area Oscillation in China Southern Power Grid," *IEEE Trans. Smart Grid*, pp. 1–12, 2016.

[18] H. Yuan, T. Jiang, H. Jia, F. Li, Y. Mishra, H. Chen, and G. Li, "Real-Time Wide-area Loading Margin Sensitivity (WALMS) in Power Systems," in *IEEE PES General Meeting*, 2015, pp. 1–5.

[19] V. Ajjarapu and C. Christy, "The continuation power flow: A tool for steady state voltage stability analysis," *IEEE Trans. Power Syst.*, vol. 7, no. 1, pp. 416–423, 1992.

[20] H. D. Chiang, A. J. Flueck, K. S. Shah, and N. Balu, "CPFLOW: a practical tool for tracing power system steady-state stationary behavior due to load and generation variations," *IEEE Trans. Power Syst.*, vol. 10, no. 2, pp. 623–634, 1995.

[21] X. Fang, F. Li, Q. Hu, and N. Gao, "System load margin evaluation using mixed-integer conic optimization," in *2015 North American Power Symposium, NAPS 2015*, 2015, pp. 1–6.

[22] X. Fang, F. Li, and N. Gao, "Probabilistic Available Transfer Capability Evaluation for Power Systems with High-Penetration Wind Power," in *13th International Conference on Probabilistic Methods Applied to Power Systems (PMAPS)*, 2014, pp. 1–6.

[23] B. Wang, X. Fang, X. Zhao, and H. Chen, "Bi-Level Optimization for Available Transfer Capability Evaluation in Deregulated Electricity Market," *Energies*, vol. 8, no. 12, p. 12370, 2015.

[24] X. Fang, F. Li, Y. Wei, R. Azim, and Y. Xu, "Reactive power planning under high penetration of wind energy using Benders decomposition," *IET Generation, Transmission & Distribution*, vol. 9, no. 14. pp. 1835–1844, 2015.

[25] X. Fang, F. Li, and Y. Xu, "Reactive power planning considering high penetration of wind energy," *2014 IEEE PES T&D Conference and Exposition*. pp. 1–5, 2014.

[26] R. Torquato, Q. Shi, W. Xu, and W. Freitas, "A Monte Carlo Simulation Platform for Studying Low Voltage Residential Networks," *Smart Grid, IEEE Trans. (Volume5 , Issue 6)*, vol. 5, no. 6, pp. 2766–2776, 2014.

[27] X. Fang, F. Li, Y. Wei, and H. Cui, “Strategic scheduling of energy storage for load serving entities in locational marginal pricing market,” *IET Generation, Transmission & Distribution*, vol. 10, no. 5. pp. 1258–1267, 2016.

[28] X. Fang, Q. Hu, F. Li, B. Wang, and Y. Li, “Coupon-Based Demand Response Considering Wind Power Uncertainty: A Strategic Bidding Model for Load Serving Entities,” *IEEE Transactions on Power Systems*, vol. 31, no. 2. pp. 1025–1037, 2016.

[29] J. S. Vardakas, N. Zorba, and C. V. Verikoukis, “A Survey on Demand Response Programs in Smart Grids: Pricing Methods and Optimization Algorithms,” *IEEE Commun. Surv. Tutorials*, vol. 17, no. c, pp. 1–1, 2014.

[30] H. Cui, F. Li, Q. Hu, L. Bai, and X. Fang, “Day-ahead coordinated operation of utility-scale electricity and natural gas networks considering demand response based virtual power plants,” *Appl. Energy*, vol. 176, pp. 183–195, 2016.

[31] K. Vu, M. M. Begovic, D. Novosel, and M. M. Saha, “Use of local measurements to estimate voltage-stability margin,” *IEEE Trans. Power Syst.*, vol. 14, no. 3, pp. 1029–1035, 1999.

[32] I. Smon, S. Member, and G. Verbiˇ, “Local Voltage-Stability Index Using Tellegen ’ s Theorem,” vol. 21, no. 3, pp. 1267–1275, 2006.

[33] S. Corsi and G. N. Taranto, “A real-time voltage instability identification algorithm based on local phasor measurements,” *IEEE Trans. Power Syst.*, vol. 23, no. 3, pp. 1271–1279, 2008.

[34] Y. Wang, I. R. Pordanjani, W. Li, W. Xu, T. Chen, E. Vaahedi, and J. Gurney, “Voltage stability monitoring based on the concept of coupled single-port circuit,” *IEEE Trans. Power Syst.*, vol. 26, no. 4, pp. 2154–2163, 2011.

[35] S. M. Abdelkader and D. J. Morrow, “Online Tracking of Thévenin Equivalent Parameters Using PMU Measurements,” vol. 27, no. 2, pp. 975–983, 2012.

[36] J. Liu, S. Member, and C. Chu, “Wide-Area Measurement-Based Voltage Stability Indicators by Modified Coupled Single-Port Models,” *IEEE Trans. Power Syst.*, vol. 29, no. 2, pp. 756–764, 2014.

[37] K. Sun, F. Hu, and N. Bhatt, “A new approach for real-time voltage stability monitoring using PMUs,” *2014 IEEE Innovative Smart Grid Technologies - Asia (ISGT ASIA)*. pp. 232–237, 2014.

[38] D. Zhou, J. Guo, Y. Zhang, J. Chai, H. Liu, Y. Liu, C. Huang, X. Gui, and Y. Liu, “Distributed Data Analytics Platform for Wide-Area Synchrophasor Measurement Systems,” *IEEE Trans. Smart Grid*, pp. 1–9, 2016.

[39] Y. Liu, L. Zhan, Y. Zhang, P. N. Markham, D. Zhou, J. Guo, Y. Lei, G. Kou, W. Yao, J. Chai, and Y. Liu, “Wide-Area-Measurement System Development at the Distribution Level: An FNET/GridEye Example,” *IEEE Trans. Power Deliv.*, vol. 31, no. 2, pp. 721–731, 2016.

[40] H. Yuan and F. Li, “Hybrid voltage stability assessment (VSA) for N−1

contingency," *Electr. Power Syst. Res.*, vol. 122, pp. 65–75, 2015.

[41] S. N. Singh and S. C. Srivastava, "Improved voltage and reactive power distribution factors for outage studies," *IEEE Trans. Power Syst.*, vol. 12, no. 3, pp. 1085–1093, 1997.

[42] P. A. Ruiz and P. W. Sauer, "Voltage and Reactive Power Estimation for Contingency Analysis Using Sensitivities," vol. 22, no. 2, pp. 639–647, 2007.

[43] S. Greene, I. Dobson, and F. L. Alvarado, "Sensitivity Of The Loading Margin To Voltage Collapse With Respect To Arbitrary Parameters - Power Systems, IEEE Transactions on," vol. 12, no. 1, 1997.

[44] H. Li, H.-D. Chiang, H. Yoshida, Y. Fukuyama, and Y. Nakanishi, "The generation of ZIP-V curves for tracing power system steady state stationary behavior due to load and generation variations," in *1999 IEEE Power Engineering Society Summer Meeting. Conference Proceedings*, 1999, vol. 2, pp. 1–5.

[45] S. H. Li, H. D. Chiang, and S. Liu, "Analysis of composite load models on load margin of voltage stability," in *International Conference on Power System Technology*, 2006, pp. 1–7.

[46] W. Li, T. Chen, and W. Xu, "On impedance matching and maximum power transfer," *Electr. Power Syst. Res.*, vol. 80, no. 9, pp. 1082–1088, Sep. 2010.

[47] Y. Wang, W. Li, and J. Lu, "A new node voltage stability index based on local voltage phasors," *Electr. Power Syst. Res.*, vol. 79, no. 1, pp. 265–271, Jan. 2009.

[48] G. Verbič, M. Pantoš, and F. Gubina, "On voltage collapse and apparent-power losses," *Electr. Power Syst. Res.*, vol. 76, no. 9–10, pp. 760–767, Jun. 2006.

[49] M. Glavic and T. Van Cutsem, "Wide-area detection of voltage instability from synchronized phasor measurements. Part II: Simulation Results," *IEEE Trans. Power Syst.*, vol. 24, no. 3, pp. 1417–1425, 2009.

[50] M. Parniani, J. H. Chow, L. Vanfretti, B. Bhargava, and A. Salazar, "Voltage stability analysis of a multiple-infeed load center using phasor measurement data," *2006 IEEE PES Power Syst. Conf. Expo. PSCE 2006 - Proc.*, pp. 1299–1305, 2006.

[51] F. Hu, K. Sun, A. Del Rosso, E. Farantatos, and N. Bhatt, "Measurement-Based Real-Time Voltage Stability Monitoring for Load Areas," *IEEE Trans. Power Syst.*, 2015.

[52] D. Q. Zhou, S. Member, U. D. Annakkage, S. Member, and A. D. Rajapakse, "Online Monitoring of Voltage Stability Margin Using an Artificial Neural Network," vol. 25, no. 3, pp. 1566–1574, 2010.

[53] M. M. Begovic and A. G. Phadke, "CONTROL OF VOLTAGE STABILITY USING SENSITIVITY ANALYSIS," *IEEE Trans. Power Syst.*, vol. 7, no. 1, 1992.

[54] S. Greene, I. Dobson, S. Member, and F. L. Alvarado, "Sensitivity of Transfer

Capability Margins With a Fast Formula," vol. 17, no. 1, pp. 34–40, 2002.

[55] F. Capitanescu, T. Van Cutsem, and S. Member, "Unified Sensitivity Analysis of Unstable or Low Voltages Caused by Load Increases or Contingencies," *IEEE Trans. Power Syst.*, vol. 20, no. 1, pp. 321–329, 2005.

[56] A. J. Flueck, R. Gonella, and J. R. Dondeti, "A new power sensitivity method of ranking branch outage contingencies for voltage collapse," *IEEE Trans. Power Syst.*, vol. 17, no. 2, pp. 265–270, 2002.

[57] N. Amjady and M. Esmaili, "Application of a New Sensitivity Analysis Framework for Voltage Contingency Ranking," *IEEE Trans. Power Syst.*, vol. 20, no. 2, pp. 973–983, May 2005.

[58] F. Capitanescu and T. Van Cutsem, "Preventive control of voltage security margins: a multicontingency sensitivity-based approach," *IEEE Trans. Power Syst.*, vol. 17, no. 2, pp. 358–364, May 2002.

[59] F. M. Echavarren, E. Lobato, and L. Rouco, "A corrective load shedding scheme to mitigate voltage collapse," *Int. J. Electr. Power Energy Syst.*, vol. 28, no. 1, pp. 58–64, Jan. 2006.

[60] V. C. Nikolaidis and C. D. Vournas, "Design strategies for load-shedding schemes against voltage collapse in the Hellenic System," *IEEE Trans. Power Syst.*, vol. 23, no. 2, pp. 582–591, 2008.

[61] T. Amraee, a. M. Ranjbar, B. Mozafari, and N. Sadati, "An enhanced under-voltage load-shedding scheme to provide voltage stability," *Electr. Power Syst. Res.*, vol. 77, no. 8, pp. 1038–1046, Jun. 2007.

[62] W. W. Price, *Dynamic Equivalents in Transient Stability Studies*. 1974.

[63] a. M. Abed, "WSCC voltage stability criteria, undervoltage load sheddingstrategy, and reactive power reserve monitoring methodology," *1999 IEEE Power Eng. Soc. Summer Meet. Conf. Proc. (Cat. No.99CH36364)*, vol. 1, pp. 191–197, 1999.

[64] "Power systems test case archive," *University of Washington*. [Online]. Available: http://www.ee.washington.edu/research/pstca/.

[65] M. A. Pai, *Energy Function Analysis for Power System Stability*. Norwell, MA: Kluwer, 1989.

[66] R. D. Zimmerman, C. E. Murillo Sánchez, and R. J. Thomas, "MATPOWER: Steady-State Operations, Planning, and Analysis Tools for Power Systems Research and Education," *IEEE Trans. Power Syst.*, vol. 26, no. 1, pp. 12–19, 2011.

[67] C. A. Baone, S. Veda, Y. Pan, W. Premerlani, J. Dai, A. Johnson, and S. Member, "Measurement based static load model identification," in *2015 IEEE Power & Energy Society General Meeting*, 2015, pp. 1–5.

[68] Y. Ge, A. J. Flueck, D. K. Kim, J. B. Ahn, J. D. Lee, and D. Y. Kwon, "An Event-Oriented Method for Online Load Modeling Based on Synchrophasor Data," *IEEE*

Trans. Smart Grid, vol. 6, no. 4, pp. 2060–2068, 2015.

[69] J. Hongjie, Y. Xiaodan, and Y. Yixin, "An improved voltage stability index and its application," *Int. J. Electr. Power Energy Syst.*, vol. 27, no. 8, pp. 567–574, Oct. 2005.

[70] H. Renmu, M. Jin, and D. J. Hill, "Composite load modeling via measurement approach," *IEEE Trans. Power Syst.*, vol. 21, no. 2, pp. 663–672, 2006.

[71] K. Wang, H. Huang, and C. Zang, "Research on Time-Sharing ZIP Load Modeling Based on Linear BP Network," in *5th International Conference on Intelligent Human-Machine Systems and Cybernetics*, 2013, pp. 37–41.

[72] V. V., S. Chakrabarti, and S. C. Srivastava, "Power system load modelling under large and small disturbances using phasor measurement units data," *IET Gener. Transm. Distrib.*, vol. 9, no. 12, pp. 1316–1323, 2015.

[73] P. Regulski, P. Wall, Z. Rusidovic, and V. Terzija, "Estimation of load model parameters from PMU measurements," in *IEEE PES Innovative Smart Grid Technologies Conference Europe*, 2015, pp. 1–6.

[74] L. Vanfretti and F. Milano, "Experience with PSAT (Power System Analysis Toolbox) as free and open-source software for power system education and research," *Int. J. Electr. Eng. Educ.*, vol. 47, no. September 2015, pp. 47–62, 2010.

[75] L. Vanfretti and F. Milano, "Application of the PSAT, an Open Source Software, for Educational and Research Purposes," in *2007 IEEE Power Engineering Society General Meeting*, 2007, pp. 1–7.

[76] J. Milanović, "On unreliability of exponential load models," *Electr. power Syst. Res.*, vol. 49, pp. 1–9, 1999.

APPENDIX

A.1 Sample 2-Bus System Parameters in PSAT Format

```
Bus.con = [ ...
  1  69  1.06  0  4  1;
  2  69  1.0029  -0.22667  4  1;
 ];

Line.con = [ ...
  1  2  100  69  60  0  0  0.05403  0.22304  0.0492  0  0  0  0  0  1;
  1  2  100  69  60  0  0  0.05403  0.22304  0.0492  0  0  0  0  0  1;
 ];

% Breaker.con = [ ...
%   16  2  100  69  60  1  1  200;
%  ];

SW.con = [ ...
  1  100  69  1.06  0  9.9  -9.9  1.2  0.8  2.324  1  1  1;
 ];

PQ.con = [ ...
  2  100  69  3  0.3  1.2  0.8  0  1;
 ];

Pl.con = [ ...
% no Sn  Vn   fn   g   Ip    Pn   b    IQ  Qn  z  u
   2 100 69  60   0 0     100    0  0   100   1  1;
];

Syn.con = [ ...
  1  615  69  60  5.2  0.2396  0  0.8979  0.2998  0.23  7.4  0.03  0.646  0.646
0.4  0  0.033  10.296  2  0  0  1  1  0  0  0  1  1;
 ];

Tg.con = [ ...
  1  1  1  0.02  1.2  0.3  0.1  0.45  0  12  50  1;
 ];

Exc.con = [ ...
  1  2  7.32  0  200  0.02  0.002  1  1  0.2  0.001  0.0006  0.9  1;
 ];

Pss.con=[...
%        Max     min output  Kw  Tw      T1  T2    T3      T4       Ka  Ta   Kp
Kv Vamax
%1  3  1  0.10000  -0.1000  -2  4.20000  0  3.15  1.0000  4.20000  25  0.5  20
5  0.045  0.045  0.045  -0.045  1  0.95  0  ;
```

```
1  2  1  0.1      -0.1      5  10    0.38 0.02   0.38    0.02     25  0.5  20
5  0.045  0.045  0.045  -0.045  1  0.95  0;
];
Bus.names = {...
  'Bus 01'; 'Bus 02'};
```

A.2 Publications During Ph.D. Study

Journal Papers

[1] **Haoyu Yuan**, Hantao Cui, and Fangxing Li, "A Measurement-based Voltage Stability Indicator for Voltage Dependent Load Models", *PES Letters*, to be submitted 2016.

[2] **Haoyu Yuan**, Fangxing Li, Tao Jiang, and Hongjie Jia, "Measurement-based Wide-Area Loading Margin Sensitivity and its Application in Voltage Stability Control," *IET Generation, Transmission and Distribution*, under review, 2016.

[3] **Haoyu Yuan**, Fangxing Li, Yanli Wei, and Jinxiang Zhu, "Novel Linearized Power Flow and Linearized OPF Models for Active Distribution Networks with Application in Distribution LMP," *IEEE Transactions on Smart Grid*, In-Press, 2016.

[4] **Haoyu Yuan** and Fangxing Li, "Hybrid Voltage Stability Assessment (VSA) for N-1 Contingency," *Electric Power Systems Research*, vol. 122, pp. 65-75, May. 2015.

[5] Tao Jiang, **Haoyu Yuan**, Hongjie Jia, Ning Zhou, Fangxing Li, "Stochastic subspace identification-based approach for tracking inter-area oscillatory modes in bulk power system utilising synchrophasor measurements," *IET Generation, Transmission and Distribution*, vol. 9, no. 15, pp. 2409–2418, 2015.

[6] Tao Jiang, Hongjie Jia, **Haoyu Yuan**, Ning Zhou, and Fangxing Li, "Projection Pursuit: A General Methodology of Wide-Area Coherency Detection in Bulk Power Grid," *IEEE Transactions on Power Systems*, vol. 31, no. 4, pp. 2776–2786, 2016.

[7] Tao Jiang, Linquan Bai, Hongjie Jia, **Haoyu Yuan**, and Fangxing Li, "Identification of Voltage Stability Critical Injection Region in Bulk Power Systems based on the Relative Gain of Voltage Coupling," *IET Generation, Transmission and Distribution*, vol. 10, no. 7, pp. 1495–1503, 2016.

Conference Papers

[8] **Haoyu Yuan,** Xue Li, Fangxing Li, Xin Fang, Hantao Cui, and Qinran Hu, "Mitigate Overestimation of Voltage Stability Margin by Coupled Single-Port Circuit Models," IEEE PES General Meeting 2016, 5 pages, Boston, MA, 2016. **(Best Conference Papers Award).**

[9] **Haoyu Yuan**, Tao Jiang, Hongjie Jia, Fangxing Li, Yateendra Mishra, Houhe Chen, and Guoqing Li, "Real-Time Wide-area Loading Margin Sensitivity (WALMS) in Power Systems," IEEE PES General Meeting 2015, 5 pages, Denver, Colorado, July 26-30, 2015.

[10] **Haoyu Yuan** and Fangxing Li, "A Comparative Study of Measurement-Based Thevenin Equivalents Identification Methods," 46th North American Power Symposium, 6 pages, Pullman, WA, Sept. 7-9, 2014.

[11] **Haoyu Yuan**, Fangxing Li, and Yanli Wei, "LMP Step Pattern Detection based on Real-Time Data," IEEE PES General Meeting 2013, 5 pages, Vancouver, BC, Canada, July 21-15, 2013.

VITA

Haoyu Yuan joined The University of Tennessee at Knoxville in August 2011 to pursue the Ph.D. degree in Electrical Engineering. He received his B.S. degree from Southeast University, Nanjing, China, in 2011, and concurrent M.S. degree from The University of Tennessee, Knoxville, TN, USA, in 2013. His research interests include power system stability and power system economics.